Measurement of Nuclear Transparency from $\mathbf{A}(e,e'\pi^+)$ Reactions

by

Benjamin Micheal Patrick Clasie

Submitted to the Department of Physics
in partial fulfillment of the requirements for the degree of

Doctor of Philosophy in Physics

at the

MASSACHUSETTS INSTITUTE OF TECHNOLOGY

August 2006

Author .....
Department of Physics
August 18, 2006

Certified by .....
Haiyan Gao
Associate Professor of Physics
Thesis Supervisor

Accepted by .....
Thomas J. Greytak
Chairman, Department Committee on Graduate Students

Measurement of Nuclear Transparency from A(e,$e'\pi^+$) Reactions

by

Benjamin Micheal Patrick Clasie

Submitted to the Department of Physics
on August 18, 2006, in partial fulfillment of the
requirements for the degree of
Doctor of Philosophy in Physics

Abstract

The color transparency phenomenon refers to the suppression of final-state interactions of a hadron propagating through the nuclear medium at large momentum transfer when the hadron is produced with small transverse size. The pion electroproduction cross section from ^{1}H, ^{2}H,^{12}C, ^{63}Cu and ^{197}Au targets from Q^2 = 1.1 to 4.8 (GeV/c)^2 was measured in Jefferson Laboratory Experiment E01-107. The nuclear transparency was formed by the ratio of (σ_A/σ_H) from the data and (σ_A/σ_H) from a model of electroproduction from nuclei that does not include π-N final state interactions. A signature of color transparency is the enhancement of the nuclear transparency at large Q^2 compared with predictions based on Glauber multiple scattering theory. This experiment represents the first nuclear transparency data from (e,$e'\pi^+$) reactions.

Thesis Supervisor: Haiyan Gao
Title: Associate Professor of Physics

Acknowledgments

My time at MIT was divided into two major projects, my work for the BLAST experiment (at the Bates Linear Accelerator Center), and the experiment described in this thesis (at JLab). I am very grateful for the support I received and the opportunities that were available during this time. I am indebted to seemingly countless people for what I have accomplished and, first of all, I would like to say thank you to all of these people.

My supervisor, Haiyan Gao, provided me with many opportunities and I am very grateful for her support and all she has taught me. When I first joined the MIT graduate program, Haiyan welcomed me to her research group with dinner at her home. She also provided many interesting projects to work on, including the laser-driven target project. I am impressed by her attention to detail and this was crucial in the success of the laser-driven target project. She encouraged me to attend several conferences during my time at MIT, including those in Russia, Japan and Hawaii. These experiences were an adventure and have been invaluable.

I had the pleasure of working closely with Dipangkar Dutta while he was at MIT and at Duke University. He was a spokesperson for the experiment in this thesis and he tirelessly answered many questions I had about the running and analysis of the experiment. He often made time for me in his busy schedule and I especially appreciate the rapid proof-reading of this thesis. He did this at a particularly busy time in his life, as it was during his move to Mississippi. He went above and beyond in giving me support and encouragement, particularly during the times before meetings and conferences.

The work of many former graduate students contributed to the analysis in this thesis. The JLab Hall-C experiments on pion electroproduction and the dissertations by Dave Gaskell (E91-003), Tanja Horn (E01-004) and Jochen Volmer (E93-021) addressed several key issues, such as modifications that included electroproduction in the Monte Carlo model, the transport and decay of pions in the simulation,the procedure for applying coincidence time cuts and the estimation of absorption of

pions in the HMS spectrometer.

In addition to Haiyan, I thank the other members of my committee, Bill Donnelly and Bob Redwine, for making room in their schedules for me and for their suggestions after reading my thesis. They also had many helpful comments since my first committee meeting and I appreciate the interest they have shown in my work. Thank you also to my academic adviser, Richard Yamamoto. Richard helped make to sure I was on track and I always looked forward to our conversations each semester.

My time at MIT would not have been the same without the work of many people from LNS. Many thanks to Joanne Gregory for organizing everything from my first office in the penthouse to travel packets; Sandy Tenorio and Sheela Hulsoor for the conversations and coffee, which helped me get through each day; Michael Grossman and George Sechen for their help with making and assembling parts for the laser-driven target project; and, Billy, Cheryl, Elsye, Jack, Jerry, Ken and Pier for making my time at MIT more enjoyable.

I shared many great experiences with fellow graduate students while taking classes at MIT and working on experiments at Bates and JLab. Jason Seely has been an unbelievable source of support, knowledge and friendship. We often worked together on the same or similar projects and, on many occasions, he went out of his way to provide assistance. Sometimes this involved the relatively simple answering of questions about his work, and other times he spent long hours setting up measurements with the laser-driven target. I learned a lot from Jason while we studied for the qualifying exams and while I worked on this thesis, as evidenced by the number of references to his work herein. Chris Crawford very patiently helped bring me up to speed with the laser-driven target project when I first arrived at MIT. Thank you Chris for showing me how to work with the various vacuum, electronic, mechanical and control systems related to this work. The glassblowing was fun too. Thank you also for all of your help with C++, ROOT and emacs. Tanja Horn helped me get acquainted with the Hall-C software and analysis when I first arrived at JLab and continued to help me through to the final results. Tanja was very thorough in her analysis and many of the methods she developed appear in this work, such as the tracking efficiency for

two-track events and the calculation of the pion absorption in the spectrometer windows. Thank you to Xin Qian who is analyzing the L-T separation results and has checked various parts of my work. Xin has been very good at coming up with fresh ideas in this complicated analysis. Thank you to Brad, Adam, Aaron, Sean, Yuan, Chi, Wang, Nik and Vitaliy and many other graduate students who have helped me through this experience.

My family, on both sides of the world, have been a continuous source of support. My wife, Debbie, has been very understanding in my pursuit of a PhD and I don't know where to start with how to express my gratitude. Thank you for being a part of the stressful times and the cheerful times, and for being understanding when I needed to work long hours on my thesis. My family in Australia have given me many opportunities that led to this point in my life. I thank my parents, Frank and Anne, my sister, Kyla and my brother, Shane, and his wife, Hannah, for their encouragement, and the constant supply of Vegemite^{TM}. My family in the US have been wonderful and have helped me enjoy my life outside of MIT. Thank you Dan, Vivian, Merith, Brook and Irving for your interest, support and generosity. A special thanks to Dan, Vivian and Merith for suffering through the 1 1/2 hour defense of my dissertation.

Contents

List of Figures

List of Tables

Chapter 1

Introduction and Physics Motivation

1.1 Color Transparency

The interactions between quarks and gluons are described by Quantum Chromodynamics (QCD), the theory of the strong force. QCD is well tested in the high energy regime where perturbative QCD calculations can be carried out. Interactions at low energies, such as the binding of protons and neutrons in a nucleus, appear to be better described using color-neutral nucleons and mesons as effective degrees of freedom, rather than quark and gluon degrees of freedom, due to our inability to solve QCD in the confinement region. The study of the transition from meson-nucleon degrees of freedom to quarks and gluons is an important topic in nuclear physics. This transition can be investigated through measurements of the onset of various predictions of QCD. One such prediction is the color transparency effect, which involves the expansion of a compact configuration of quarks into a normal-sized hadron.

The phenomenon of color transparency was first introduced by Mueller and Brodsky in 1982 [1, 2]. Experiments designed to search for color transparency have been performed since the late 1980s and currently there is no conclusive evidence for this effect. The goal of the experiment analyzed in this thesis, the Pion Color Transparency Experiment (πCT), was to search for the effects of color transparency in

semi-exclusive pion electroproduction reactions, A(e,e$'\pi^+$), and was the first experiment to search for color transparency in this channel. A positive slope of the nuclear transparency with increasing Q^2 is a signature for the color transparency effect that was searched for in πCT.

Color transparency refers to the suppression of final-state interactions of a hadron propagating through the nuclear medium in exclusive processes at large momentum transfer when the hadron is produced with small transverse size [3]. This behavior is predicted by QCD and is due to the selection of Fock states with the minimum number of constituents at transverse distances, $b_\perp \approx 1/\sqrt{Q^2}$, where (-$Q^2$) is the four momentum transfer squared. At large Q, the transverse size may be smaller than the equilibrium (free) size of the hadron, and the hadron may remain intact as it rapidly expands. Events where the hadron remains intact can be selected by experimental cuts in a coincidence experiment. The mechanism for the expansion of the hadron (for example, the hadronization time, which is the amount of time over which the small configuration expands) is poorly understood, as there is no widely accepted theory and the existing data are not sufficient to constrain or exclude models.

Three conditions must be satisfied to observe color transparency. These conditions are:

1. Large momentum transfer squared, so that hadrons are preferentially selected with small transverse size. This is based on the uncertainty principle, where the range of the virtual photon is approximately $1/Q$. The quarks that make up the hadron must come from a small region within this range and the small grouping of quarks is called a Point Like Configuration (PLC).

2. Large magnitude of the hadron velocity, so that the hadron can propagate out of the nucleus before returning to its equilibrium size. This can occur because the lifetime of the PLC is dilated in the rest frame of the nucleus. The distance over which the PLC travels before reaching its dressed (free) size is called the formation length. The formation length increases with increasing magnitude of the relative velocity between the hadron and the residual nucleus.

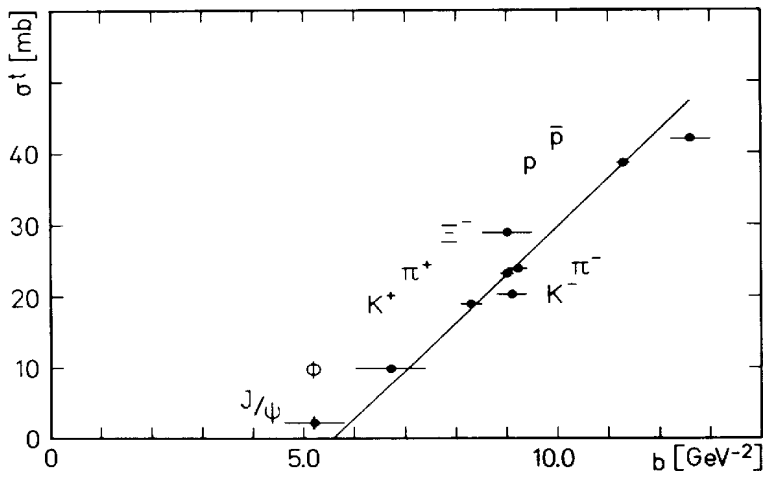

Figure 1-1: Experimental evidence for the geometric interpretation of the hadron-proton total cross section, σ^t. The slope parameter, b, is given by $b = R_h^2 + R_p^2$, where R_h is the radius of the hadron and R_p is the radius of the proton [4]. The figure is from Ref. [4].

3. Reduced interaction, or color screening, which is experienced between the hadron of reduced transverse size and the residual nucleus. Perturbative QCD predicts that the cross section for the interaction between a small $q\bar{q}$ dipole and the nucleus is proportional to b^2, where b is the transverse distance between the q and the $\bar{q}$. Experimental evidence for the dependence of the total cross section on the size of the hadron can be seen in Fig. 1-1 from Ref. [4].

Therefore, at a sufficiently large momentum transfer and formation length, one may find a nucleus to be completely transparent to the hadron produced in the reaction.

Nuclear transparency is defined as the ratio of the cross section per nucleon for a process on a bound nucleon in the nucleus to the cross section for the process on a free nucleon [5]. The nuclear transparency can be interpreted as the probability that the hadron produced in the reaction is not scattered outside of the experimental acceptance by the residual nucleus. If there is a color transparency effect, the nuclear transparency will depend on the momentum transfer involved in the process (it will have a positive slope with respect to the momentum transfer). This is because the valence quarks of the hadron are preferentially selected from smaller regions as Q^2 is increased. An increase in the nuclear transparency with increasing Q^2 will be in sharp

contrast to the theory of multiple scattering at high-energies in Ref. [6]. The nuclear transparency in this picture is energy independent due to the energy independence in the hadron-nucleon total cross section at high energies. The Q^2 dependence of the nuclear transparency was measured in πCT and, in addition, the dependence of the nuclear transparency on the nucleon number, A, was investigated.

1.2 Expansion models

The formation length, l_f, is the distance over which a PLC expands to its dressed (free) size. Assuming that this expansion occurs linearly with time, l_f is given by

$$l_f = \gamma t_0 \beta_{\rm lab}, \tag{1.1}$$

where $\beta_{\rm lab}$ is the speed of the hadron in the lab frame, $\gamma = 1/\sqrt{1-\beta_{\rm lab}^2}$, and t_0 is the time required for the expansion in the hadron rest frame. The naive parton model [7] assumes that quarks separate in the transverse direction at the speed of light and l_f is given by

$$l_f = \gamma R_h \beta_{\rm lab}. \tag{1.2}$$

The naive parton model of the expansion was improved by the quantum diffusion model, which was inspired by perturbative QCD. In this model, the quark separation, x_t, is proportional to $\sqrt{z}$, where z is the longitudinal distance from the production point to the position of the particle. The formation length in this model is determined from the average value of the dominant energy denominator [7]

$$l_f \simeq 2p_h \left\langle \frac{1}{M_n^2 - M_h^2} \right\rangle, \tag{1.3}$$

where p_h and M_h are the momentum and mass of the hadron, respectively, and M_n is the mass of a typical intermediate state of the hadron.

The setting with the largest pion momentum in πCT was at $p_\pi = 4.4$ GeV/c, which makes $l_f \sim 22$ fm in the naive parton model. A wide range of values have

been suggested for ΔM^2, which is the denominator in Equation 1.3, and current data do not constrain the value of l_f for pions. Based on semiclassical ideas, $\Delta M^2 = 0.25$ (GeV/c^2)^2 [7], and in Ref [8], it was estimated that $\Delta M^2 = 0.7$ (GeV/c^2)^2 based on the lowest lying Regge partner and $\Delta M^2 = 1.4$ (GeV/c^2)^2 was suggested as an upper limit. The formation length at the highest momentum setting will be 7 fm, 2.5 fm and 1.3 fm for $\Delta M^2 = 0.25$ (GeV/c^2)^2, 0.7 (GeV/c^2)^2 and 1.4 (GeV/c^2)^2, respectively. Therefore, some models predict that the formation length at the highest momentum setting in πCT may be larger than the radii of nuclei with small nucleon number.

1.3 Motivation

Color transparency (CT) is a novel QCD phenomenon and currently there is no conclusive evidence for this effect. In particular, there are no experimental data showing the onset of CT. The onset is particularly important for studying the expansion process and quantities such as the formation length. Data showing the onset of color transparency may help constrain models that may elucidate how a compact configuration of quarks expands into a hadron. Furthermore, the interaction between a scattered hadron and the residual nucleons is traditionally described by the Glauber multiple scattering mechanism [6] and CT will be an important modification to this theory if its existence is confirmed.

The onset of color transparency is important for the study of Generalized Parton Distributions (GPDs) and the measurement of GPDs is amongst the highest priorities in intermediate energy nuclear physics. GPDs provide information on the longitudinal momentum and, simultaneously, the transverse position of partons in a nucleon. The onset of CT is a requirement for factorization [9], which is related to access to GPDs. CT is not the only requirement for access to GPDs, for example, factorization assumes that leading-order perturbative QCD is fully applicable, and appreciable contributions from higher-twist amplitudes can lead to a breakdown of factorization.

The typical diagram showing factorization in deep-exclusive meson production

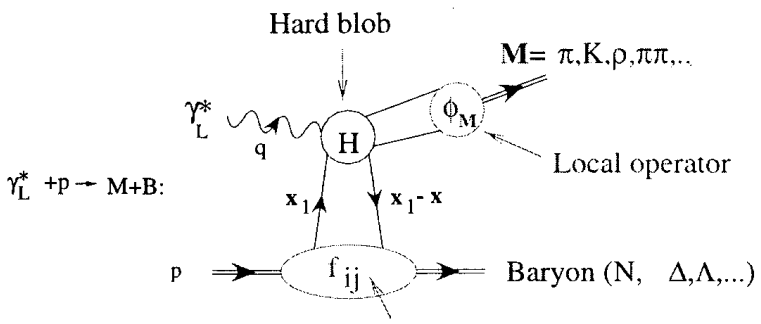

Figure 1-2: Factorization in deep-exclusive meson production (figure from Ref [9]).

is shown in Figure 1-2, where the amplitude for the process can be expressed as the convolution of three processes. The separation of these three processes is possible due to the incoherence of physical processes at widely separated energy scales (f_{ij} and ϕ_M are soft processes, whereas H is a hard process that can be calculated perturbatively). The process labeled with f_{ij} provides access to the GPD, H is the hard amplitude and ϕ_M is the meson distribution amplitude. CT is necessary in the separation of these processes as the exchange of gluons between the meson produced from the hard interaction and the baryon is suppressed.

1.4 Previous measurements

The first experiment designed to search for color transparency used the ^{12}C(p,2p) reaction and was performed at Brookhaven National Laboratory [10] in the late 1980s. Later, more measurements of the nuclear transparency, which used the same reaction, were performed at Brookhaven National Laboratory [11, 12]. The nuclear transparency was defined as the cross section for elastic p-p scattering in the nucleus divided by the cross section for elastic p-p scattering in hydrogen, with corrections for Fermi motion of the proton in the nucleus [10]. The observed nuclear transparency first increased as a function of the beam energy and then decreased, with a peak near 9 GeV. While this behavior was not predicted by traditional nuclear physics calculations, it is usually not attributed to color transparency. Ralston and Pire [13, 14]

proposed that this behavior may have been due to nuclear filtering. In this picture, the proton is viewed as having many components in its Fock-space wave function that are superposed to make a normal-sized proton. The nucleus can act like a filter that depletes the long-distance amplitudes of the incoming and scattered protons. Brodsky *et al.* [15] suggested that the peak in the nuclear transparency could be related to the threshold for charm resonance production.

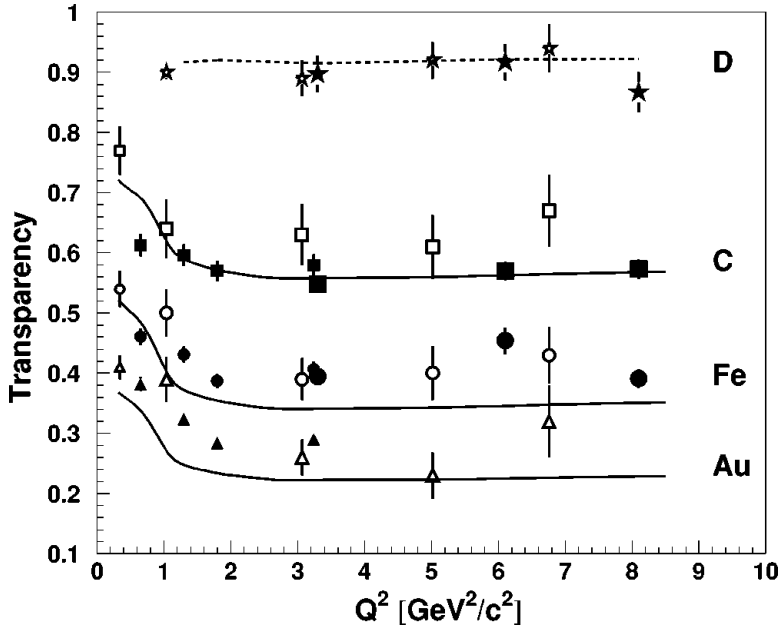

Figure 1-3: Transparency from $(e, e'p)$ quasielastic scattering. The figure comes from K. Garrow *et al.* [16]. The measurements made at Bates are the small open symbols, SLAC are the large open symbols, and JLab are the solid stars, squares and triangles. Errors for the JLab data points include statistical and point-to-point systematic uncertainties, but do not include model-dependent or normalization-type uncertainties. The SLAC and Bates data points include statistical and net systematic uncertainties.

Figure 1-3 shows the nuclear transparency measured using the A(e,e′p) reaction at the Bates Linear Accelerator Center [17], the Stanford Linear Accelerator Center (SLAC) [18] and the Thomas Jefferson National Accelerator Facility (JLab) [19, 20, 16]. The nuclear transparency in this reaction was defined as the ratio of the experimental yield to the yield from the Plane Wave Impulse Approximation (PWIA). The nuclear transparency was observed to be energy independent from $Q^2 \approx 2$ (GeV/c)^2

to the maximum measured Q^2 of 8.1 (GeV/c)^2 from deuterium, carbon, iron and gold targets. These measurements indicated that there was no significant effect from color transparency in the A(e,e′p) reaction up to $Q^2 = 8.1$ (GeV/c)^2. The absence of the color transparency effect in the A(e,e′p) reaction has been interpreted as an indication that the proton formation length may only have been as large as internucleonic distances, rather than the size of the nucleus, in these experiments [21].

Color transparency measurements using coherent and incoherent ρ^0 production have been performed at Fermilab [22] and more recently at DESY [23]. Electroproduction of ρ^0 mesons from a nucleus is described in Figure 1-4. The virtual photon fluctuates into a $q\bar{q}$ pair that has a transverse size $r_\perp \sim 1/Q$, which can propagate over a distance called the coherence length, l_c. The coherence length is given by

$$l_c = \frac{2\nu}{Q^2 + M_{q\bar{q}}^2}, \tag{1.4}$$

where ν is the energy of the virtual photon and $M_{q\bar{q}}$ is the invariant mass of the $q\bar{q}$ pair. The $q\bar{q}$ pair scatters from the target nucleus and evolves into a normal-size ρ^0 over a distance given by l_f. For coherent reactions, the target nucleus remains intact and in its ground state after the interaction. For incoherent reactions, the nucleus is excited or it breaks up.

The nuclear transparency for the production of ρ^0 mesons was defined as $T = \sigma_A/(A\sigma_H)$ and the results from Fermilab were parameterized with the function $T = A^{\alpha-1}$. A positive slope of α as a function of Q^2 was reported and appeared to contradict the flat Q^2 dependence predicted by the Glauber multiple scattering mechanism. However, the results have since been interpreted as a coherence length effect [24]. For kinematics with large l_c, the virtual $q\bar{q}$ pair may undergo interactions with the nucleus before the hard interaction that puts it on the mass shell. As the kinematics of this experiment were not at constant l_c, the variation of α with Q^2 was explained by a reduction in these initial-state interactions rather than by a reduction in final-state interactions.

More recent measurements of coherent and incoherent ρ^0 production at DESY [23]

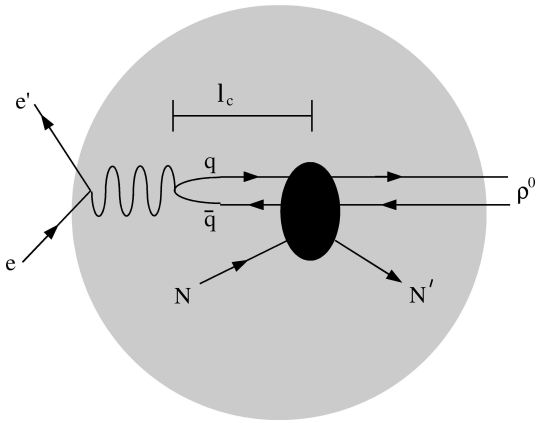

Figure 1-4: Electroproduction of ρ^0 mesons from a nucleus. The virtual photon fluctuates into a $q\bar{q}$ pair which can propagate over a distance, l_c, known as the coherence length. The $q\bar{q}$ pair evolves into a ρ^0 meson after interacting with the nucleus.

at $Q^2 = 0.9 - 3$ (GeV/c)^2 and at constant l_c showed a rise in the nuclear transparency with Q^2 consistent with theoretical calculations of color transparency. Although the results showed hints of color-transparency behavior, contributions from the complex interplay between various effects in the reaction mechanism may have influenced the observed effect [25]. Hence, these results did not provide conclusive evidence for color transparency.

The most convincing evidence for the existence of color transparency comes from an experiment performed at Fermilab [26]. The cross section of diffractive dissociation of 500 GeV/c pions into dijets was measured and parameterized with $\sigma = \sigma_0 A^\alpha$, where σ_0 is the π-N cross section in free space. The free parameter, α, was fit to the data with the result $\alpha \sim 1.6$. This result was in agreement with calculations assuming 100% color transparency and was very different to the normal π-N cross section, which has the dependence $\sigma = \sigma_0 A^{2/3}$. However, Q^2 could only be estimated from the transverse momentum of the individual jets with respect to the beam direction, k_t. It was estimated that $Q^2 \gtrsim 10$ (GeV/c)^2 in these results and the experiment did not provide information on the onset of color transparency with respect to Q^2.

The data from pion photoproduction from helium, ^{4}He$(\gamma, \pi^- p)$, at JLab (measurements at $\theta^\pi_{\rm cm} = 70^\circ$ are shown in Figure 1-5) displayed hints of color-transparency behavior [27, 28, 29]. Color transparency can be measured in photoproduction reac-

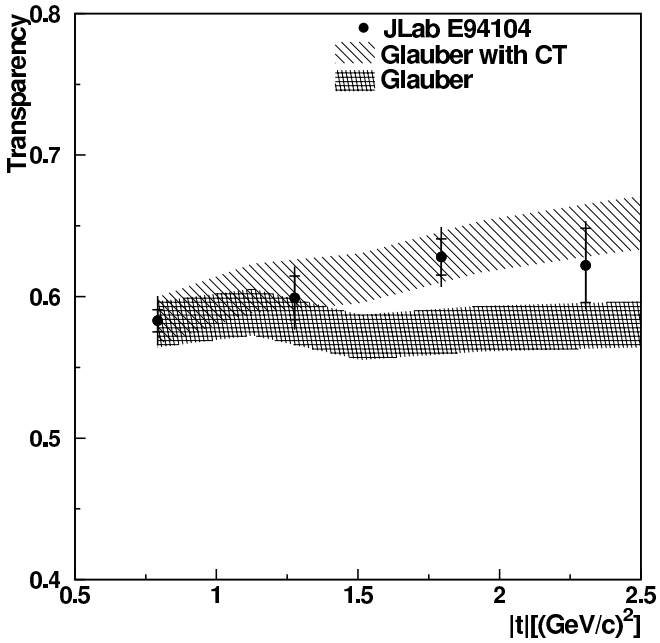

Figure 1-5: Transparency from ^{4}He$(\gamma, \pi^- p)$ at $\theta^{\pi}_{\rm cm} = 70^\circ$ as a function of the momentum transfer square to the hadron system, t (defined in Section 1.6). The figure comes from Ref. [27]. The inner error bars are statistical uncertainties, while the total error bars are statistical and point-to-point systematic uncertainties added in quadrature. There is, in addition, 4% normalization, or scale, systematic uncertainty.

tions, where $Q^2 = 0$, by measuring the cross section vs. the four momentum transfer squared, t, to the hadron system. The impact parameter of the real photon, b, is approximately $b \sim 1/\sqrt{-t}$, which can be likened to the range of a virtual meson with four momentum squared equal to t. At large $-t$, the impact parameter is small enough to force the partons to exchange the minimum number of gluons before they recombine into the final particles [30]. These hard gluons are exchanged between quarks within a limited range and these quarks form a PLC. The data from JLab showed 2σ deviations from traditional Glauber calculations and the slope of the data vs. $-t$ was in better agreement with calculations that included color transparency.

1.5 Advantage of using pions

Mesons are made up of only two valence quarks ($q\bar{q}$), while protons and other baryons are made up of three valence quarks (qqq). The production of a PLC requires the exchange of only one hard gluon for a $q\bar{q}$ system. Intuitively, it is more probable to produce a point-like configuration of a meson compared to a baryon, which requires the exchange of at least two hard gluons. The amplitude for producing a PLC with a transverse dimension of $1/Q$ is in general $(m/Q)^{k-1}$, where k is the number of constituents of the hadron and m^{-1} is the transverse dimension of the typical configuration of the hadron [7]. For a typical nuclear dimension of 1 fm and energy scale of $Q^2 = 5$ (GeV/c)^2, m/Q is approximately 0.1, and therefore, this amplitude decreases rapidly as the number of constituents and/or Q^2 increases.

Pions (π^+, π^0, π^-), which have the smallest mass of all the mesons, are easier to produce with velocities, $|\vec{v}|$, larger than protons with a given beam energy. The velocity of the hadron is important because the expansion of the PLC occurs over a finite time in the rest frame of the hadron. For larger velocities, the PLC will travel longer distances before expanding to its equilibrium size and will therefore have a longer formation length.

1.6 Kinematics

The particular reaction studied in πCT was A(e,e$'\pi^+$), which can be written as

$$e + A \rightarrow e' + \pi^+ + X, \tag{1.5}$$

where X represents other particles in the final state (for example a neutron and the residual A-1 nucleons). A diagram of the reaction is shown in Figure 1-6. All of the variables in this diagram are defined in the lab frame; the scattering plane is the plane containing the three-momentum of the incident and scattered electron; the reaction plane is the plane containing $\vec{q}$ and the pion momentum vector; θ_e is the electron scattering angle; θ_{pq} is the angle between the three-momentum of the virtual photon

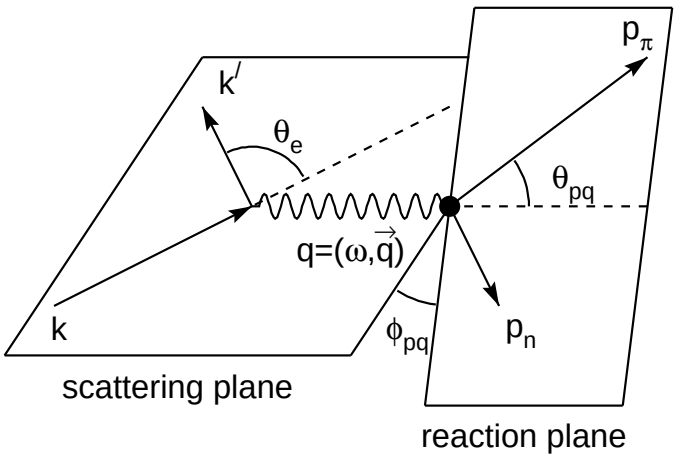

Figure 1-6: Pion electroproduction kinematics [31]. All quantities are in the lab frame.

and the pion; and ϕ_{pq} is the angle between the scattering plane and the reaction plane.

The pion electroproduction cross section is usually expressed as a function of Q^2, W and t, where $q^2 = -Q^2$ is the four-momentum transfer squared and W is the invariant mass of the virtual photon and the target, given by

$$W = \sqrt{M_A^2 + 2M_A\omega - Q^2}, \tag{1.6}$$

where ω (also called ν) is the energy of the virtual photon. The four-momentum squared of the momentum transferred to the nucleon(s), t, is given by

$$t = (q - p_\pi)^2 = (E_\pi - \omega)^2 - |\mathbf{p}_\pi|^2 - |\mathbf{q}|^2 + 2|\mathbf{p}_\pi||\mathbf{q}|\cos(\theta_{pq}). \tag{1.7}$$

The minimum value of $-t$, denoted by $-t_{\min}$, corresponds to the value of $-t$ when $\theta_{pq} = 0$. We can also define $-t_{\text{pole}} = -M_{\pi^+}^2$, which corresponds to the smallest value of $-t$ that can be obtained at any kinematics, and is not kinematically accessible in electroproduction. When $-t = -t_{\text{pole}}$, the denominator in Equation 1.40 is zero. The magnitude of the virtual pion 3-momentum, k_π, is given by

$$k_\pi = |\mathbf{q} - \mathbf{p}_\pi|. \tag{1.8}$$

The missing mass of the particles represented by X in Equation 1.5 is defined as M_x. The missing energy and missing momentum of X are given by

$$\begin{aligned} E_x &= E_e - E_{e'} + M - E_\pi, \text{ and,} \\ \boldsymbol{P}_x &= \boldsymbol{q} - \boldsymbol{p}_\pi. \end{aligned} \tag{1.9}$$

M_x can be constructed using the missing energy and momentum, and is $M_x = \sqrt{E_x^2 - \boldsymbol{P}_x^2}$. One can form the nuclear missing mass using $M = M_A$ in Equation 1.9. Another useful definition of the missing mass, called the nucleon missing mass, M'_x, can be formed using $M = M_p$ in Equation 1.9.

1.7 Pion electroproduction cross section

The elementary pion cross section is the cross section from a hydrogen target. The Born level, or first order, diagrams for this reaction are shown in Figure 1-7. The elementary pion cross section was measured in πCT using a hydrogen target and the model for the elementary process was iterated to match the data.

The pion electroproduction cross section from a stationary proton in the one-photon-exchange approximation is [32]

$$\frac{d^5\sigma}{d\Omega_{e'} dE_{e'} d\Omega_\pi} = \Gamma_\nu \frac{d^2\sigma}{d\Omega_\pi}, \tag{1.10}$$

where

$$\Gamma_\nu = \frac{\alpha}{2\pi^2} \frac{E_{e'}}{E_e} \frac{K_{eq}}{Q^2} \frac{1}{1-\epsilon} \tag{1.11}$$

is the virtual photon flux,

$$K_{eq} = (W^2 - M_p^2)/(2M_p) \tag{1.12}$$

is the equivalent photon energy,

$$\epsilon = \left(1 + \frac{2|\mathbf{q}|^2}{Q^2} \tan^2 \frac{\theta_e}{2}\right)^{-1} \tag{1.13}$$

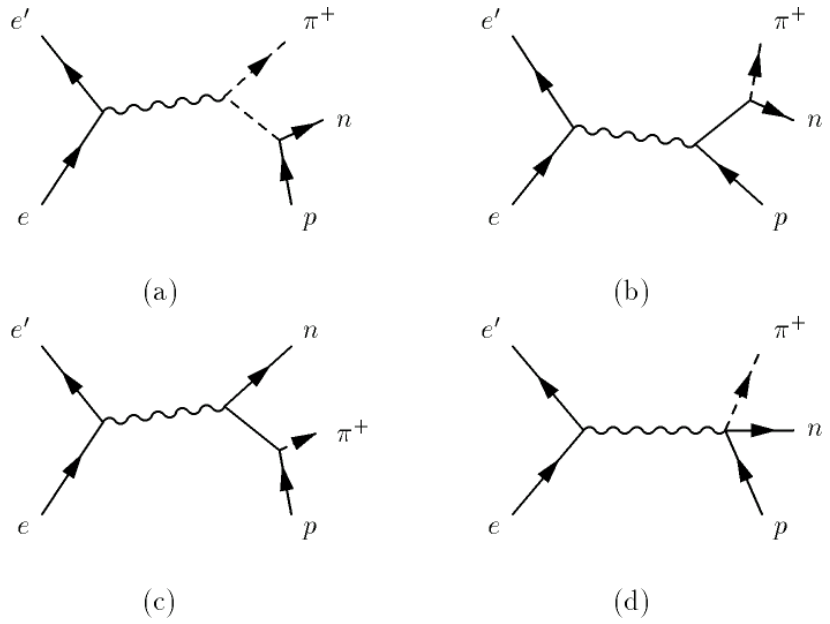

Figure 1-7: Born diagrams that contribute to the elementary pion cross section. (a) is the pion pole diagram (t-channel process), (b) is the nucleon pole diagram (s-channel), (c) is the crossed nucleon pole diagram (u-channel), and (d) is the seagull diagram.

is the longitudinal polarization of the virtual photon, and $\frac{d^2\sigma}{d\Omega_\pi}$ is the virtual photon cross section. The solid angle of the pion, Ω_π, is determined in the lab frame. The virtual photon cross section for a stationary proton target is

$$\frac{d^2\sigma}{d\Omega_\pi} = \epsilon\frac{d^2\sigma_L}{d\Omega_\pi} + \frac{d^2\sigma_T}{d\Omega_\pi} + \sqrt{2\epsilon(1+\epsilon)}\frac{d^2\sigma_{LT}}{d\Omega_\pi}\cos(\phi_\pi) + \epsilon\frac{d^2\sigma_{TT}}{d\Omega_\pi}\cos(2\phi_\pi), \qquad (1.14)$$

where the cross sections $\frac{d^2\sigma_L}{d\Omega_\pi}, \frac{d^2\sigma_T}{d\Omega_\pi}, \frac{d^2\sigma_{LT}}{d\Omega_\pi}$ and $\frac{d^2\sigma_{TT}}{d\Omega_\pi}$ depend on Q^2, W and t.

For nuclear targets, there is a new degree of freedom due to the relative momentum between the struck nucleon and the spectator nucleons, and the missing mass is no longer constrained by 4-momentum conservation to equal M_n, the mass of the neutron. The differential pion electroproduction cross section for a nuclear target is given by

$$\frac{d^6\sigma}{d\Omega_{e'}dE_{e'}d\Omega_\pi dM_x} = \Gamma_\nu\frac{d^3\sigma}{d\Omega_\pi dM_x}, \qquad (1.15)$$

where the virtual photon cross section is

$$\frac{d^3\sigma}{d\Omega_\pi dM_x} = \epsilon\frac{d^3\sigma_L}{d\Omega_\pi dM_x} + \frac{d^3\sigma_T}{d\Omega_\pi dM_x} + \sqrt{2\epsilon(1+\epsilon)}\frac{d^3\sigma_{LT}}{d\Omega_\pi dM_x}\cos(\phi_\pi) + \epsilon\frac{d^3\sigma_{TT}}{d\Omega_\pi dM_x}\cos(2\phi_\pi). \tag{1.16}$$

1.8 Quasifree pion electroproduction model

The quasifree model is used to describe electroproduction from nuclear targets. The energy of the incoming electron is large compared to the energy associated with the binding of nucleons in the nucleus and the nucleons bound in the target nucleus may be viewed as essentially free (the impulse approximation). Properties of the nucleons inside of the nucleus are assumed to be described by an independent particle shell model, where each nucleon interacts with a mean field exerted by the other nucleons. The probability of finding a nucleon with momentum $\mathbf{p}_m$, and separation energy E_m, in the nucleus is given by the spectral function, $S(E_m, \mathbf{p}_m)$.

In πCT, the π^+ particle was detected in coincidence with the scattered electron, and therefore, the struck nucleon was constrained to be a proton by charge conservation. The struck proton was changed into a neutron by the interaction and a schematic of this process is shown in Figure 1-8. The model for electroproduction from nuclear targets was built from the measured cross section from a hydrogen target. Pions were assumed to be produced from individual protons that made up the nucleus, which had an initial momentum due to Fermi motion.

The quasifree pion electroproduction cross section for a nuclear target is given by

$$\frac{d^6\sigma_{\rm A}}{d\Omega_{e'}dE_{e'}d\Omega_\pi dP_\pi} = \int dE_m d\boldsymbol{p}_m S(E_m, \boldsymbol{p}_m)\frac{d^5\sigma_{\rm H}}{d\Omega_{e'}dE_{e'}d\Omega_\pi}\delta\left(h(E_m, \boldsymbol{p}_m) - P_\pi\right), \tag{1.17}$$

where,

$$\frac{d^5\sigma_{\rm H}}{d\Omega_{e'}dE_{e'}d\Omega_\pi} = f_\Gamma\Gamma_\nu\frac{d^2\sigma_{\rm H}}{d\Omega_\pi} \tag{1.18}$$

is the elementary cross section for a proton that is moving due to Fermi motion, $\delta(h(E_m, \boldsymbol{p}_m) - P_\pi)$ is a delta function that restricts P_π to those values allowed by 4-momentum conservation, and, $P_\pi = |\mathbf{p}_\pi|$. The factor, f_Γ, corrects the virtual photon flux due to the proton

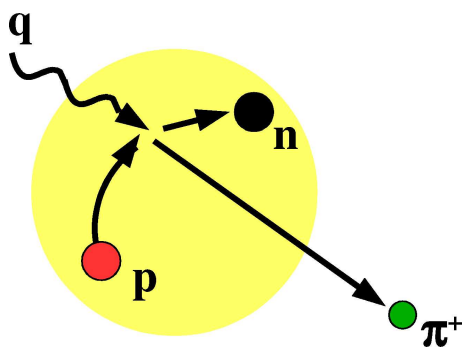

Figure 1-8: Schematic of quasifree pion electroproduction. The lightly shaded area (yellow in color) represents a nucleus. A proton, p, was moving inside of the nucleus when it was struck with a virtual photon, q. A neutron, n, and a π^+ particle are produced in the reaction.

Fermi motion and f_Γ is given by

$$f_\Gamma = \frac{M_p/E_p}{1 - \boldsymbol{p}_m \cdot \hat{z}/E_p}, \tag{1.19}$$

where $\hat{z}$ is the direction of the incident beam and E_p is the energy of the proton. The delta function and E_p will be discussed further in the next section. P_π was not generated randomly in the Monte Carlo simulation (Chapter 4) due to the constraint imposed by the delta function.

Models of the virtual photon cross section, $\frac{d^2\sigma_{\rm H}}{d\Omega_\pi}$, usually give $\frac{d^2\sigma_{\rm H}}{dtd\phi_{\rm cm}}$, where $\phi_{\rm cm}$ is the angle between $\mathbf{q}$ and $\mathbf{p}_\pi$ in the γ^*-p center of mass frame. The variables can be transformed using the Jacobian

$$\frac{d^2\sigma_{\rm H}}{d\Omega_\pi} = \frac{\partial(t, \phi_{\rm cm})}{\partial(\cos\theta, \phi)} \frac{d^2\sigma_{\rm H}}{dtd\phi_{\rm cm}}. \tag{1.20}$$

The virtual photon cross section in these new variables was iterated until it matched the hydrogen data and was different for each kinematic setting. However, the starting point for iterations was the parameterization

$$\begin{aligned}
\tfrac{d^2\sigma_L}{dtd\phi_{\rm cm}} &= f_W 350 Q^2 \tfrac{\exp(-t(16-7.5\ln Q^2))}{(1+1.77Q^2+0.05Q^4)^2}, \\
\tfrac{d^2\sigma_T}{dtd\phi_{\rm cm}} &= f_W (4.5/Q^2 + 2/Q^4), \\
\tfrac{d^2\sigma_{LT}}{dtd\phi_{\rm cm}} &= f_W \left(\exp(0.79 - \tfrac{3.4}{\sqrt{Q^2}} t) + 1.1 - \tfrac{3.6}{Q^4} \right) \sin(\theta_{\rm cm}), \text{ and,} \\
\tfrac{d^2\sigma_{TT}}{dtd\phi_{\rm cm}} &= -f_W \tfrac{5}{Q^4} \tfrac{|t|}{(|t|+0.02)^2} (\sin\theta_{\rm cm})^2,
\end{aligned} \tag{1.21}$$

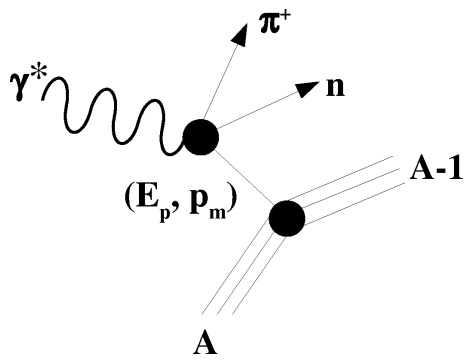

Figure 1-9: Diagram showing quasifree A(e,e′π^+). The proton that is hit by the virtual photon has 4-momentum p_p=(E_p,$\mathbf{p_m}$).

where, $f_W = \frac{8.539}{2\pi(s-M_p^2)^2}$. This form of the virtual photon cross section was based on the parameterization in J. Volmer's work [33] that was later extended to higher Q^2.

1.9 Models for the energy of the proton

In the quasifree approximation, the virtual photon interacts with a single proton inside a nucleus (Figure 1-9). The momentum of the proton is given by $\mathbf{p_m}$, however, E_m is not the energy of the proton and it can be interpreted as the separation energy. Therefore, the energy of the proton, E_p, is not constrained by any of the assumptions in the quasifree approximation.

A model that can be used to determine E_p is described in Ref. [31], and is called the default model in this thesis. This model assumes that the invariant mass of the spectator nucleons are the same immediately before and after the interaction, which is based on the hypothesis that the spectator nucleons were unaffected by the interaction. The mass of the spectator nucleons, M^*_{A-1}, can be determined from the usual definition of E_m,

$$E_m \equiv M_p + M^*_{A-1} - M_A, \tag{1.22}$$

and the energy of the struck proton is given by

$$E_p = M_A - \sqrt{(M^*_{A-1})^2 + |\mathbf{p}_m|^2}. \tag{1.23}$$

The function, $h(E_m, \boldsymbol{p}_m)$, in the delta function in Equation 1.17 conserves 4-momentum in

the elementary process and can be determined by solving the relation

$$M_n^2 = (q + p_p - p_\pi)^2, \tag{1.24}$$

where $p_p = (E_p, \mathbf{p}_m)$ and q are the 4-momenta of the proton and virtual photon respectively, and $p_\pi = (\sqrt{h^2 + M_\pi^2}, h\hat{\mathbf{p}}_\pi)$.

A second model was developed in the πCT analysis that we called the "$E_m = 0$" model. The development of this model was based on the realization that we do not know anything about the recoiling neutron in Figure 1-9 as only the outgoing electron and pion were detected. This is a distinction between A(e,e$'\pi^+$) and A(e,e$'$p), because in the latter reaction the nucleon is detected outside of the nucleus. In A(e,e$'\pi^+$), it is possible for the neutron not to leave the nucleus and it can be off the mass shell in the final state. It was therefore assumed that the A(e,e$'\pi^+$) process could have taken place without the shift in energy due to the separation energy of the proton. This model is similar to the default model, except that E_m was set to zero in Equation 1.22, giving

$$M_{A-1}^* = M_A - M_p. \tag{1.25}$$

The procedure for determining $h(E_m, \boldsymbol{p}_m)$ then followed the same steps as in the previous method. E_p was determined using Equation 1.23, except with the new definition of M_{A-1}^*, and $h(E_m, \boldsymbol{p}_m)$ followed from Equation 1.24. With this model, E_m did not affect E_p, and $h(E_m, \boldsymbol{p}_m) = h(\boldsymbol{p}_m)$. Therefore, the quasifree cross section (Equation 1.17) was simplified,

$$\frac{d^6\sigma_{\rm A}}{d\Omega_{e'} dE_{e'} d\Omega_\pi dP_\pi} = \int d\boldsymbol{p}_m \frac{d^5\sigma_{\rm H}}{d\Omega_{e'} dE_{e'} d\Omega_\pi} \delta\left(h(\boldsymbol{p}_m) - P_\pi\right) \int dE_m S(E_m, \boldsymbol{p}_m) \tag{1.26}$$

$$= \int d\boldsymbol{p}_m S(\boldsymbol{p}_m) \frac{d^5\sigma_{\rm H}}{d\Omega_{e'} dE_{e'} d\Omega_\pi} \delta\left(h(\boldsymbol{p}_m) - P_\pi\right), \tag{1.27}$$

where $S(\boldsymbol{p}_m) = \int dE_m S(E_m, \boldsymbol{p}_m)$.

A third model was also tested that we called the "Proton-on-shell" model. This model assumed that the proton was on the mass shell before the interaction. The procedure for calculating the quasifree cross section was the same as the "$E_m = 0$" model, except that E_p was given by

$$E_p = \sqrt{|\boldsymbol{p}_m|^2 + M_p^2}. \tag{1.28}$$

The function $h(E_m, \boldsymbol{p}_m)$ was also simplified to $h(\boldsymbol{p}_m)$ in this model.

1.10 Spectral functions

The spectral functions used in this analysis were independent-particle shell model spectral functions that did not include correlations. The copper spectral function was constructed for πCT, whereas existing spectral functions were used for deuterium, carbon, aluminum and gold. The deuterium, carbon and gold spectral functions were obtained from SLAC experiment NE18 [18, 19] and the aluminum spectral function was obtained from Ref. [34].

The deuterium spectral function was calculated using the Bonn potential [35] as input to the optical model. However, the high-momentum tails of the spectral function did not extend far enough and the spectral function from the Bonn potential was merged with a spectral function calculated using the Argonne v_{18} potential [36]. The carbon and gold spectral functions were computed by the program DWEEPY [37, 38], which solves the Schrödinger equation in an optical model potential. The parameters for the optical model potentials were obtained from the data of Ref. [39] and more details on these spectral functions can be found in Ref. [40].

The copper spectral function was constructed from the iron spectral function described in Ref. [40] by increasing the number of protons in the outermost 1f shell from 6 to 9 and changing the central binding energy, E_B, of this shell using the separation energy, E_{sep}, for copper. The central binding energy of a shell is a variable that comes from the DWEEPY model and is

$$E_B = K_N + E_{\text{sep}}, \tag{1.29}$$

where, $K_N = \sqrt{|\mathbf{p}_m|^2 + M_N^2} - M_N$ is the kinetic energy of a nucleon inside of a nucleus. The binding energy distribution of the 1f shell was calculated using the Lorentzian

$$\mathcal{L} = \frac{1}{\pi} \frac{\Gamma/2}{(E - E_B)^2 + (\Gamma/2)^2}, \tag{1.30}$$

where the width parameter, Γ, was taken from the formula of Brown and Rho [41]

$$\Gamma(E) = \frac{(24 \text{ MeV})(E - E_F)^2}{(500 \text{ MeV}^2) + (E - E_F)^2}. \tag{1.31}$$

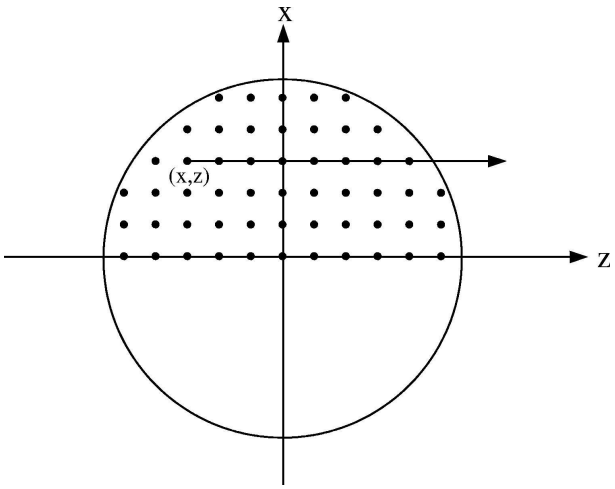

Figure 1-10: Schematic of a Glauber scattering calculation for A(e,e′π^+). The circle represents a nucleus, and the point at (x,z) represents the point where the pion was created. The pion is propagated parallel to the z axis where it can interact with the nucleons in the residual nucleus.

The width parameter for copper was much smaller than 1 MeV, which is smaller than the resolution of the spectrometers in πCT. Therefore, Γ was set to 1 MeV, as was the case with iron.

1.11 Glauber scattering theory

The nuclear transparency in A(e,e′π^+) can be calculated using Glauber scattering theory [6] and is called the Glauber transparency. A simple Glauber transparency simulation is described below. The point where the pion was created was generated randomly inside the nucleus. The pion was given a random momentum direction and propagated until it was outside of the nucleus. The nucleus was assumed to be spherical and, therefore, the interaction point was only generated in a half-circle in the 2-dimensional x-z plane (Figure 1-10). The pion was propagated parallel to $\hat{z}$ with the step size Δz. The transmission of the pion, T_π, after completing each step was given by

$$T_\pi = 1 - (n_p \sigma_{\pi p} + n_n \sigma_{\pi n}) \Delta z, \tag{1.32}$$

where n_p (n_n) was the number density of protons (neutrons) and $\sigma_{\pi p}$ ($\sigma_{\pi p}$) was the π^+-p (π^+-n) cross section. The π^+-p and π^+-n cross sections were taken from Ref. [42], which

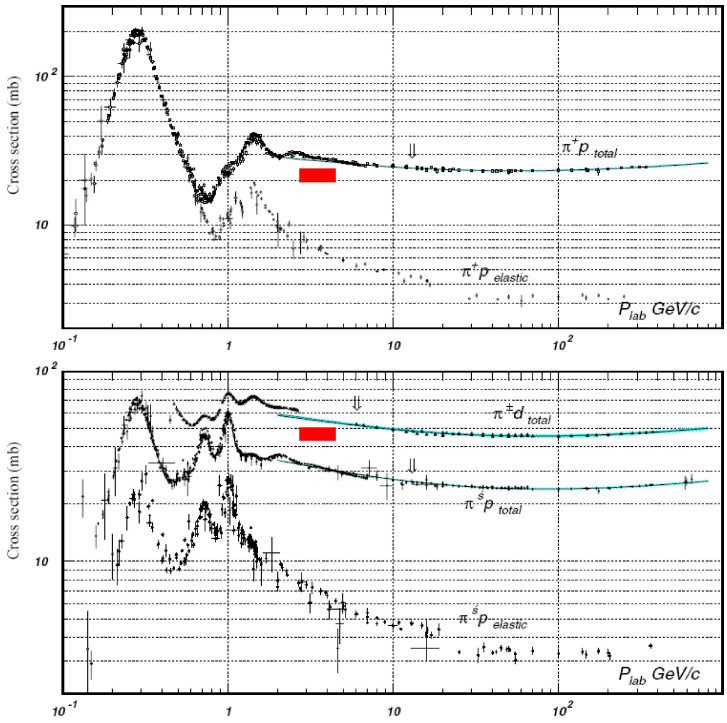

Figure 1-11: The π^+-p and π^+-d cross sections from the Particle Data Group [42]. The solid (red) bar indicates the pion momentum range in πCT.

are shown in Figure 1-11. These cross sections were dominated by inelastic scattering and the neutron cross section was determined by subtracting $\sigma_{\pi p}$ from $\sigma_{\pi d}$. The variation in these cross sections was at most $\pm 5.4\%$ from the value of the cross section at the center of the solid (red) bar in Figure 1-11.

The model was extended to include the pair distribution function, $g_{pN}(\mathbf{r}_1, \mathbf{r}_2)$ (see for example Ref. [43]). The pair distribution function describes the joint probability of finding a proton at the position $\mathbf{r}_1$ and a different nucleon at $\mathbf{r}_2$. The pair distribution functions were normalized such that

$$\begin{aligned}
&\int n_p(\mathbf{r}_2) d\mathbf{r}_2 - \int n_p(\mathbf{r}_2) g_{pp}(0, \mathbf{r}_2) d\mathbf{r}_2 = 1, \\
&\int n_n(\mathbf{r}_2) d\mathbf{r}_2 - \int n_n(\mathbf{r}_2) g_{pn}(0, \mathbf{r}_2) d\mathbf{r}_2 = 0, \\
&\int n_p(\mathbf{r}_1) n_p(\mathbf{r}_2) g_{pp}(\mathbf{r}_1, \mathbf{r}_2) d\mathbf{r}_1 d\mathbf{r}_2 = Z(Z-1), \text{ and,} \\
&\int n_p(\mathbf{r}_1) n_n(\mathbf{r}_2) g_{pn}(\mathbf{r}_1, \mathbf{r}_2) d\mathbf{r}_1 d\mathbf{r}_2 = (A-Z)(Z-1).
\end{aligned} \tag{1.33}$$

The transmission of the pion after completing each step was modified to include the pair

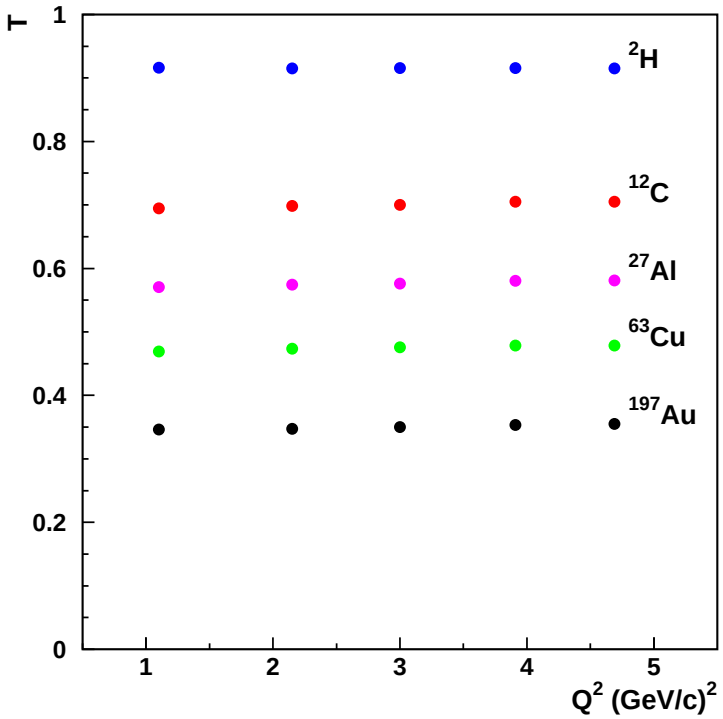

Figure 1-12: The Glauber transparency using a Monte Carlo simulation developed for πCT.

distribution functions

$$T_\pi = 1 - (g_{pp} n_p \sigma_{\pi p} + g_{pn} n_n \sigma_{\pi n}) \Delta z. \tag{1.34}$$

The Glauber transparency, which is equal to the transmission of the pion after exiting the nucleus, was determined at the kinematics encountered in πCT (Table 2.4). The results of this Glauber simulation are shown in Figure 1-12, and the Glauber transparency at the highest Q^2 were at most 2% larger than the lowest Q^2 for all of the nuclei shown.

1.12 Models of color transparency

Refs. [7, 8] give the cross section for the pion during and after the expansion process,

$$\sigma_{\pi N}^{eff}(z, p_\pi) = \sigma_{\pi N}(p_\pi) \left(\left\{ \left(\frac{z}{l_f} \right)^\tau + \frac{n^2 \langle k_t^2 \rangle}{Q^2} \left[1 - \left(\frac{z}{l_f} \right)^\tau \right] \right\} \theta(l_f - z) + \theta(z - l_f) \right), \tag{1.35}$$

where, l_f is the formation length (the distance over which the expansion takes place). The cross section of the initially produced PLC at $z = 0$ is

$$\sigma_{PLC} = \sigma_{\pi N}(p_\pi)\frac{n^2\left\langle k_t^2\right\rangle}{Q^2}, \tag{1.36}$$

where $n = 2$ is the number of quarks in a pion and $\left\langle k_t^2\right\rangle^{\frac{1}{2}} \approx 0.35$ GeV/c is the average transverse momentum of a parton in a hadron [7]. A model without CT can be obtained by setting $\tau = 0$ in Equation 1.35, $\tau = 1$ corresponds to the quantum diffusion model and $\tau = 2$ corresponds to the naive parton model.

Recently, the quantum diffusion model was used in a semi-classical approximation to estimate the effects of color transparency in the energy range of πCT [8]. The transparency was determined using a semi-classical formula involving an integral over the path of the outgoing pion,

$$T = \frac{1}{A}\int d^3r n(r)\exp\left[-\int_z^\infty dz'\sigma_{\pi N}^{eff}(z'-z,p_\pi)n(r')\right]. \tag{1.37}$$

The formation length was determined using the quantum diffusion model,

$$l_f \simeq 2p_\pi/\Delta M^2, \tag{1.38}$$

with $\Delta M^2 = 0.7$ (GeV/c^2)^2. The predicted change in the nuclear transparency was approximately 17%, 32% and 33% for ^{12}C, ^{63}Cu and ^{197}Au, respectively, for the range of energies in πCT.

B. Z. Kopeliovich *et al.* in Ref. [44] provided a more quantum mechanical model for predicting the effects of CT in exclusive ρ^0 production on nuclei. The cross section of a $q\bar{q}$ pair with transverse size, r, had the cross section

$$\sigma(r) = \frac{1}{3}\pi^2 r^2 \mathcal{F}(\nu, r), \tag{1.39}$$

where $\mathcal{F}(\nu, r)$ is related at small r to the gluon structure function of the proton by $\mathcal{F}(\nu, r) = \alpha_s(r)xg(x, Q_r^2)$, which is evaluated at the virtuality $Q_r^2 \sim a/r^2$ (where $a \sim 7-10$), $x \approx (Q_R^2 + m_\nu^2)/2M_N\nu$, and, $\alpha_s(r)$ is the running QCD coupling. However, this model has not been used to predict the effects of color transparency in the A(e,e$'\pi^+$) reaction.

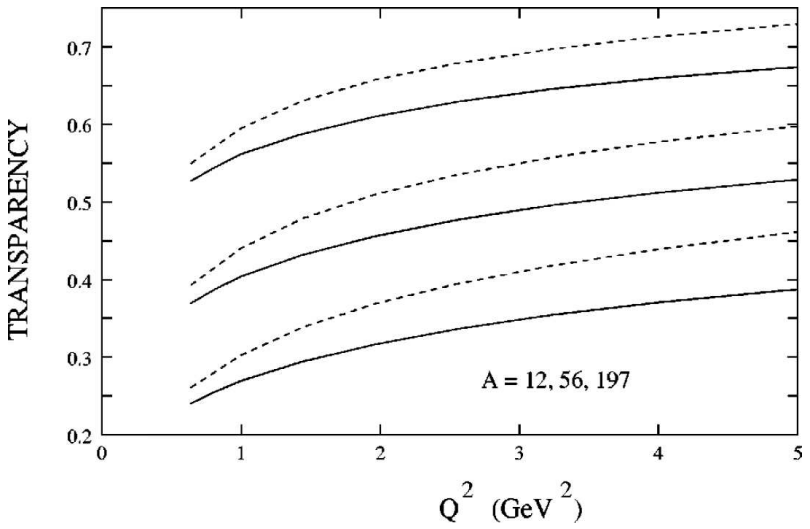

Figure 1-13: Calculation of the nuclear transparency in A(e,e$'\pi^+$) by B. Kundu *et al.* (Figure from Ref. [45]). The solid and dashed curves use end-point and asymptotic distribution amplitudes respectively and correspond to A=12, 56 and 197 from top to bottom.

The nuclear transparency for different nuclei for A(e,e$'\pi^+$) was calculated for the kinematics in πCT by B. Kundu *et al.* in Ref. [45]. This model followed a perturbative QCD approach, where the struck hadron was full sized and, subsequently, only the short distance amplitudes dominated inside the integrations. This model relied on the pion distribution amplitude, $\phi(x, 1/b)$ (this is a function of the Feynman variable x and the transverse separation between the quarks, b), to describe the zero-distance wave functions. The distribution amplitude models can be classified as "end-point" dominated (from QCD sum rules) or "centrally" dominated (from the asymptotic distribution amplitudes). They used both an end-point model [46, 47] and an asymptotic model [48] and the predicted nuclear transparency for each case is shown in Figure 1-13.

1.13 Background processes and other considerations

In this experiment, the signal searched for was a deviation between the experimental data and the quasifree production model for deuterium and heavier targets. Background processes, which were those that were not described by the quasi-free model, may have obscured

this signal. The kinematics of the experiment were chosen to minimize the influence of background processes, however, a model uncertainty was assigned to the nuclear transparency results due to these effects (Chapter 5).

1.13.1 Pauli blocking

Pauli blocking is an effect due to antisymmetrization of identical Fermion wave functions. As a result, no two identical fermions, such as protons and neutrons, can have the same quantum numbers. Ideally, a model of Pauli blocking of the recoiling neutron in A(e,e$'\pi^+$) should be constructed using the wave function of the nucleus and an operator for elementary pion electroproduction to calculate the amplitude for this process. However, existing operators for the elementary pion electroproduction process were not valid at the energies encountered in πCT (see for example MAID2003 in Ref. [49]). The model for Pauli blocking that was used in πCT is described in Section 4.4.

1.13.2 Pion absorption in nuclear matter

The free cross section for pion-nucleon scattering, $\sigma_{\pi N}$, was assumed not to be modified when a nucleon was inside of a nucleus, or at least not to be energy independent. This assumption was based on the observation that $\sigma_{\pi N}$ is energy independent for the pion momenta encountered in πCT (Figure 1-11) and therefore any modification should also have been energy independent to first order. Ref. [8] made the former assumption for our pion momenta and Ref. [50] assumed that $\sigma_{\pi N}$ was independent of the nucleon number. Measurements of the pion-nucleus absorption cross section are presented in Ref. [51] as a function of the pion momentum. Although there were few measurements for pions with momentum between 2 and 4 GeV/c, the data suggested that the pion-nucleus cross section did not have a strong dependence on the pion momentum.

1.13.3 n-N final-state interactions

It was not expected that n-N Final-State Interactions (n-N FSI) would influence the events in A(e,e$'\pi^+$) that had small missing mass, $M_x \approx M_{A-1} + M_n$. This was the threshold for single-pion production and at this threshold the recoiling neutron and spectator nucleons had zero relative momentum. The Jost function formalism (Section 5.4.1 in Ref. [31]) can

be used to include n-N final state interactions in the quasi-free model for $A \leq 3$. Corrections for n-N FSI in the πCT analysis are described in Section 4.3.

1.13.4 Multiple-pion production

The quasi-free production model did not describe the production of more than one pion in a single event, which is called multiple-pion production. Multiple-pion production from hydrogen targets in πCT was suppressed due to the relatively high $Q^2 > 1$ (GeV/c)^2 and $W > 2.1$ GeV, which was outside of the resonance region. In fact, no significant multiple-pion production in the missing mass distributions from hydrogen targets was seen in πCT (Appendix A). These results suggested that the mechanism for multiple-pion production involved the outgoing pion producing one or more pions from a nucleon in a second process that was incoherent (the amplitude for the second process does not undergo interference with the first process) from the production of the first pion. A model of multiple-pion production based on this assumption is described in Section 4.8. Multiple-pion events can only be produced above a missing mass threshold that is larger than the missing mass threshold for single-pion production. Therefore, a missing mass cut was employed in πCT to suppress multiple-pion events in the data samples (Section 3.2). The multiple-pion production simulation was used to estimate the contamination from multiple-pion events and was at most 0.4% when missing mass cuts were employed.

1.13.5 Rescattering

Rescattering events may contribute to the results when $-t > -t_{\rm pole}$. Rescattering in A(e,e$'\pi^+$) involves the electroproduction of a meson followed by a second interaction that produces the π^+ particle. For example, rescattering can occur through ρ electroproduction followed by $\rho N \rightarrow \pi N'$. A diagram for rescattering is shown in Figure 1-14.

The cross section for rescattering can become very large compared to the single scattering cross section. Although little is known about the rescattering contribution for the kinematics encountered in πCT, the effect in ρ^0 photoproduction is shown in Figure 1-15. Rescattering contributions dominate the cross section in ρ^0 photoproduction for $-t > 0.5$ (GeV/c)^2. As $t_{\rm min}$ varied between settings in πCT, some settings could be more susceptible to rescattering contributions. The πCT central kinematics were chosen so

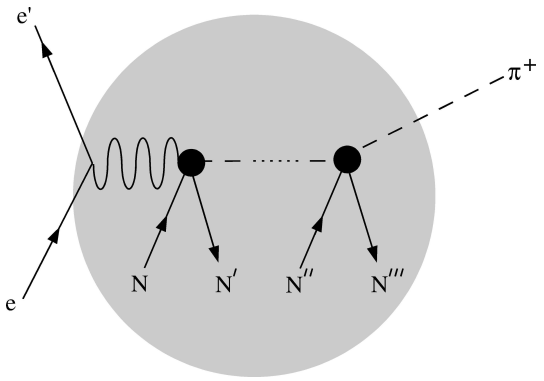

Figure 1-14: The diagram corresponding to rescattering in pion electroproduction inside a nucleus (shaded region). The interactions represented by the black circles may or may not be coherent with each other, and so the meson line joining these circles contains a fine-dashed line.

that $-t_{\rm central} \gtrsim -t_{\rm pole}$, however, the region near the pion pole was avoided for the reasons described in Section 1.13.6. Furthermore, the πCT central kinematics were chosen with $-t = -t_{\rm min}$, or as close to this condition as possible given the allowed rotation angles of the spectrometers. Under these conditions, $\theta_{pq} \approx 0$, and the contribution due to rescattering events were reduced by the missing mass cut used to exclude multiple-pion events. We verified experimentally that there were no observable contributions from rescattering at $-t = 0.374$ (GeV/c)^2 using the W vs. k_π test point (Table 2.4).

1.13.6 Pion pole

The elementary pion electroproduction cross section changes rapidly in the vicinity of the pion pole ($-t_{\rm pole} = -M^2_{\pi^+}$). In this region, the longitudinal cross section is dominated by the t-channel process (Fig. 1-7), and is given by

$$\sigma_L \approx \frac{-t\ Q^2}{(t - M^2_{\pi^+})^2} g^2_{\pi NN}(t) F^2_\pi(Q^2, t), \tag{1.40}$$

where $g_{\pi NN}$ is the πNN coupling and F_π is the pion form factor.

A smoothly varying cross section was desirable in πCT as the model for the elementary process was iterated to match the experimental data from the hydrogen target. This cross section may not be valid in the quasi-free model of a nucleus if the cross section is rapidly varying as some nucleons have large-momentum due to the tails of the spectral function,

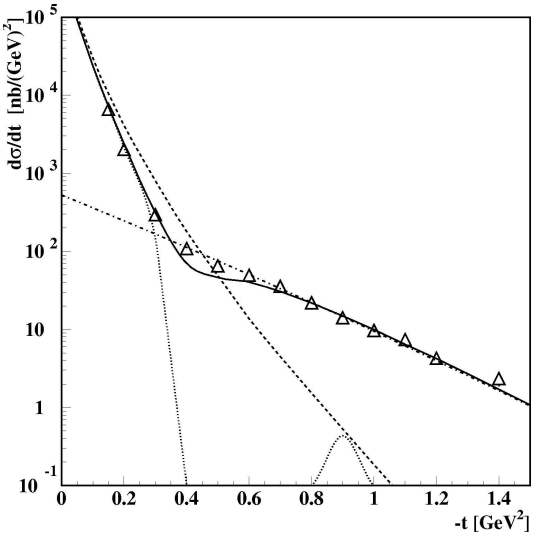

Figure 1-15: The t dependence of the rescattering cross section in ρ^0 photoproduction. The dashed, dash-dotted, dotted and solid curves represent single scattering, double scattering, interference between single and double scattering, and full contributions respectively. The triangles are experimental data from Ref. [52] and the figure is from Ref [53].

and, these nucleons may be outside of the range of the model for the elementary process. Furthermore, F_π is not known very accurately above $Q^2 = 1 - 2$ (GeV/c)^2, which could complicate corrections for this effect. The kinematics of πCT were chosen to minimize the problems due to the pion pole, while at the same time, minimize possible rescattering contributions.

1.13.7 Pion excess

Excess pions may be present in nuclei due to the pion-exchange forces between nucleons [54]. An energy dependence in the A(e,e$'\pi^+$) nuclear transparency could be interpreted as an energy dependence of the density of the pion field in nuclei. An experiment that searched for the pion excess in nuclei [55] did not rule out or confirm the existence of this effect. Friman *et al.* [54] used a static one-pion exchange potential to show that the pion excess can be as large as 10% at $k_\pi = 0.43$ GeV/c. If the pion excess exists, it will increase the nuclear transparency in πCT near $Q^2 = 2.15$ (GeV/c)^2 ($k_\pi = 0.41$ GeV/c) and then have the opposite dependence to the color transparency signal at larger Q^2.

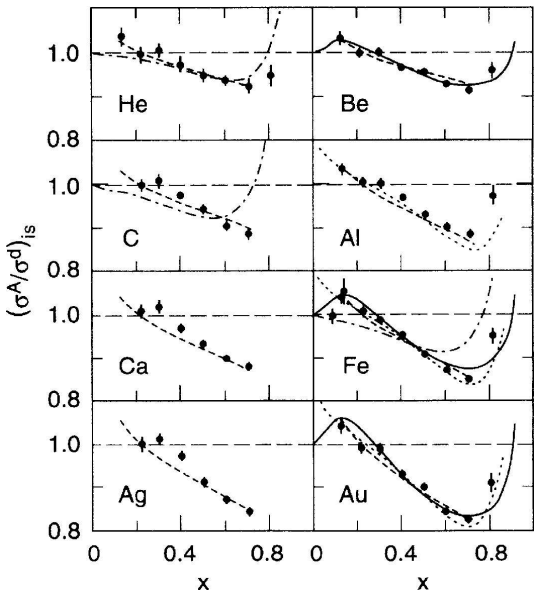

Figure 1-16: The cross section ratios for isoscalar targets as a fuction of $x = Q^2/(2M\nu)$. The cross section ratios are not constant and equal to 1, which is a result of the EMC effect. The circles are experimental data from Ref. [56] and the errors bars are the combined statistical and point-to-point systematic errors. The figure is from Ref. [56].

1.13.8 Medium modification of nucleons

The effect discovered by the European-Muon Collaboration (EMC effect) showed that the distribution of quarks in a nucleus was different from the distribution of quarks in a nucleon [56], due to nuclear effects. The inclusive cross sections from nuclei divided by the inclusive cross section from deuterium are shown in Figure 1-16. In πCT, the range of x was 0.21-0.54 (Table 2.4), where the inclusive cross section ratio decreased by approximately 10%. The impact of the EMC effect on the cross sections in πCT was expected to be smaller than 10% because a pion was detected in coincidence with the electron. In addition, the cross section ratio had a negative slope for the range of x in πCT which could have caused a change in the nuclear transparency that was opposite to the color transparency signal.

The EMC effect describes how the influence of the nuclear medium changes the quark distributions inside a nucleon. A similar effect is the change in the nucleon structure functions due to the binding of the nucleon. This is typically incorporated in A(e,e′p) using the off-shell prescription due to T. de Forest [57]. However, no such prescription exists for A(e,e′π^+) and the results in πCT did not include corrections for medium modification

of the elementary cross section. As we were searching for a Q^2 dependence in the nuclear transparency, this approximation was acceptable if the effect did not change with Q^2. Longitudinal-Transverse (L-T) separations were performed at $Q^2 = 2.15$ and 4.0 $(\mathrm{GeV/c})^2$ in πCT (Table 2.4). The goal of the L-T separation was to verify that the L-T character did not appreciably change from the hydrogen target to targets with $A > 1$, and was an important check of the quasifree approximations.

1.13.9 Spectroscopic strength

Measurements from A(e,e′p) revealed that spectroscopic factors were quenched by approximately 30-35% compared to mean-field values [58, 59]. A possible explanation for this discrepancy was that correlations moved some of the single particle strength to orbitals above the Fermi energy. Measurements at high Q^2 showed that the spectroscopic factors were momentum-transfer dependent [60] and no significant quenching was seen at $2 \leq Q^2 \leq 4$ $(\mathrm{GeV/c})^2$ in exclusive (e,e′p) reactions [61]. This type of effect was very important when the nuclear transparency was extracted in A(e,e′p) reactions with cuts on the momentum of the struck nucleon. However, the nuclear transparency extracted from A(e,e′π^+) was less susceptible to these effects because the cross section involved an integration over all E_m and $\mathbf{p}_m$ (Equation 1.17). Different spectral functions, including those with and without correlations, were tested to quantify the effect due to the Q^2 dependence of the spectroscopic factors.

Chapter 2

Experimental Apparatus

The πCT experiment was performed in Hall C at the Thomas Jefferson National Accelerator Facility (JLab). The standard Hall C equipment, including the solid target ladder, was used. A Continuous Wave (CW) beam was produced by the accelerator at beam energies up to 5.8 GeV. The beam position and current were monitored by the standard beam line instrumentation of Hall C. The electron beam was incident on stationary nuclei in the target, and the target material could be changed by moving the target ladder. The scattered electron and the π^+ produced in the reaction were detected in coincidence using the SOS and HMS spectrometers. The target material was unpolarized, and the electron beam was unpolarized when averaged over time. The signals from the detectors were relayed to the Hall C counting house, where they were processed by the trigger electronics and recorded by the data acquisition system.

A brief description of the equipment used in πCT will follow in this chapter, and more detailed descriptions can be found in Refs. [62, 63, 31, 64].

2.1 Accelerator

The electron beam was accelerated using superconducting Radio Frequency (RF) cavities in a configuration that resembles a racetrack, as shown in Fig. 2-1. Electrons were injected into the North Linac at 56 MeV and were accelerated in the North and South Linacs. Superconducting magnets in the West and East Arcs circulated the beam. The beam passed through each linac up to 5 times with an increase in energy of up to 1.15 GeV

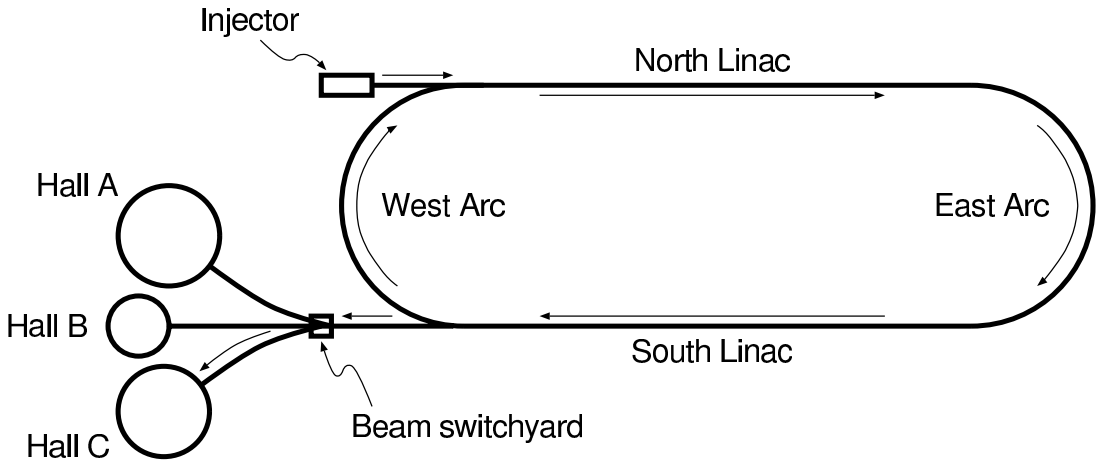

Figure 2-1: Schematic of the electron accelerator (figure from Ref. [64]).

after each pass. The beams from each pass were separated in the recirculation arcs using RF separators, transported separately in the arc and recombined at the entrance to each successive linac. The beam energies used in the experiment were 5.767, 5.012 and 4.021 GeV.

The beam current in the experiment was 35-80 μA, and the duty factor of the beam was almost 100%. The beam's microstructure consisted of pulses occurring at a frequency of 1497 MHz. The nominal bunchlength was 1/360 of the period between bunches (approximately 2 ps). Each bunch was maintained as small as possible because a longer bunchlength caused a larger energy spread in the beam due to the difference in accelerating gradients in the RF cavities at the front and rear of a bunch. The energy spread of the beam was $\pm$0.025%. At the Beam Switchyard, the beam was split to three experimental halls in which each hall could operate simultaneously with different beam energies. Every third pulse was delivered to Hall C, with a frequency of 499 MHz.

2.2 Hall C Arc

The beam position, profile, energy and current were measured in the Hall C arc (Fig. 2-2). In addition, the beam was rastered over an area of the target of up to 2$\times$2 mm^2 by the Fast

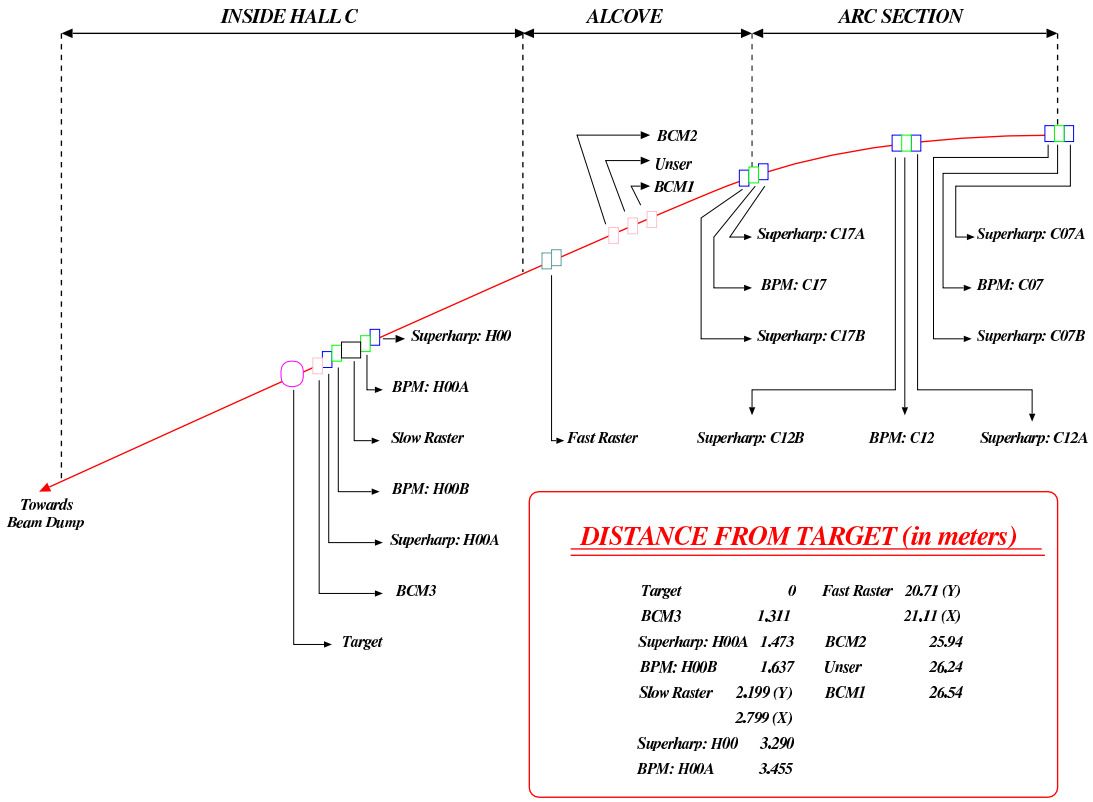

Figure 2-2: Top view of the Hall C beam line showing the equipment used in transporting the beam from the beam switchyard to the target (figure from Ref. [31]).

Raster. The raster was necessary to reach acceptable beam currents without damaging the target and to reduce the effect of localized boiling in the liquid targets.

The beam position was continuously monitored during data collection using the non-destructive Beam-Position Monitors (BPM) H00A and H00B to ensure that the beam was centered on the target. The transverse beam size was measured using the destructive superharp scanner H00A and the beam diameter was 60-130 μm, which was much smaller than the raster size. The BPMs and superharps could measure the beam position with a precision of 0.2 mm and 0.01 mm respectively.

Using the bending magnets of the Hall C arc, the relative beam energy could be measured with a precision of $\Delta E/E \approx 10^{-4}$. The beam energy could be determined absolutely to a precision of 10^{-3} by measuring the angle and/or momentum of outgoing particles in reactions where these properties are kinematically constrained by the beam energy. The

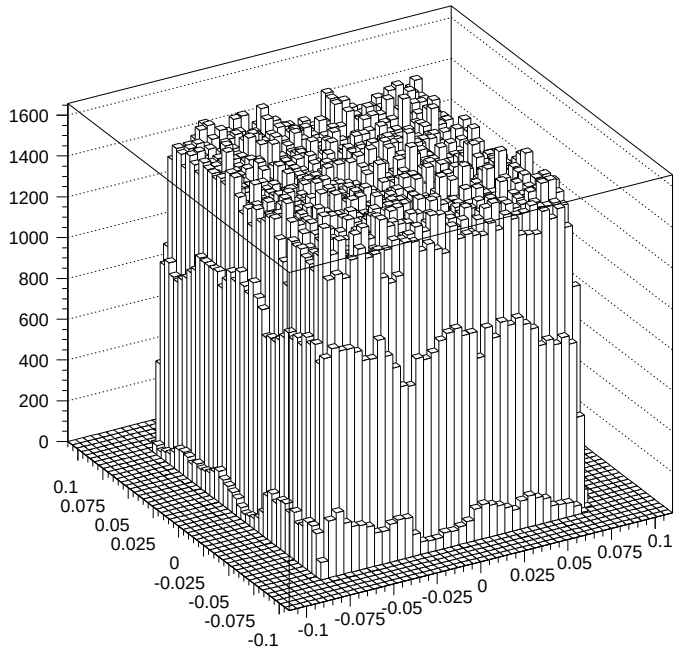

Figure 2-3: Histogram of the vertical fast raster position [cm] vs. horizontal fast raster position [cm].

most precise method is the diffractive minima method [62].

The beam current was monitored through a combination of a parametric DC current transformer (Unser monitor) and coupled resonant cavities (BCM1 and BCM2). The BCMs provided stable and linear output vs. the beam current while the Unser monitor was used to provide an absolute calibration for the BCMs. The baseline (zero current) signal from the Unser monitor drifted slowly over several minutes, and so was not used once the BCMs were calibrated.

The BCMs consisted of cylindrical cavities with holes at each end to allow the beam to pass through. The cavities were designed with a resonant frequency equal to the bunch frequency of the beam. An antenna in the cavity coupled to the TEM_{010} mode produced a signal proportional to the beam current. BCM1 was less reliable than BCM2 and used a power meter to directly measure the electrical power from the antenna. BCM2 was more linear than BCM1 through the use of a high precision RMS to DC converter followed by a DC to frequency converter. The frequency signal was then counted in a scaler. BCM2 was used to extract the cumulative charge for the data analysis.

The BCMs were calibrated using the Unser monitor during πCT and during experi-

ments that ran immediately before and after the πCT running periods. A global fit of the calibration coefficients was determined for these calibrations and the residual had a standard deviation of 0.3 μA. The beam current in πCT was 35-80 μA, and therefore, the point-to-point uncertainty in the cumulative charge delivered by the beam was estimated to be 0.4-0.9%. The normalization uncertainty, which comes from the Unser monitor, was estimated to be 0.4% [65].

The raster pattern used for all targets was uniform over a 2 mm $\times$ 2 mm square. The current in the fast raster magnets were monitored and the position of the beam was fed into the data stream for each event. The reconstruction could therefore be corrected for the vertical position of the beam, event-by-event. An image of the raster pattern is shown in Fig. 2-3

2.3 Target

The standard Hall C cryogenic target ladder and optics sled was used in πCT (Fig. 2-4). For the July 2004 running period, Loop 1 was filled with liquid hydrogen and Loop 2 was filled with liquid deuterium. Loop 3 was unused. For the December 2004 running period, Loop 1 was unused, Loop 2 was filled with liquid hydrogen and Loop 3 was filled with liquid deuterium. The liquid targets were cylindrical with a diameter of $\sim$4 cm (see Table 2.1) and the axis of the cylinder was vertical (the "tuna can"). The cans were made of aluminum 0.12 mm thick, which contributed to energy loss of the beam as it entered the cell and the scattered particles as they exited the cell, and also produced events in the spectrometer that came from interactions between the beam and the cell wall.

The cryogenic target ladder could be translated vertically by lifter motors. The ladder could be positioned so that the beam interacted with any of the liquid or solid targets in the ladder. The optics sled contained a dummy target, which consisted of two aluminum foils placed 4 cm apart in order to determine the effects of the cell wall on the yields from the liquid targets. The yields from the liquid alone could be determined by subtracting the yield from the dummy target from the yield from the liquid target (after suitable scaling because the dummy target foil thickness was approximately 7 times thicker than the walls of the liquid target). The solid target ladder was attached above the optics sled containing target foils of naturally occurring isotopic abundances of carbon, copper and gold. All foils

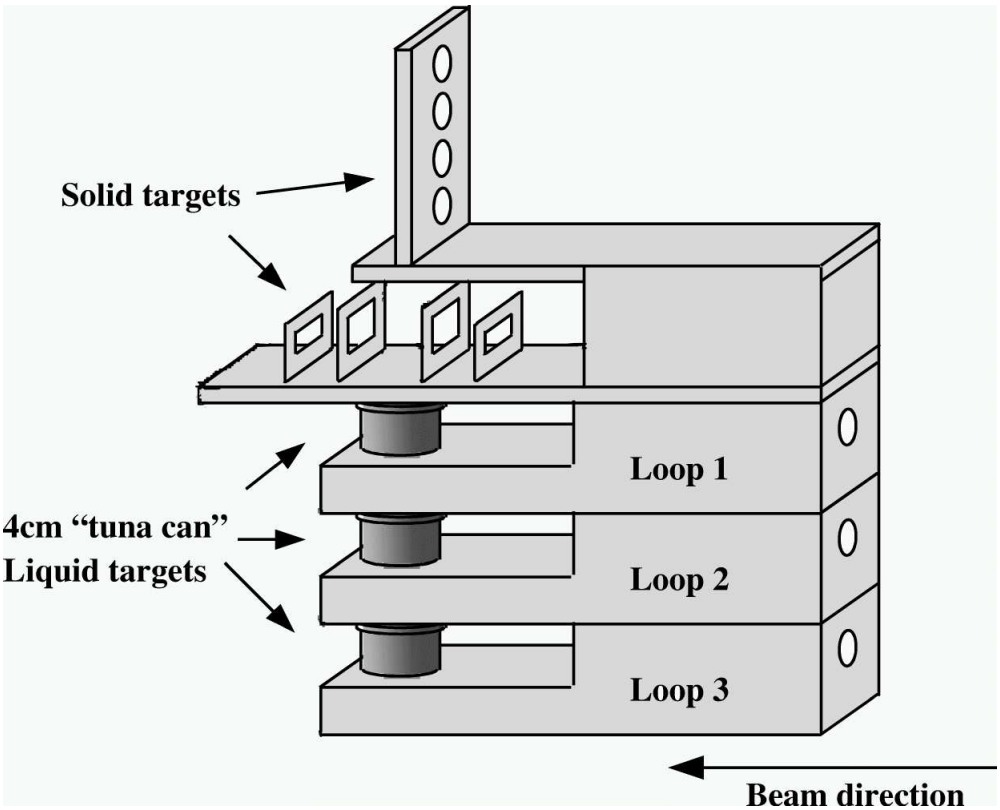

Figure 2-4: Schematic of the target ladder.

in the solid target ladder were separated vertically.

The temperature and pressure of the liquid targets affect the density and the contraction of the aluminum cell walls, which in turn affects the thickness. The temperatures of the cryogenic loops of hydrogen and deuterium were regulated with fluctuations up to 0.02 K. During the July running period, the temperatures of the hydrogen and deuterium targets were 18.60 and 22.00 K, respectively. During the December running period, the temperatures were 19.00 and 22.00 K for the hydrogen and deuterium targets, respectively. Each liquid target was connected to a large ballast tank, which was not cryogenic and was available to store the target liquid if it warmed up or in an emergency. The pressure of the gas in the ballast tank, which was also the pressure of the liquid, fluctuated by up to 1 psia and the effect on the density was negligible (the liquid was almost incompressible). The pressure was 24 psia for hydrogen and 21 psia for deuterium during the July running period, and 22 psia for both hydrogen and deuterium during the December running period. The thicknesses and associated uncertainties of the liquid targets are described in Table 2.1.

Target	18.6K H_2 Loop 1	19K H_2 Loop 2	D_2 Loop 2	D_2 Loop 3
Thickness (g/cm^2)	0.2858	0.2860	0.6587	0.6617
Inner diameter (cm)	3.930	3.956	3.935	3.953
Purity (%)	>99.99	>99.99	>99.95	>99.95
Boiling correction (%)	0.6	0.6	0.6	0.6
Beam path length (%)	0.6	0.6	0.6	0.6
Equation of state (%)	0.5	0.5	0.5	0.5
Total uncertainty (%)	1.0	1.0	1.0	1.0

Table 2.1: Nominal liquid target thicknesses and associated total uncertainty. The thickness values are not corrected for beam offsets.

Target	C	Al, foil 1	Al, foil 2	Cu	Au
Thickness (g/cm^2)	0.6667	0.2626	0.2633	0.7986	0.3795
Purity (%)	99.95	98	98	99.995	99.999
Total uncertainty (%)	0.5	0.5	0.5	0.5	0.5

Table 2.2: Nominal solid target thicknesses and associated total uncertainty.

The solid targets are described in Table 2.2.

The cryogenic cells were cylinders and as the beam did not pass through the axis of the cylinder, the beam traversed a reduced path length through the target. The uncertainty in the absolute beam position relative to the axis of the cylinder was approximately 0.2 mm. The target thickness was corrected for any known offsets and the uncertainty in the beam path length was estimated at 0.6% using the uncertainty in the beam position. The thickness of the solid targets were calculated using measurements of the mass and area of the targets. The uncertainty of the solid target thicknesses were estimated from the uncertainty in these measurements. The uncertainty due to the target boiling is discussed in Section 3.11.

After passing through the target, the beam was transported to a beam dump in the experimental hall via the "small diameter" beam pipe (d=2 in). The small diameter beam pipe was used to allow the High-Momentum Spectrometer (Section 2.4.1) to rotate to the smallest opening angle used in the experiment ($\theta_{HMS} = 10.6^\circ$).

2.4 Spectrometers

The reaction studied was A(e,e′π^+) and the scattered electron (e′) was detected in the Short-Orbit Spectrometer (SOS) while the π^+ was detected in coincidence in the High-Momentum Spectrometer (HMS). Bending magnets and wire chambers in each spectrometer allowed the determination of the particle's momentum, while gas and aerogel detectors were employed to select the desired particles. In addition, plastic scintillators with < 1 ns time resolution provided the difference in the time-of-flight between the e′ and the π^+ and were also used for triggering in each spectrometer.

2.4.1 High-Momentum Spectrometer (HMS)

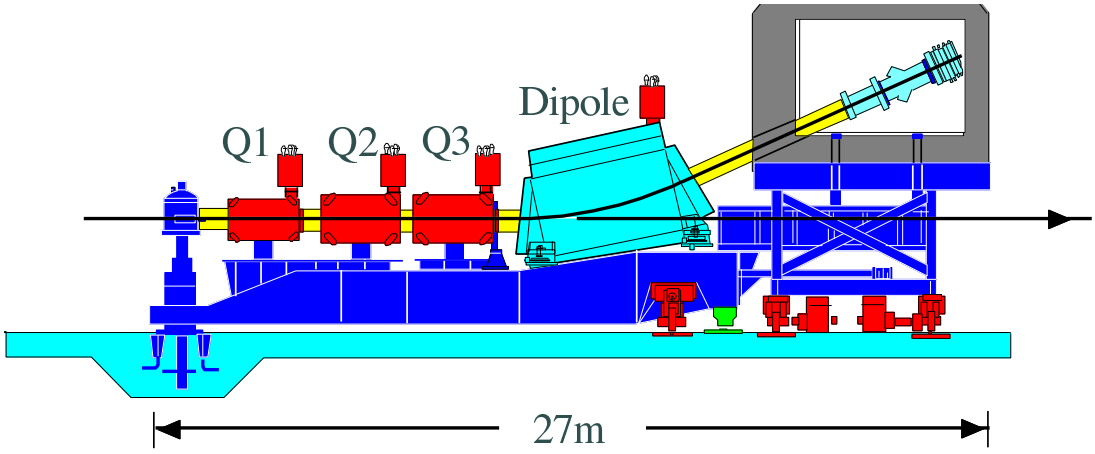

Figure 2-5: Side view of the HMS (figure from Ref. [31]).

The HMS uses four superconducting magnetic elements to focus and separate particles based on their momentum and charge (Fig. 2-5). The magnetic elements consisted of three quadrupoles followed by a dipole (QQQD). The HMS was rotated about the target, and angles between 10.6° to 20.0° were used with momentum settings between 2.1-4.4 (GeV/c). The resolution of the momentum and the in-plane and out-of-plane scattering angles was 0.2%, 0.8 mrad and 1.2 mrad respectively. At a particular setting, the nominal momentum acceptance was ±10% of the central momentum and the nominal angular acceptance was ±40 mrad in plane and ±75 mrad out of plane. The configuration of the detectors in the HMS is shown in Fig. 2-6, and will be discussed further in Sec. 2.4.3.

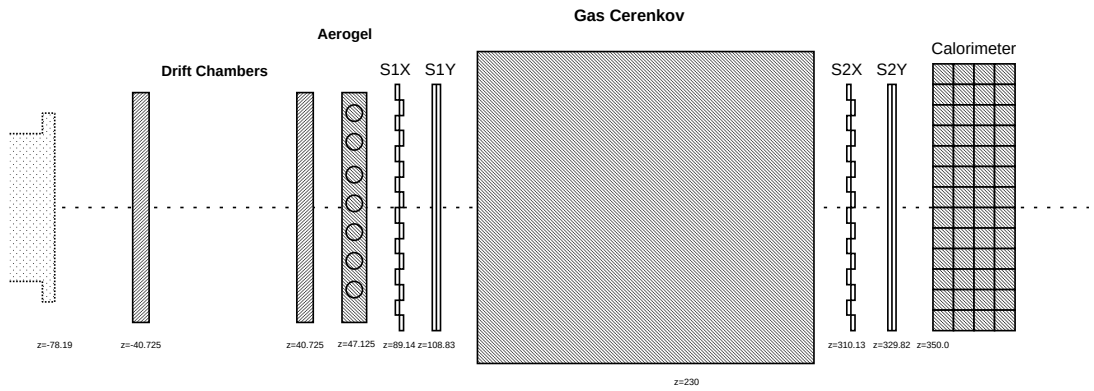

Figure 2-6: Configuration of the detectors in the HMS (figure from Ref. [65]).

2.4.2 Short-Orbit Spectrometer (SOS)

The SOS contained three room temperature magnetic elements, a quadrupole followed by two dipoles (QDD) (Fig. 2-7). The SOS was rotated about the target, and angles between 27.8° to 55.9° were used with momentum settings between 0.73-1.73 (GeV/c). The resolution of the momentum and the in-plane and out-of-plane scattering angles was 0.15%, 2.5 mrad and 0.5 mrad respectively. At a particular setting, the nominal momentum acceptance was +15% to −10% of the central momentum and the nominal angular acceptance was ±70 mrad in plane and ±40 mrad out of plane. The distance from the target to the center of the detector hut was approximately 10 m. The configuration of the detectors in SOS hut was very similar to the HMS, shown in Fig 2-6. The distances between the detector elements were slightly different in the SOS compared to this figure and no aerogel Cerenkov detector was used in the SOS.

2.4.3 Detector packages

The HMS and SOS each contained two wire (or drift) chambers that were separated by 81.5 cm in the HMS and 49.5 cm in the SOS. The chambers were located outside of the magnetic fields of the spectrometer magnetic elements. The position and angle of a track could be determined using the two wire chambers in a given spectrometer. Each chamber consisted of 6 planes of wires and the gas surrounding the wires was a mixture of argon and ethane in the ratio of 1:1. The position resolutions of the HMS and SOS drift chambers

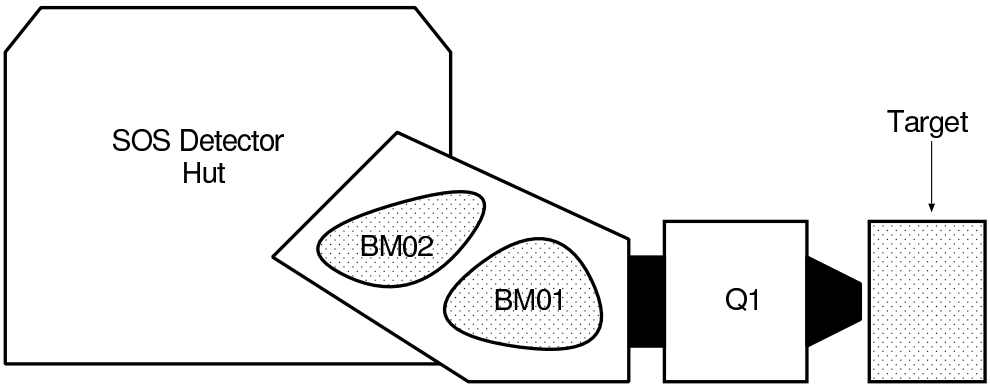

Figure 2-7: Side view of the SOS (figure from Ref. [31]).

were 280 μm and 180 μm respectively.

The HMS and SOS detector huts contained planes of fast scintillators. The planes were grouped into pairs, with one pair directly behind the drift chambers and another pair separated by 250 cm in the HMS and 180 cm in the SOS. Each detector hut therefore contained four planes of scintillators. A particle that passed along the central ray of a given spectrometer was expected to produce signals in each of the four planes. The time-of-flight of a particle between the planes was not used in πCT except to calibrate the timing of the scintillator paddles. The coincidence time, which was the relative timing between the spectrometers was used in πCT. The FWHM of the coincidence time was 200-300 ps for e-π^+ events.

Threshold Cerenkov detectors were employed for e-π-K-p separation in each spectrometer. The HMS contained a gas Cerenkov filled with 0.956 atm of perfluorobutane (C_4F_{10}). It had an index of refraction of 1.00137 and a momentum threshold of 2.65 (GeV/c) for π^+ and a threshold of 9.4 (GeV/c) for K^+. The maximum HMS central momentum setting was 4.4 (GeV/c) so that the Cerenkov detector could be used to identify π^+ except for settings with the central momentum below 3.1 (GeV/c). For these settings, the π^+ velocity was close to or below the threshold for particles within the acceptance. Positrons did not need to be separated from pions in the HMS because the coincidence requirement with an electron in the SOS removed positron events.

An aerogel Cerenkov detector was installed in the HMS for πCT to separate π^+ from K^+ for central momentum settings below 3.1 (GeV/c). The aerogel had an index of refraction of

1.015 and so had a threshold for π^+ of 0.8 (GeV/c) and a threshold for K^+ of 2.85 (GeV/c). Two kinematic settings had the central HMS momentum below 3.1 (GeV/c), the Q^2 = 1.10 $(GeV/c)^2$ setting and the W vs. k_π test point, which had central HMS momenta 2.793 (GeV/c) and 2.074 (GeV/c), respectively. The HMS momentum acceptance at the Q^2 = 1.10 $(GeV/c)^2$ setting extended up to 3.016 (GeV/c), which is above the aerogel momentum threshold for kaons. Therefore, it may be possible for kaons to pass all of the particle identification cuts in the HMS at this setting and be misidentified as pions. However, events where kaons were misidentified as pions were an insignificant background because the cross section for producing kaons at this setting is only a few percent of pion production cross section and they were reconstructed with a missing mass much larger than the double pion production threshold. So, these events were removed by the double pion missing mass cut (Section 3.2).

The SOS contained a gas Cerenkov which was used to separate electrons from π^- particles. The existing ("Old") Cerenkov detector was used during the July running period. This detector was replaced with a "New" Cerenkov detector for other experiments, and was used during πCT in the December running period. The two Cerenkov detectors are compared in Table 2.3. The maximum momentum setting of the SOS was 1.73 (GeV/c) (with momentum acceptance up to 1.99 (GeV/c)) during July, which was well below the 3 (GeV/c) momentum threshold for pions. The pion threshold in the New Cerenkov detector was also larger than the pion momenta detected in the SOS during the December running period.

Lead glass calorimeter stacks existed at the back of HMS and SOS detector huts and signals from these detectors were not used in πCT, except to calibrate the SOS gas Cerenkov detector. Electrons impinging on the calorimeter caused cascades of secondary electrons and the primary electrons rapidly lost their energy within one or two blocks of lead glass. The signal from the calorimeter was calibrated to give the total energy deposited by these events (where the energy was also determined from the momentum of the electron). Hadrons, such as pions, tended to punch through the calorimeter and deposited only a fraction of their energy. The calorimeter therefore provided particle identification between electrons and hadrons independent of the Cerenkov detectors.

Gas Cerenkov	Old	New
Running period	July	December
Window-to-window length (cm)	111	99.4
Width (cm)	73.7	110
Height (cm)	99	110
Window material	2×(254 μm Lexan graphics film and 50.8 μm Tedlar film)	2×(0.762 mm Al)
Window thickness	2×39 mg/cm^2	2×206 mg/cm^2
Gas	Freon-12 (CCl_2F_2)	Perfluorobutane (C_4F_{10})
Pressure (atm)	1.0	1.41
n	1.00108	1.0019
Electron threshold	11 (MeV/c)	8.3 (MeV/c)
Pion threshold	3 (GeV/c)	2.27 (GeV/c)
Entrance	11" high, 24" wide and 12" half circles above and below	22" high, 14" wide and 7" half circles above and below
NPE for relativistic particles	10-11	44

Table 2.3: Description of the Old and New SOS gas Cerenkov detectors.

2.4.4 Trigger configuration

The purpose of the trigger electronics was to provide an electronic pulse (also called the trigger) whenever certain combinations of detector elements had events within a narrow time window (gate width). The single arm trigger logic of the HMS and the SOS is shown in Figure 2-8. To output a signal, the SCIN logic unit required 3 out of 4 scintillator planes to have hits in a given spectrometer. Similarly, the ELLO and ELHI logic units required a combination of detector hits to output a signal, as shown in Figure 2-8. The ELREAL condition was satisfied when the ELLO and/or ELHI logic units outputted an electronic pulse. For πCT this trigger requirement was SCIN (3/4) in the HMS and ELREAL in the SOS. The gate width was small enough to limit the electronic dead time, but long enough to ensure that all the detectors associated with an event that are required for the trigger have enough time to arrive at the electronics. The gate width was 60 ns during πCT.

The SOS (which was detecting scattered electrons) formed a trigger on an event if the conditions for ELLO or ELHI were met. To satisfy the ELLO condition, the gas Cerenkov detector had to detect an event, and either three out of four scintillator planes had to register hits (SCIN 3/4), or a combination of scintillator planes and the calorimeter had to

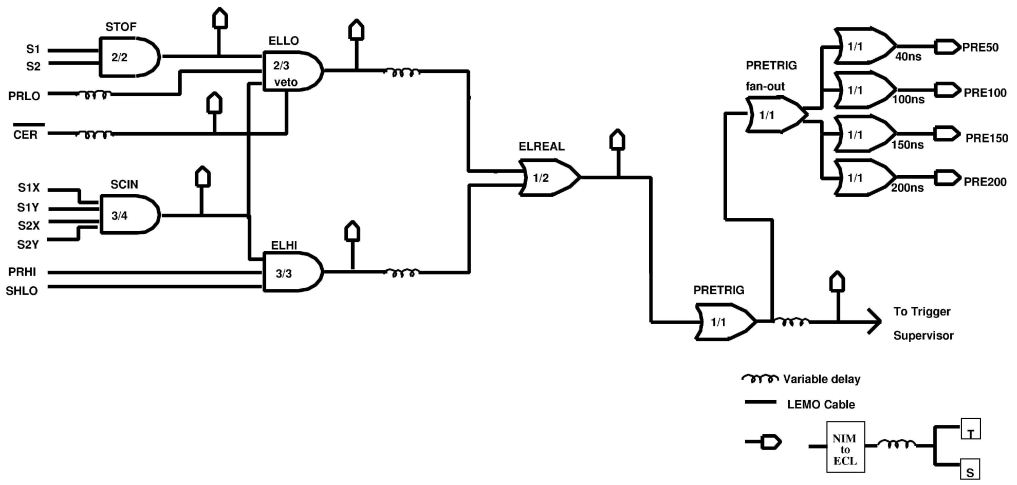

Figure 2-8: Single-arm trigger electronics configuration [65]. For the SOS, the output from ELREAL was used as the input for the pretrigger (PRETRIG). For the HMS, the ELHI, ELLO and ELREAL logic was bypassed so that the SCIN 3/4 was the input to the pretrigger.

register hits. The PRLO signal (it is called the PRLO signal, because the voltage threshold of the discriminator was low) came from the first layer of calorimeter lead glass bars, where the electrons were expected to create electron showers. The ELLO condition was almost always met with electrons by satisfying the SCIN 3/4 condition and the requirement that the gas Cerenkov detected an event. Other combinations of detectors were used in the trigger so that the efficiency of each detector element could be determined.

The ELHI signal provided redundancy in the trigger because its signal was independent of the gas Cerenkov. This allowed one to determine the efficiency of this detector in the analysis. The ELHI condition was satisfied when three out of four scintillator planes registered hits, the preshower signal passed a high voltage threshold (PRHI) and the summed signal from the lead glass calorimeter passed a low voltage threshold.

The outputs from the single-arm trigger electronics were used in the coincidence trigger (Figure 2-9). The HMS and SOS pretrigger signals were sent to an 8LM LeCroy programmable logic unit. The status of the trigger supervisor (which will be described next) was also sent to the 8LM to prevent events from overlapping. The 8LM determined if the event was either a coincidence event, an HMS single arm event or a SOS single arm event.

The output from the 8LM was sent to the trigger supervisor where prescaling of the single arm events could be accomplished to reduce the computer dead time. The trigger

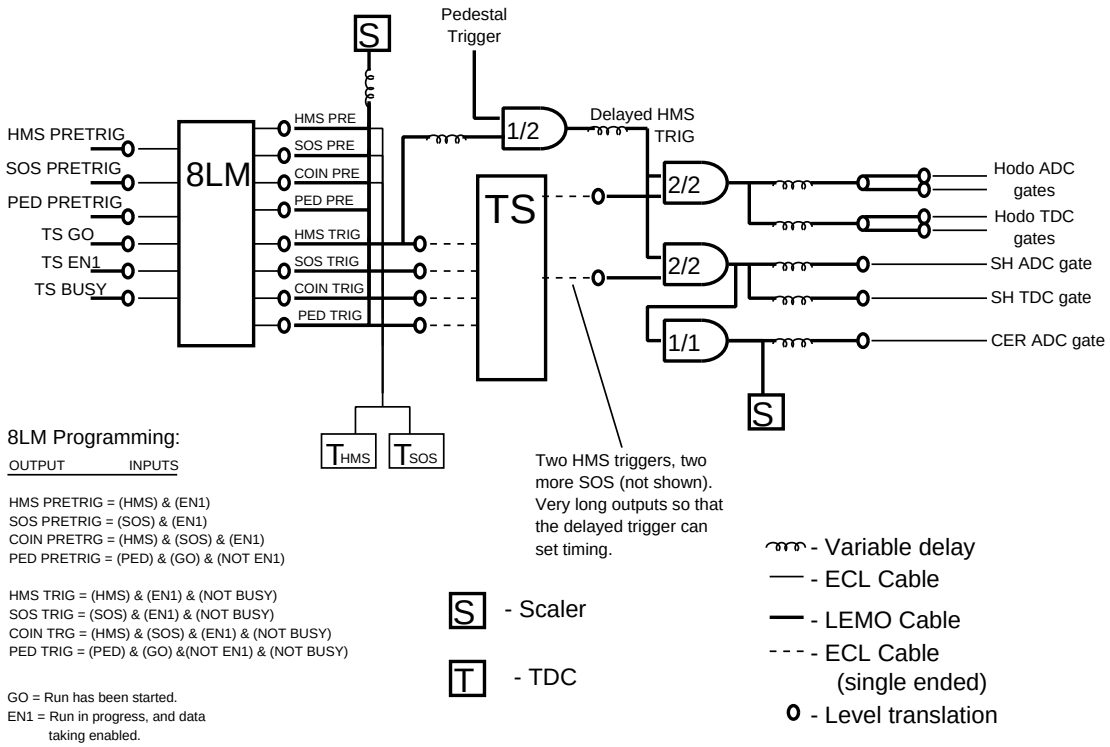

Figure 2-9: Configuration of the trigger supervisor and coincidence trigger electronics (figure from Ref. [31]).

supervisor outputted two signals for the HMS and two for the SOS with very long gate widths. The gate width was determined by the time required for the data acquisition and was limited to a maximum of 100 μs. TRIG signals split off before the trigger supervisor were delayed and then ANDed with the output from the trigger supervisor (only the delayed HMS TRIG is shown). The ANDed signal for the HMS provided the TDC start signal for the HMS TDCs, and the same procedure was used for the SOS. In this way, the start time for the TDCs of each spectrometer did not depend on the timing of the coincidence gate. The ANDed signals were also used to enable the readout of the ADC modules.

Signals from the photomultiplier tubes (PMTs), which were used on the fast scintillator planes, Cerenkov detectors and lead-glass calorimeters, were sparsified. Dark current in PMTs caused a DC shift in the current signal vs. time. The current integrated over the time that the ADC was enabled was therefore the sum of the charge from the signal plus the integral of the dark current over the gate width. The charge from the dark current in a given event, the pedestal, was usually constant with time. To reduce the rate of data

written to disk, signals from PMTs that were within the pedestal peak were not recorded

There was, however, a risk with sparsification that a detector may become very inefficient, because real events may be identified as the pedestal. To limit this problem, the pedestals of all the PMTs were checked at the beginning of each run (each run was usually 30-60 min). The first 1000 events of each run were triggered by an electronic pulser and the ADCs were read out for each PMT. The pulser signal was called the pedestal trigger. Because no signal was expected in the current from a given PMT, the pedestal was measured in these events. The measured pedestals were compared to those used in the sparsification and the run was stopped if significant discrepancies were seen, and the pedestal positions were updated if necessary.

2.5 Kinematic settings

The central kinematics of πCT are shown in Table 2.4. In addition to the kinematics shown, data were taken with a hydrogen target and with the HMS (Section 2.4.1) rotated from the central kinematics by an amount comparable to the spectrometer acceptance. The spectrometer was rotated to both larger angles (plus side) and smaller angles (minus side), however, some settings at the minus side could not be performed because the central setting was already at the smallest possible HMS angle. The plus and minus side measurements were performed to better constrain the fitting of the elementary pion cross section model.

Q^2	W	$-t$	E_e	$\theta_{e'}^{\rm SOS}$	$E_{e'}$	θ_q	$\theta_{\rm HMS}$	p_π	k_π	ϵ	x
1.10	2.26	0.050	4.021	27.76	1.190	10.58	10.61	2.793	0.23	0.50	0.21
2.15	2.21	0.158	5.012	28.85	1.730	13.44	13.44	3.187	0.41	0.56	0.35
3.00	2.14	0.289	5.012	37.77	1.430	12.74	12.74	3.418	0.56	0.45	0.45
3.91	2.26	0.413	5.767	40.38	1.423	11.53	11.53	4.077	0.70	0.39	0.50
4.69	2.25	0.527	5.767	52.67	1.034	9.09	10.63	4.412	0.79	0.26	0.54
2.16*	2.21	0.164	4.021	50.76	0.730	9.03	10.60	3.187	0.42	0.27	0.35
4.01*	2.14	0.441	5.012	55.88	0.910	9.50	10.55	3.857	0.71	0.25	0.52
2.16†	1.74	0.374	4.021	32.32	1.730	19.99	19.99	2.074	0.65	0.63	0.50

Table 2.4: πCT central kinematics; θ_q is the angle between $\mathbf{q}$ and the beam direction in the lab frame, k_π is the magnitude of the three momentum of the virtual struck pion in the quasifree knockout picture, and $x = Q^2/(2M\nu)$. Kinematics labeled with * are the low epsilon points used for L-T separations and the setting labeled with † is the W vs. k_π test point. The HMS and SOS are described in Section 2.4. Energy is given in GeV, momentum in GeV/c, mass in GeV/c^2 and angles are in degrees.

Chapter 3

Data analysis

The goal of the πCT data analysis was to determine the normalized yields from the raw data files produced during the experiment. The normalized yield is the number of events that pass a given set of cuts divided by the cumulative charge delivered by the beam after correcting for the efficiency of the detectors. The standard Hall C analysis code, called the Engine, was used to process these raw data files. The Engine performs reconstruction of events using the raw wire chamber and other detector signals and stores the output in a summary file. The summary file contains the reconstructed kinematics for each event along with other useful information such as the charge delivered by the beam. Corrections to the data include kinematic corrections and normalization corrections. Kinematic corrections are concerned with optimizing the accuracy of reconstructed quantities. Normalization corrections are applied in order to determining normalized yields and absolute cross sections, such as detector efficiencies and corrections to the target thickness. The steps involved in determining the normalized yields will be described in this chapter.

3.1 Event reconstruction

The spectrometer quantities, x, y, x' and y', could be deduced from reconstruction of the wire chamber data. These quantities are the vertical and horizontal positions of the track at the midpoint between the wire chambers, and the gradients of the track with respect to the spectrometer central ray. The target quantities, y_{tar}, x'_{tar}, y'_{tar} and δ were determined from the spectrometer quantities by suitable transformation functions. These quantities

are the horizontal position of the event, the horizontal and vertical gradients of the track with respect to the spectrometer central ray and the momentum of the particle given as a percentage above the central momentum setting of the spectrometer, respectively. The transformations are given by

$$\begin{aligned} y_{tar} &= f_1(x, y, x', y'), \\ x'_{tar} &= f_2(x, y, x', y'), \\ y'_{tar} &= f_3(x, y, x', y'), \text{ and,} \\ \delta &= f_4(x, y, x', y'). \end{aligned} \tag{3.1}$$

The transformation matrix can be determined theoretically based on the configuration of the magnets in a given spectrometer. Another, more accurate, method is to optimize the matrix with a specially prepared data set and surveys of the spectrometers. The latter method cannot be performed, however, without some reasonable starting transformation, which the theoretical transformation matrix provides. The transformation functions, f_i, are parameterized as a sum of polynomials of the spectrometer quantities, with up to 6th order polynomials used. The coefficients of the polynomials comprise the optics matrix, M, given by

$$x^i_{tar} = f_i(x, y, x', y') \approx \sum_{j,k,l,m}^{j+k+l+m \leq 6} M^i_{jklm} (x)^j (y)^k (x')^l (y')^m. \tag{3.2}$$

The parameterization for f_1 can be optimized by a data set consisting of a series of foil targets placed at well determined positions in the target region. The parameterization for f_1 can then be optimized to make a histogram of y_{tar} as narrow as possible and close to the foil position. Similarly, the parameterization of f_2 and f_3 can be optimized using a data set consisting of sieve slit runs with the same foils used to optimize y_{tar}. The sieve collimators contain small holes and are placed in the zero-magnetic field region between the target and the first magnet of a given spectrometer. Surveyed positions of the foils and the sieve holes allow one to determine the angle of tracks at the target and optimize the angle matrix elements. Following optimization of the angles, the parameterization of f_4 can be accomplished by a series of hydrogen elastic runs. The constrained kinematics allows one to determine the momentum of the particles using x'_{tar} and y'_{tar}, and therefore optimize the δ matrix elements.

When fitting matrix elements, the zeroth order matrix elements (M^i_{0000}) are always

Matrix name	P_{SOS} during δ optimization (GeV/c)	P_{SOS} during angle optimization (GeV/c)	P_{SOS} range (GeV/c)
900	0.9	1.65	0.1 to 1.1
Default	1.45	1.65	1.1 to 1.7
1740	1.74	1.65	1.7 to 1.8
1200	0.9	1.2	Not used

Table 3.1: Matrices available for the reconstruction of SOS target quantities, the settings at which these matrices were optimized and the range in the central SOS momentum setting (P_{SOS}) over which the matrices produce the best agreement with surveys of the hall.

discarded. The reason is that the zeroth order matrix elements represent a global offset of the spectrometer, such as the out-of-plane spectrometer offset. These offsets can be more accurately determined using hydrogen elastic coincidence runs (heep check), they can be parameterized as functions of the central spectrometer settings, and parameterizations of the offsets generally do not need to be changed when matrices are changed.

3.1.1 SOS optics matrix

A number of SOS matrices were available to transform the reconstructed spectrometer quantities (x, y, x' and y') into target quantities (y_{tar}, x'_{tar}, y'_{tar} and δ). These matrices were called 900, Default, 1740 and 1200, and the central momentum range over which these matrices were used in the πCT analysis are described in Table 3.1. The 900, default and 1740 matrix share the same angle matrix elements. To help correct for saturation effects (Section 3.1.2), a parameterization was developed by X. Chuncheng [66] to correct y_{tar}, x'_{tar} and y'_{tar} for $P_{SOS} \neq 1.65$ (GeV/c). This parameterization was used whenever the 900, default or 1740 matrices were used.

The 1200 matrix was optimized as part of the πCT analysis, while the other matrices were available before the experiment. This matrix was tested using optics data taken at $P_{SOS} = 1.2$ (GeV/c) and the standard deviation of the reconstructed in-plane scattering angle was 0.88 mrad and the out-of plane scattering angle was 0.31 mrad. The standard deviations of the in-plane and out-of-plane scattering angles using the Default matrix were 0.93 mrad and 0.20 mrad, respectively. The improvement using the new matrix was marginal in the in-plane angle and worse in the out-of-plane angle, and so the 1200 matrix was not

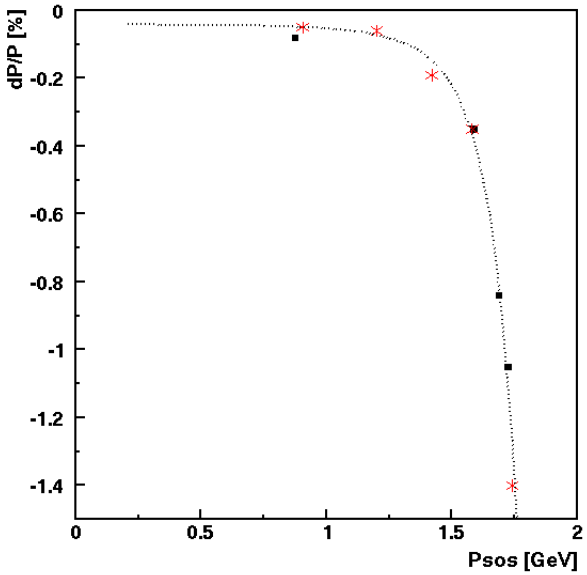

Figure 3-1: SOS field correction. The observed correction to the SOS central momentum during πCT (squares) and 2003 (stars). The dotted line is the parameterization of the 2003 data, and was not modified for πCT.

used.

3.1.2 SOS saturation corrections

The room temperature magnets in the SOS spectrometer contain iron cores that produce saturation effects in the reconstruction for central momentum settings above approximately 1.1 (GeV/c). One such effect is the field correction, which is a correction to the SOS central momentum setting, and is a parameterization of the zeroth order matrix element for f_4. The SOS field correction is determined from hydrogen elastic coincidence runs, where the actual SOS central momentum can be compared to the value of the central momentum set during the experiment. The deviation observed during πCT is shown in Figure 3-1, together with the observed offset during 2003 [65]. The parameterization used for this correction was

$$\frac{dP}{P}[\%] = -0.036 - 0.00632 \times \exp({P_{SOS}}^{3.004}). \tag{3.3}$$

The saturation correction is another artifact introduced by saturation of the iron cores in the SOS spectrometer. This correction was needed because the optics matrix was used

at central momenta other than the central momentum where the matrix was optimized. This effect was not significant when using the 1740 and 900 matrices because the 1740 matrix was only used for P_{SOS} close to 1.74 (GeV/c), while saturation effects were small in the settings where the 900 matrix was used. Therefore, the saturation correction was only applied to the Default matrix. One can see the effects of this problem in Fig. 3-2. The missing mass minus the mass of the neutron should be zero if events were reconstructed correctly, however, a dependence on x'_{tar} is seen. The first plot in Fig. 3-2 was made without the saturation correction determined during the πCT analysis. The second plot was made using this saturation correction, which was applied in addition to the existing correction.

The SOS saturation correction was applied to the δ matrix elements, and the πCT parameterization is shown in Fig. 3-3. The form of the parameterization is a function of P_{SOS} and x'_{tar}, and is given by

$$\begin{aligned} d(\delta_{\rm SOS})[\%] = \; & 0.0199 - 0.34515x'_{tar} + 12.82(x'_{tar})^2 + 212.492(x'_{tar})^3 \\ & + (-0.01602 - 0.27781x'_{tar} - 14.7455(x'_{tar})^2)\mathrm{P_{SOS}} \\ & + (-174.44\exp(138.856(x'_{tar} - 0.0755)) + 0.1113 + 6.1344x'_{tar}) \\ & \times (1.077 - 1.561\mathrm{P_{SOS}} + 0.3876{\mathrm{P_{SOS}}}^3)\exp(0.4756\mathrm{P_{SOS}}). \end{aligned} \tag{3.4}$$

This parameterization can be seen to become almost zero at $P_{SOS} = 1.4 - 1.5$ (GeV/c), which is where the δ matrix elements of the Default matrix elements were optimized.

3.2 Event selection

The various cuts employed to select e-π^+ coincidence events and the efficiency of these cuts are outlined in this section. Acceptance cuts restricted events to well-understood regions of the spectrometers, and at the same time, were not made too narrow as this affected the statistical uncertainty. The nominal acceptance cuts are given in Table 3.2. The window defined by the acceptance cuts for the quantities $x'_{\rm tar}$ and $y'_{\rm tar}$ were made large enough such that the collimators in each spectrometer defined the acceptance. The positions of these cuts compared to the experimental and Monte Carlo distributions are shown in Figure 3-4. The quantities $x'_{\rm tar}$, $y'_{\rm tar}$ and δ were defined in Section 3.1.

The boundaries of the phase space defined by δ, $y_{\rm tar}$, and $y'_{\rm tar}$ in the SOS disagree with the model of the SOS in some regions (see Section 5.5.3 in Ref. [33]). The acceptance in

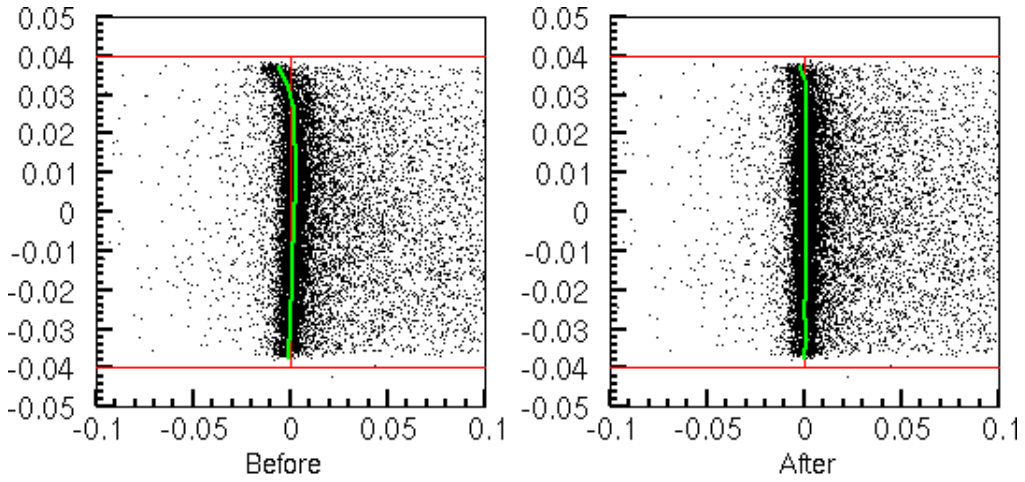

Figure 3-2: SOS saturation correction observed at $P_{SOS} = 1.73$ (GeV/c) using H(e,e$'\pi^+$) and the Default matrix. On the left is x'_{tar} [rad] vs. the missing mass minus the mass of the neutron [MeV/c^2] before applying the πCT saturation correction. The plot on the right is the same distribution after applying the correction.

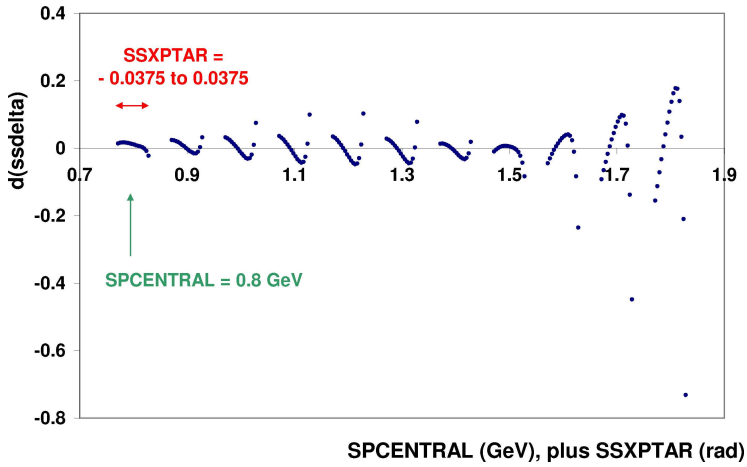

Figure 3-3: SOS saturation correction parameterization determined during the πCT analysis. The quantities ssdelta, ssxptar are the SOS target quantities δ and $x'_{\rm tar}$, respectively, and spcentral is the central momentum setting of the SOS (P_{SOS}).

HMS	SOS
$\lvert x'_{\rm tar}\rvert$ < 0.075 rad	$\lvert x'_{\rm tar}\rvert$ < 0.04 rad
$\lvert y'_{\rm tar}\rvert$ < 0.04 rad	$\lvert y'_{\rm tar}\rvert$ < 0.07 rad
$\lvert\delta\rvert$ < 8 %	-10 % $< \delta <$ 15 %

Table 3.2: Nominal acceptance cuts in the HMS and SOS spectrometers.

the SOS was therefore reduced further using the cuts

$$\begin{aligned} y'_{\rm tar} &> -125.0 + 4.25\delta + 64.0 y_{\rm tar} - 1.7\delta y_{\rm tar}, \text{ and,} \\ y'_{\rm tar} &< \ \ 125.0 - 4.25\delta + 64.0 y_{\rm tar} - 1.7\delta y_{\rm tar}. \end{aligned} \tag{3.5}$$

Particle identification cuts were already discussed briefly in Section 2.4.3. The SOS gas Cerenkov was used to select electrons and the efficiency of this cut, $\varepsilon_{\rm scer}$, was determined using an unbiased sample of electrons that were identified using the SOS calorimeter. Coincidence time cuts and acceptance cuts were also employed to select e-π^+ coincidence events from the unbiased sample so that the efficiency was determined for those events that contributed to the experimental yields. The SOS gas Cerenkov cut and the efficiency of the cut is shown in Table 3.3. The position of the cut was increased to 5 photoelectrons for the December running period as a new SOS gas Cerenkov was installed. The pion rejection ratio was 100:1 during the July running period and 300:1 during the December running period. Even though there is a small chance that a pion may be misidentified as an electron when determining normalized yields, the net effect of events with misidentified pions will be reduced due to the subtraction of random coincidences, and this effect does not pose a problem.

The aerogel and gas Cerenkov detectors in the HMS were used to select π^+ particles. The aerogel Cerenkov detector was used in the data cuts when the central momentum setting of the HMS, $P_{\rm HMS}$, was less than approximately 3.2 (GeV/c). The gas Cerenkov detector was used in the data cuts when $P_{\rm HMS} \gtrsim 3.2$ (GeV/c). The aerogel Cerenkov detector was not used when $P_{\rm HMS} \gtrsim 3.2$ (GeV/c) because the additional particle identification was not required (there was negligible reduction in the random coincidence background) and there would be an additional systematic uncertainty due to the efficiency of the aerogel Cerenkov detector.

An unbiased sample of pion events in the HMS was selected from coincidence events

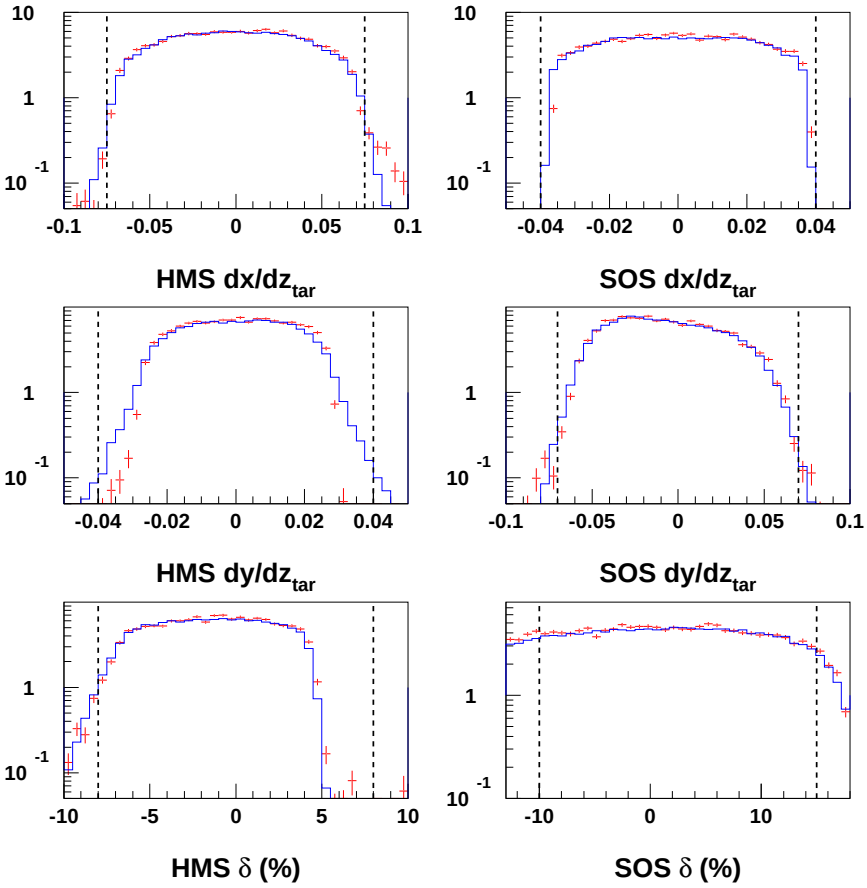

Figure 3-4: Experimental data (crosses) and Monte Carlo simulation (solid line) for H(e,e$'\pi^+$) at $Q^2 = 1.1$ (GeV/c)^2. The Monte Carlo simulation is described in Chapter 4. The quantities $dx/dz_{\rm tar}$ and $dy/dz_{\rm tar}$ are $x'_{\rm tar}$ and $y'_{\rm tar}$, respectively. The dashed lines show the positions of the acceptance cuts.

using tight coincidence time cuts, missing mass cuts and SOS particle identification cuts. The efficiency of the HMS gas Cerenkov, $\varepsilon_{\rm hcer}$, could be determined with an additional cut on the unbiased sample of pions using the HMS aerogel detector to remove protons. The efficiency of the HMS gas Cerenkov detector was then the number of events from the unbiased sample that passed the HMS gas Cerenkov cut divided by the number of events in the unbiased sample.

The HMS gas Cerenkov detector could not be used to remove proton events when determining the efficiency of the HMS aerogel detector, $\varepsilon_{\rm haero}$, as both the pion and proton events were also below the gas Cerenkov threshold. Therefore the unbiased sample of pion

$P_{\rm SOS}$	$N_{\rm scer}$	$\varepsilon_{\rm scer}(\%)$
1.190	1	99.77 ± 0.3
1.730	1	99.81 ± 0.3
1.430	1	99.93 ± 0.3
1.423	5	99.84 ± 0.3
1.034	5	99.83 ± 0.3
0.730*	1	99.16 ± 0.5
0.910*	1	99.69 ± 0.3
1.730†	1	99.81 ± 0.3

Table 3.3: Position of the SOS gas Cerenkov cut and the efficiency of this cut, $\varepsilon_{\rm scer}$. The cut is given by $N_{\rm photoelectrons} > N_{\rm scer}$. Central momentum settings, $P_{\rm SOS}$, labeled with * are the low epsilon points used for L-T separations and the setting labeled with † is the W vs. k_π test point. The uncertainties shown are the normalization uncertainties, the point-to-point uncertainties were estimated using different targets at the same setting and were 0.2%.

events contained a small fraction of proton events due to random coincidences, and $\varepsilon_{\rm haero}$ determined using this sample of events will represent a lower limit of the true $\varepsilon_{\rm haero}$. The accuracy of this method was confirmed by examining the dependence of $\varepsilon_{\rm haero}$ on the target nucleon number, A, and also by performing random coincidence subtraction (Section 3.5) of the sample of pion events before and after applying the aerogel Cerenkov cut.

The position of the HMS aerogel and gas Cerenkov cuts and the associated efficiencies are shown in Table 3.4. The parameterization for the HMS gas Cerenkov efficiency, $\varepsilon(\delta_{\rm HMS})$, that is shown in the table is given by

$$\varepsilon(\delta_{\rm HMS}) = 1.031 - 0.001654\delta_{\rm HMS} - 0.001272(\delta_{\rm HMS} - |\delta_{\rm HMS}|) - 0.3378/(\delta_{\rm HMS} + 10.0) \quad (3.6)$$

This paramameterization of the efficiency was required because the efficiency was observed to depend on $\delta_{\rm HMS}$. This dependence occured because the pions at negative $\delta_{\rm HMS}$ are closer to the momentum threshold of the HMS gas Cerenkov detector compared to those pions at positive $\delta_{\rm HMS}$. A parameterization of the efficiency was not required for the L-T separation kinematic setting at $P_{\rm HMS} = 3.187$ (GeV/c) because the $\delta_{\rm HMS}$ acceptance was predominantly populated at negative $\delta_{\rm HMS}$, and no dependence on this quantity was seen. The efficiencies for both settings as a function of $\delta_{\rm HMS}$ are shown in Figure 3-5. The rejection ratio for the HMS gas Cerenkov was 50:1 at $P_{\rm central} = 3.2$ (GeV/c) and 300:1 at

$P_{\rm HMS}$	$N_{\rm hcer}$	$\varepsilon_{\rm hcer}(\%)$	$N_{\rm haero}$	$\varepsilon_{\rm haero}(\%)$
2.793	-	-	0.7	98.84 $\pm$ 0.5
3.187	0.7	$\varepsilon(\delta_{\rm HMS})$ $\pm$ 0.5	-	-
3.418	1.35	99.11 $\pm$ 0.5	-	-
4.077	2.0	99.77 $\pm$ 0.3	-	-
4.412	2.0	99.77 $\pm$ 0.3	-	-
3.187*	0.7	98.18 $\pm$ 0.5	-	-
3.857*	1.5	99.75 $\pm$ 0.3	-	-
2.074†	-	-	0.7	98.93 $\pm$ 0.5

Table 3.4: The position of the HMS gas Cerenkov cut,$N_{\rm hcer}$ and the efficiency of this cut, $\varepsilon_{\rm hcer}$. The position of the HMS aerogel Cerenkov cut,$N_{\rm hcer}$ and the efficiency of this cut, $\varepsilon_{\rm haero}$ are also shown. The cuts are given by $N_{\rm photoelectrons} > N_{\rm hcer}$ and $N_{\rm photoelectrons} > N_{\rm haero}$ in the gas and aerogel detectors, respectively. Central momentum settings, $P_{\rm HMS}$, labeled with * are the low epsilon points used for L-T separations and the setting labeled with † is the W vs. k_π test point. The uncertainties shown are the normalization uncertainties, the point-to-point uncertainties were estimated using different targets at the same setting and were 0.2%. The parameterization for $\varepsilon(\delta_{\rm HMS})$ is described in the text.

$P_{\rm central}$ = 4.4 (GeV/c). The rejection ratio for the HMS aerogel Cerenkov detector was approximately 5:1 at $P_{\rm central}$ = 2.1 and 2.8 (GeV/c).

The coincidence time was calculated from the time difference between the SOS and HMS triggers, and was used to help identify e-π^+ coincidences. The raw coincidence time is the time of the leading edge of the SOS trigger pulse minus the time of the retimed HMS trigger pulse. The coincidence time is similar to the raw coincidence time except that it includes corrections for the path length of the tracks through the magnetic elements of the spectrometers, pulse height corrections for the signals from the scintillators, and subtraction of the time required for light to travel in the scintillators from the event position to the PMT. The purpose of these corrections was to make the coincidence time a constant value over the acceptance of the spectrometers, assuming an electron was detected in the SOS and a π^+ in the HMS. To allow for the resolution in the timing of the hodoscope scintillators and electronics, a wide (2 ns) cut was applied to the coincidence time. This cut is discussed further in Section 3.5.

Coincidence blocking and synchronization errors can affect good events that would otherwise fall within the coincidence time cuts. These errors affected both random and true events alike, and attempts were made to select cuts that removed events with coincidence

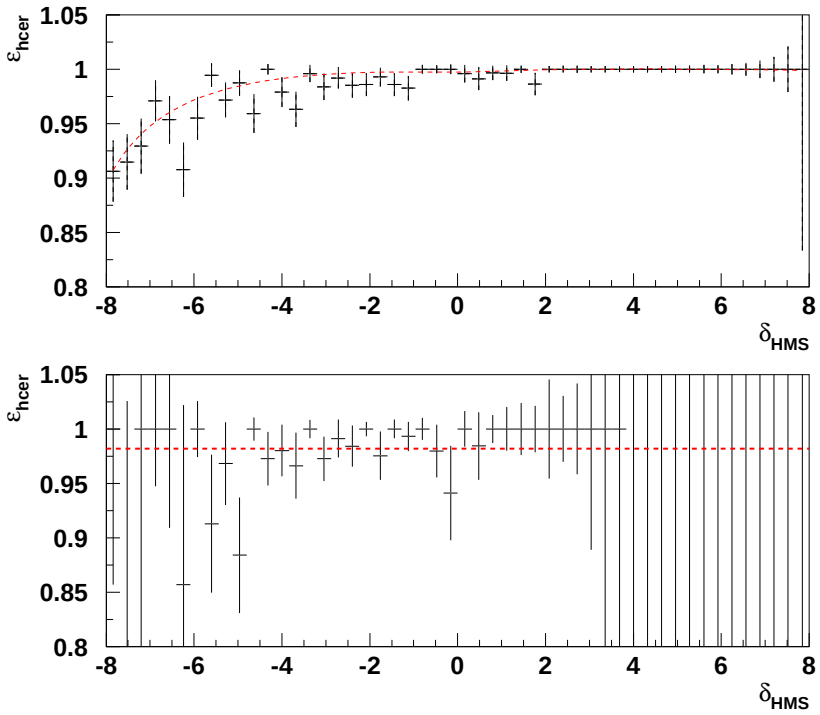

Figure 3-5: HMS gas Cerenkov efficiency for pions at $P_{\rm HMS} = 3.2$ (GeV/c). The experimental efficiencies are the crosses and the dashed lines are the parameterizations that were fit to this data. The first plot shows the parameterization for $\varepsilon(\delta_{\rm HMS})$ and the second shows the efficiency for the L-T separation kinematic setting at $P_{\rm HMS} = 3.187$ (GeV/c).

blocking and synchronization errors. The fraction of events removed by these cuts was used to correct the yields of true coincidence events. A discussion of these errors and the coincidence blocking and synchronization cuts are described in Sections 3.3 and 3.4, respectively.

A background to our quasi-free pion production picture was double pion production. An electron and π^+ may be detected in coincidence with a second pion that is not detected. Two pions may be produced at the vertex and/or by particles interacting with the residual nucleons as they propagate out of the nucleus. These events can not be modeled very well, and so missing mass cuts were used to exclude these events.

The nuclear missing mass, M_x, and nucleon missing mass, M'_x, were defined in Section 1.6. Cuts on either the nuclear missing mass or the nucleon missing mass were employed to exclude events where more than one pion was produced. The nuclear missing mass has a well-defined threshold below which double pion production cannot occur, and is given by $(M_x)_{2\pi} = M_{\pi^0} + M_n + M_{A-1}$. However, this cut was very restrictive and resulted

Q^2 (GeV/c)^2	^{2}H	^{12}C	^{27}Al	^{63}Cu	^{197}Au
1.1	2.00	11.35	25.275	59.35	183.57
2.15	2.04	11.375	25.325	59.40	183.63
3.0	2.025	11.40	25.35	59.40	183.63
3.9	2.04	11.40	25.38	59.45	183.67
4.7	2.08	11.425	25.40	59.50	183.74

Table 3.5: Above-threshold nuclear missing mass cut positions for all kinematic settings and targets. The missing mass cut was $M_x < M_{\rm cut}$, where $M_{\rm cut}$ [GeV/c^2] is displayed in the table.

Q^2 (GeV/c)^2	^{2}H	^{12}C	^{63}Cu	^{197}Au
1.1	1.04	1.04	1.01	1.01
2.15	1.02	1.02	1.01	1.00
3.0	1.03	0.975	0.975	0.95
3.9	1.02	0.95	0.95	0.95
4.7	1.01	0.93	0.93	0.935

Table 3.6: Nucleon missing mass cut positions for all kinematic settings and targets. The missing mass cut was $M'_x < M'_{\rm cut}$, where $M'_{\rm cut}$ [GeV/c^2] is displayed in the table.

in an unacceptable loss of events, particularly at the highest Q^2 setting. Two alternative sets of cuts were used, nucleon missing mass cuts and above-threshold nuclear missing mass cuts. The position of these cuts were determined using a multi-pion simulation discussed in Section 4.8. The positions of the nuclear missing mass cuts are given in Table 3.5 and the positions of the nucleon missing mass cuts are given in Table 3.6.

3.3 Coincidence blocking correction

Coincidence events can be blocked when a random event arrives in one of the spectrometers just before the coincidence event. Not only can the wrong kinematics be assigned to the coincidence event, but the retimed trigger pulse for the spectrometer will have the wrong delay, which affects both the ADCs and TDCs. This effect only becomes significant at high rates and can be made insignificant by suitable prescaling of the single arm triggers.

The coincidence blocking events can be identified in the raw HMS coincidence time, $(T_{\rm raw})_{\rm HMS}$, spectrum, since the blocked events lie outside of the coincidence trigger window and arrive earlier than real coincidence events. The coincidence blocking cut was

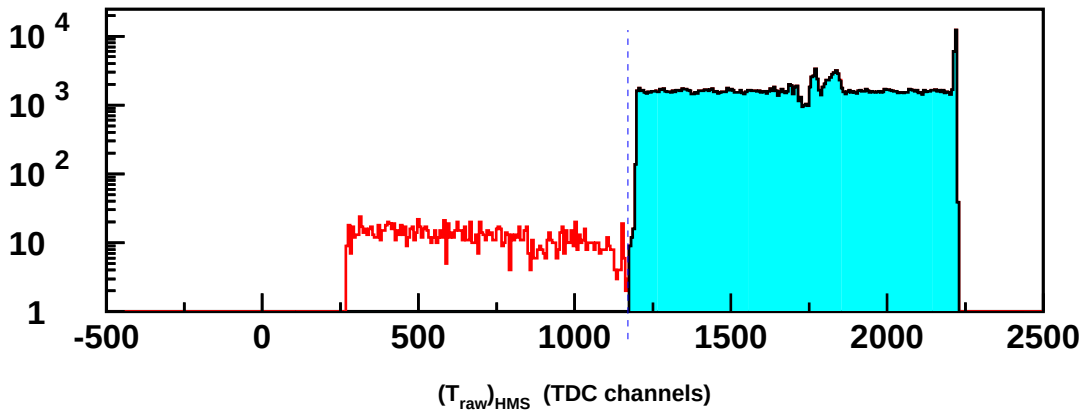

Figure 3-6: Coincidence blocking correction for deuterium at $Q^2 = 1.1$ $(GeV/c)^2$. Events outside of the shaded region arrived earlier than the real coincidence events and constitute 0.62% of the total events.

$(T_{\rm raw})_{\rm HMS} > 1170$, and the coincidence blocking factor, $f_{\rm coinblock}$, was the total events divided by the number that pass this cut. This factor resulted in a correction of less than 0.7% for all runs. The uncertainty due to this correction was estimated using a previously determined parameterization for $f_{\rm coinblock}$ [65], given by

$$1/f_{\rm coinblock} = 1 - R_{\rm SOS}\tau_{\rm SOS}, \tag{3.7}$$

where $R_{\rm SOS}$ was the SOS pretrigger rate (Hz) and $\tau_{\rm SOS} = 92$ ns was an effective gate width. The point-to-point systematic uncertainty, given by the deviation between the experimentally determined correction and the parameterization, was 0.2%.

3.4 Synchronization correction

The ADCs and TDCs can be run in a buffered or unbuffered mode. When operated in the buffered mode, up to 8 events could be stored in the internal buffers of the ADCs and TDCs while the data acquisition computers were busy, which helped reduce the computer dead time during runs with high rates. There was a small probability, however, that the detectors within a spectrometer can be out of synchronization with the detectors of the

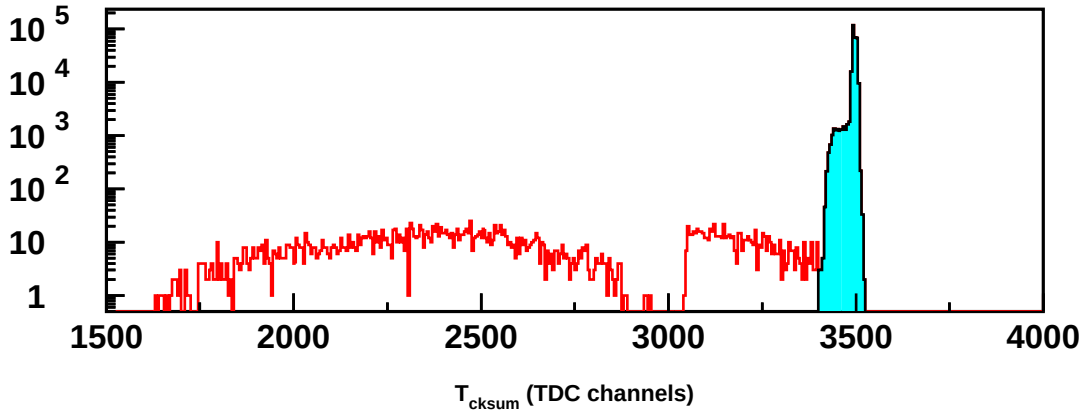

Figure 3-7: Synchronization correction for deuterium at $Q^2 = 1.1$ $(GeV/c)^2$. Events outside of the shaded region have incorrect synchronization and constitute 0.93% of the total events.

other spectrometer when the event is recorded to disk. When this occurs, a particle in a coincidence event could be matched with the preceding or following event in the other spectrometer.

During πCT, the ADCs and TDCs were generally run in the unbuffered mode. Checks were performed using the buffered mode, and there was no observable difference in the normalized yield after correcting for synchronization errors. A correction of less than 1% for loss of synchronization was necessary in the unbuffered mode.

Events where a loss of synchronization occurred could be identified using a checksum, $T_{\rm cksum}$, defined as

$$T_{\rm cksum} \equiv T_{\rm HMS,raw} + T_{\rm SOS,raw}, \tag{3.8}$$

where $T_{\rm HMS,raw}$ is the raw coincidence time measured with an HMS TDC, and $T_{\rm SOS,raw}$ is the raw coincidence time measured with an SOS TDC. The raw coincidence times are given by

$$\begin{aligned} T_{\rm HMS,raw} &= (T_{\rm trig})_{\rm SOS} - (T_{\rm retim})_{\rm HMS}\ , \text{ and,} \\ T_{\rm SOS,raw} &= (T_{\rm trig})_{\rm HMS} - (T_{\rm retim})_{\rm SOS}\ , \end{aligned} \tag{3.9}$$

where $(T_{\rm trig})_{\rm HMS(SOS)}$ is the time of the leading edge of the electronic pulse in the trigger electronics of HMS (SOS), and $(T_{\rm retim})_{\rm HMS(SOS)}$ is the time of the leading edge of the retimed

trigger pulse in the trigger electronics of HMS (SOS). The retiming delay is described in Section 2.4.4. Therefore, the checksum is equal to a constant timing delay

$$\begin{aligned} T_{\text{cksum}} &= (T_{\text{trig}} - T_{\text{retim}})_{\text{HMS}} + (T_{\text{trig}} - T_{\text{retim}})_{\text{SOS}} \\ &= \text{HMS retiming delay} + \text{SOS retiming delay.} \end{aligned} \tag{3.10}$$

Events with a loss of synchronization will not have a constant checksum, and can be identified as those outside of the main peak in Figure 3-7. Coincidence events that passed the coincidence blocking cut (Section 3.3) were used in this figure and in the calculation of the synchronization correction described below. The shaded region represents the region accepted as events with the correct synchronization. The synchronization cut was $T_{\text{cksum}} > 3390$, and the coincidence blocking factor, f_{sync}, was the total events divided by those that pass the synchronization cut.

3.5 Random coincidence subtraction

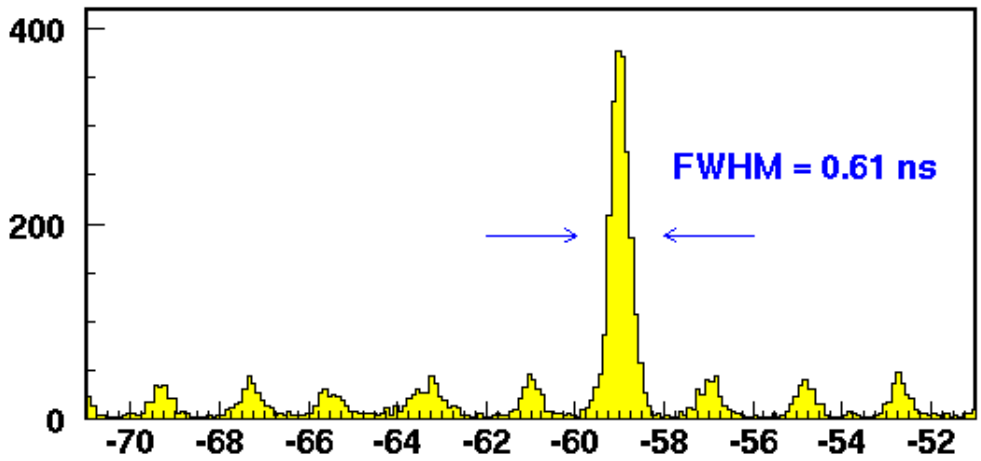

Figure 3-8: Coincidence time (ns) between the scattered electron and π^+. The true coincidence peak has a FWHM of 0.61 ns and the smaller peaks are the random coincidences. The 2 ns coincidence time difference between random coincidence peaks is due to the beam microstructure.

The coincidence time spectrum for the carbon target at $Q^2 = 1.1$ (GeV/c)^2 is displayed in Figure 3-8. The large peak near the coincidence time of -59 ns contains true coincidence events, where an electron and a pion were generated from the same vertex. The absolute

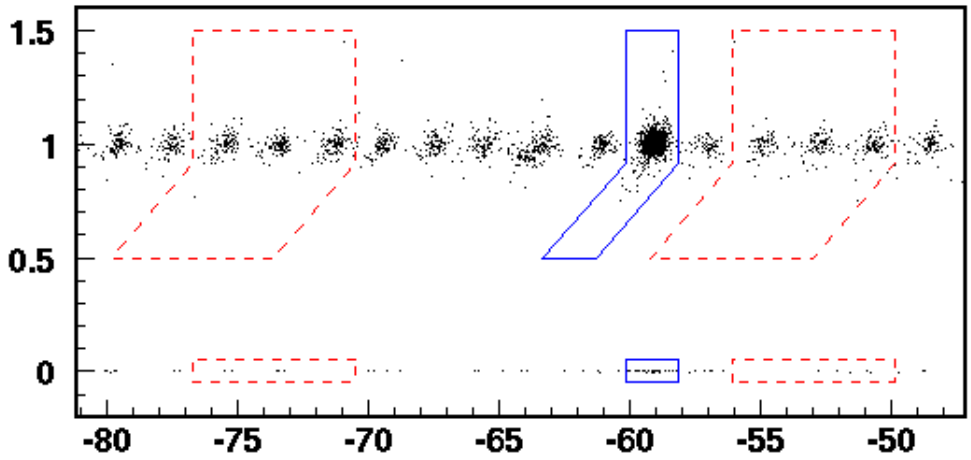

Figure 3-9: Pion velocity (v/c) in the HMS vs. coincidence time (ns). The solid lines show the cut used to select true coincidence events. The dashed lines show the cuts used to select 6 random coincidence peaks. All the cuts described in Section 3.2 were applied to this data.

position of the peak contains arbitrary, fixed delays and so has no physical significance. The smaller peaks contain events where the electron and pion do not originate from the same vertex and are random coincidences. Random coincidences also exist in the true-coincidence peak and can not be separated with coincidence time cuts. These events are removed by background subtraction, which is discussed below.

The coincidence time spectrum shown in Figure 3-8 is from the carbon target at $Q^2 = 1.1$ (GeV/c)^2, which had the worst background from random coincidences compared to the number of events inside the true coincidence peak. Figure 3-9 shows the cuts used to select true coincidence events. The positions of the cuts were fixed relative to large peak, and were adjusted every run. Pions may interact strongly with nuclei in the scintillator material, possibly knocking out a slower hadron, and producing reconstructed events that appear at lower or even zero velocity and with a lower coincidence time. The velocity in the HMS was determined from the time-of-flight between the scintillator planes that are separated by 250 cm (Section 2.4.1). Graphical cuts shown by the solid lines in Figure 3-9 were used to guarantee that all true events were inside the cut. The same analysis with graphical cuts was not necessary in the electron arm (SOS) because electrons do not interact through the strong nuclear force.

The width of the timing cut was equal to the period of the beam microstructure, 2.00 ns,

and is shown in Figure 3-9. The width was large enough so that all true coincidence events could be assumed to be inside the cut. The edges of the cut were 4.3 standard deviations from the center of the coincidence time peak, and so this was a reasonable assumption. There was, however, two corrections for true coincidence events that were excluded by the coincidence time cut, the synchronization correction (Section 3.4) and the coincidence blocking correction (Section 3.3).

The number of true coincidences, $N_{\rm true}$, was obtained through background subtraction. This was accomplished by

$$N_{\rm true} = N_{\rm peak} - \frac{N_{\rm sides}}{6}, \tag{3.11}$$

where $N_{\rm peak}$ was the number of events that passed the cuts represented by the solid lines in Figure 3-9 and $N_{\rm sides}$ was the number of events that passed the cuts represented by the dashed lines. Both $N_{\rm peak}$ and $N_{\rm sides}$ included all the cuts described in Section 3.2. The cuts to select random events near the coincidence time of -75 ns could not be moved closer to the large peak because a coincidence proton peak exists near -66 ns. The proton peak was reduced using cuts on the number of photoelectrons in the HMS gas and/or aerogel Cerenkov detectors, however, this region was avoided in the background subtraction procedure.

Random coincidence subtraction also needed to be applied when comparing a given distribution of experimental data to the Monte Carlo. This was because the distribution of random coincidences (in the missing mass for example) was not the same as the true coincidence distribution. When comparing the experimental distributions to the Monte Carlo, Equation 3.11 was changed to

$$H_{\rm true} = H_{\rm peak} - \frac{H_{\rm sides}}{6}, \tag{3.12}$$

where H is a histogram of a given distribution.

3.6 Scintillator 3-out-of-4 and trigger efficiency

The HMS and SOS spectrometers each contained four layers of scintillators and a requirement for a single-arm trigger was that 3 out of 4 layers must have a hit. The efficiency of this requirement therefore needs to be considered. While individual planes certainly had small regions of inefficiency, it was very likely that at least three planes had hits. The

3-out-of-4 efficiency ($P_{3/4}$) can be calculated from

$$\begin{aligned} P_{3/4} &= P_1P_2P_3P_4 + P_1P_2P_3(1-P_4) + P_1P_2(1-P_3)P_4 \\ &\quad + P_1(1-P_2)P_3P_4 + (1-P_1)P_2P_3P_4 \end{aligned} \tag{3.13}$$

where P_n represents the efficiency of the nth plane. The efficiency of the nth plane could be determined using an unbiased sample, where the unbiased sample was selected by requiring hits in the other three planes. The efficiency was then the fraction of events that had at least one hit in the nth plane divided by the number of events in the unbiased sample.

Correlations can also occur between regions of inefficiency and affect $P_{3/4}$. For example, hodoscope paddles that had underperforming photomultiplier tubes were inefficient near that end of the paddle. If such a region in a paddle was followed by an inefficient region in another plane, then the trigger efficiency had the potential to be lowered in this part of the acceptance. Therefore, the acceptance was divided spatially into a 2-dimensional grid at the focal plane. The 3-out-of-4 efficiency was calculated for each bin using Equation 3.13. The efficiency for each bin was combined into an average using the distribution of e-π coincidence events as a weight. The 3-out-of-4 efficiency was found to be above 99.5% for all runs in both spectrometers. The efficiency was therefore assumed to 100$\pm$0.5%.

For the HMS, $P_{3/4}$ was the trigger efficiency. The SOS trigger was ELREAL, which can be formed from either two hodoscope planes through the STOF condition or three planes through the SCIN condition (Figure 2-8). The efficiency of the hodoscope planes in the SOS trigger was therefore estimated to be $P_{3/4}$, where the uncertainty, 0.5%, is a conservative estimate. The SOS trigger efficiency also depends on the efficiency of the gas Cerenkov and calorimeter. However, a Cerenkov cut is used for all experimental data, and the efficiency of this cut using an unbiased sample was discussed in Section 3.2.

3.7 Dead time corrections

The computer dead time is due to the finite time required for the electronic modules and computers to process an event, which is fixed by the "TS BUSY" signal in Figure 2-9, and this dead time is non-paralyzable [67]. An event that reaches the trigger supervisor will cause the 8LM to suppress all output for subsequent events that occur within a constant time, τ, of the original event.

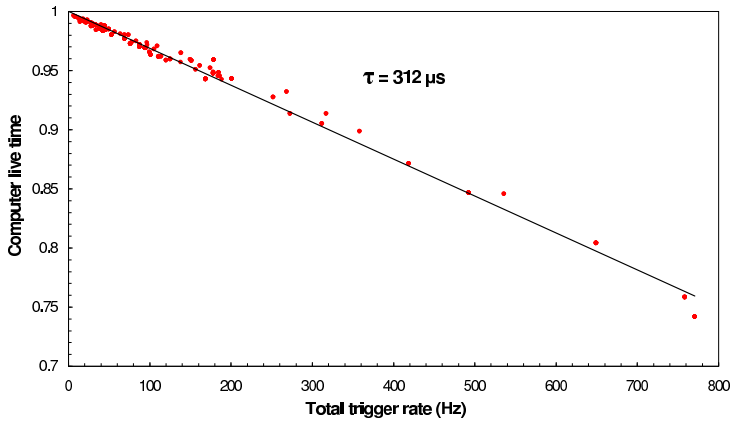

Figure 3-10: The measured computer live time as a function of the rate of any type of trigger (atrig). The solid line is a linear fit to the measured live time.

The computer live time, $\mathrm{LT_{comp}}$, is the ratio of the measured counts to the true number of counts. Using the notation in Figure 2-9, $\mathrm{LT_{comp}}$ is the ratio of the number of triggers to the number of pretriggers, and is given by

$$\mathrm{LT_{comp}} = \frac{N_{\mathrm{trigger}}}{N_{\mathrm{pretrigger}}} = \frac{1}{1 + R\tau}, \tag{3.14}$$

where R is the rate of pretriggers. The computer live time can also be expressed as a function of the rate of triggers, R_{trig}, and is given by

$$\mathrm{LT_{comp}} = 1 - R_{\mathrm{trig}}\tau. \tag{3.15}$$

The measured $\mathrm{LT_{comp}} = N_{\mathrm{trigger}}/N_{\mathrm{pretrigger}}$ is shown in Figure 3-10 as a function of R_{trig}. Although Equation 3.15 provides a reasonable description of the measured $\mathrm{LT_{comp}}$, the measured $\mathrm{LT_{comp}}$ was used to correct the data.

The electronic dead time arises from logic and discriminator modules preceding the 8LM (Figure 2-8). These modules output a digital pulse whenever the input signal(s) to the module satisfy certain conditions and the duration of the digital pulse, the gate width, determines the dead time of the module. Events that are separated in time by less than the longest gate width in the chain of logic units in the trigger may cause that module to ignore the second event or output one elongated digital pulse (rather than two pulses), and

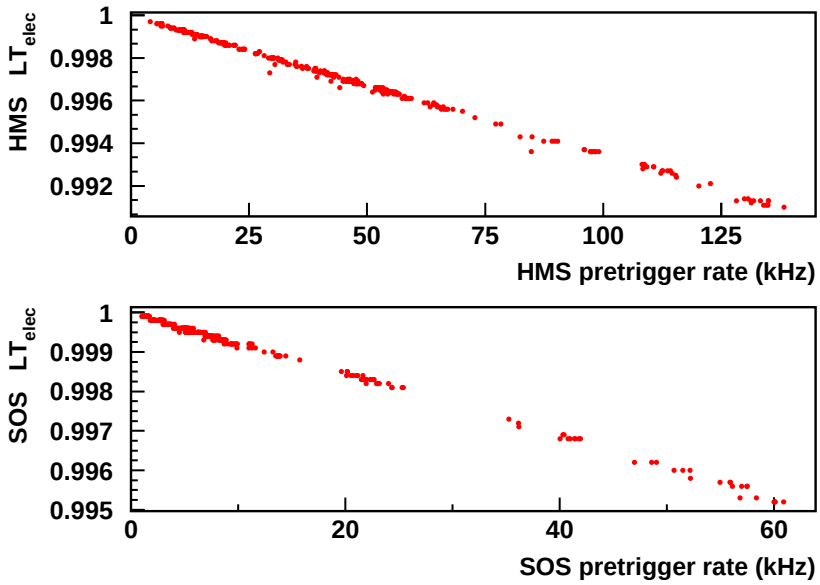

Figure 3-11: The measured electronic live time as a function of the the HMS and SOS pretrigger rate.

the second event will be lost. The limiting gate width, τ_e, is approximately 60 ns, which is very small compared to the average time between events, and therefore the electronic live time, $\mathrm{LT_{elec}}$, can be approximated by

$$\mathrm{LT_{elec}} \approx 1 - R\tau_e. \tag{3.16}$$

The electronic live time was measured using the modules in the upper-right corner in Figure 2-8. These modules had varying gate widths from 40 to 200 ns, and allows one to extrapolate to zero gate width and the number of true events, N_{true}. The electronic live time, given by

$$\mathrm{LT_{elec}} = N_{\mathrm{pretrigger}}/N_{\mathrm{true}}, \tag{3.17}$$

was calculated for all runs, and is shown in Figure 3-11. The experimental yields (Section 3.10) were corrected for the electronic dead time using the correction factors

$$(f_{\mathrm{elec}})_{\mathrm{HMS,SOS}} = 1/(\mathrm{LT_{elec}})_{\mathrm{HMS,SOS}}. \tag{3.18}$$

The uncertainty due to the dead time corrections were dominated by the computer dead time, as the size of this correction was as large as 25%, whereas the correction due to the electronic dead time was less than 1%. The uncertainty in the dead time corrections was estimated from data runs taken at constant beam current, but varying computer dead time. A point-to-point uncertainty of 0.5% was assumed in the dead time corrections based on the observed variation in the dead time corrections with the trigger and pretrigger rates.

3.8 Tracking efficiency

The tracking efficiency, ε_{track}, is the probability of finding a track from experimental signals from the wire chambers when a charged particle passes through them. As it is not always clear if a particle did or did not pass through the wire chambers in a given event, the determination of the tracking efficiency can be a subjective process. Typically ε_{track} is determined by selecting a pool of events where one is convinced that a charged particle passed through the wire chambers, and ε_{track} is the number of events where a track was found divided by the number of events in the pool. The tracking efficiency depends on the reconstruction software and the efficiency of the individual wires in the wire chambers.

The tracking efficiency depends on the event rate, which affects the probability of seeing two tracks inside the $\sim$250 ns width of the TDC window. The reconstruction code only returns a single track during such events, and the reduction in the event rate is corrected for by the dead-time correction (Section 3.7). However, events with multiple tracks have a greater chance of being reconstructed incorrectly and the πCT analysis includes the correction worked out during the analysis of the Pion Form Factor Experiment [65]. They found a bias in the reconstruction software due to the exclusion of two-track events. The tracking efficiency is also different for electrons, pions and protons, and so identification (PID) cuts are used to select electrons in the SOS (gas Cerenkov and calorimeter) and pions in the HMS (gas and aerogel Cerenkov).

Events where the track should have passed through the wire chambers were selected by requiring hits on particular TOF paddles that define a fiducial area in the wire chambers. Events that hit the central paddle in each of the four scintillator planes in a given spectrometer and produced at least a small signal in the calorimeter ($E_{cal} > 0.02 \times P_{central}$) were guaranteed by geometry constraints to pass through the wire chambers, and should have a

track. The PID cuts described above were applied to this sample of events and ε_{track} was the probability that the reconstruction code found tracks in this sample.

The tracking efficiency was improved by a new track selection method called the "Prune" method. A tolerance time of 3 ns was used in both the HMS and SOS. The tolerance time was a cut on scintillator times projected to the focal plane that excluded PMT signals that were very different in time from the other PMT signals in the calculation of the coincidence time and ε_{track}. Furthermore, if there were a number of possible tracks in a given event, the Prune method excluded tracks with unreasonable reconstructed quantities (x'_{tar}, y'_{tar}, δ, etc.) and tracks that did not point toward the scintillators that were hit. More information on the Prune method can be found in Refs. [68, 69].

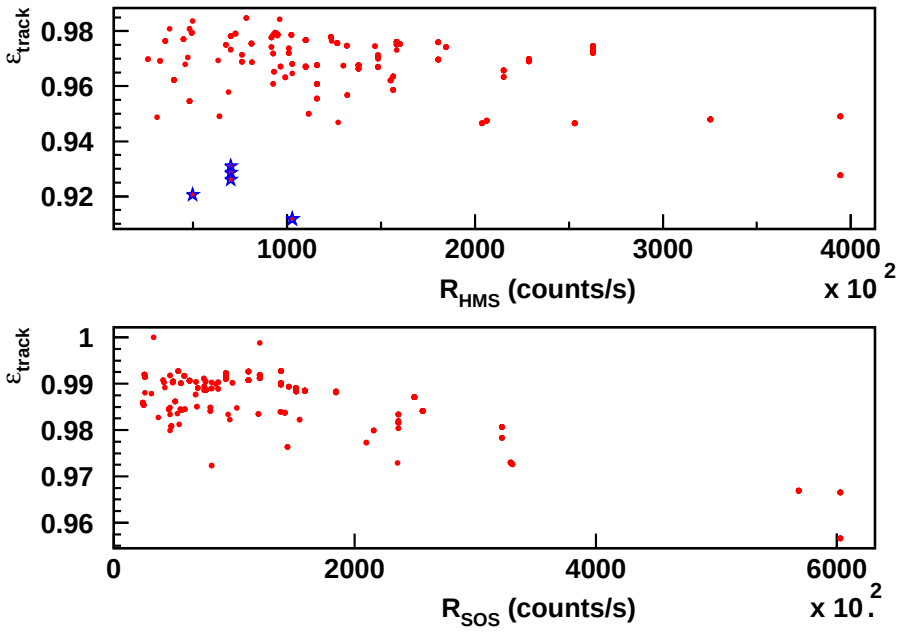

Figure 3-12: Tracking efficiency, ε_{track}, vs. the normalized scaler of the scintillator plane closest to the wire chambers, R. The tracking efficiencies of the HMS (top) and the SOS (bottom) are shown.

The tracking efficiencies in the HMS and SOS are shown in Figure 3-12. The efficiency was averaged over 5-10 runs at a time, unless conditions, targets, and/or kinematics changed. The average efficiency of each group of 5-10 runs was assigned to all runs in the group. Runs that had trips were excluded from the average but were assigned the average efficiency of

its group.

There were several hours during the December running period when the low outside air temperature affected the mixing of the wire chamber gas and the HMS tracking efficiency was reduced. These runs are marked with a star in Figure 3-12. These settings were repeated after the hardware was operating normally and it was found that the normalized yield, which included corrections for the tracking efficiency, was unaffected.

The tracking efficiency was 92-99% in the HMS and 96-100% in the SOS. Based on the variation of ε_{track} with R in Figure 3-12, a point-to-point uncertainty of 1.0% and 0.5% was assigned to the correction for the HMS and SOS tracking efficiency, respectively. A normalization uncertainty of 1.0% and 0.5% was assigned to the HMS and SOS tracking efficiency, respectively, due to the size of the correction and an estimate of how well one can select a pool of events where a charged particle passed through the wire chambers.

3.9 Particle absorption in the spectrometers

When hadrons are detected in either the HMS or SOS, particles may interact though the strong nuclear force with nuclei in the target material, the window of the scattering chamber, the windows of the spectrometer, etc. The transmission, T_h, through these materials was calculated using the hadron-nucleus inelastic cross section and applied as a correction to the normalized yield (Section 3.10).

Proton absorption was corrected for in the analysis of elastic H(e,e′p) data (Sec. 4.9), and it was weakly dependent on the proton momentum. Measurements in Ref. [65, 31] indicate that the transmission of protons in the HMS was 94.5% under spectrometer configurations similar to what was used during πCT. The transmission was largely unchanged from earlier transmission analyses, see for example Ref. [70]. The proton transmission was measured by selecting electron cuts that guaranteed the proton was within the spectrometer acceptance and the transmission was the measured coincidence rate divided by the electron single-arm rate.

The transmission for pions is weakly dependent on the pion momentum between 2.1 and 4.4 (GeV/c). Based on the work in Ref. [65], the transmission for pions in the HMS was 95%. The transmission was expected to change slightly between targets due to the absorption in half of the thickness of the target material. Theoretically, the average absorption will

change at most by 0.5% between the targets. The pion absorption correction will cancel when we form the ratio between targets and in the L/T separation, but it was applied to calculations of the absolute cross section. The uncertainty due to the pion absorption was 2% in the absolute cross section determination, which was estimated using the difference between the calculated pion transmission and the measured proton transmission [65]. The point-to-point uncertainty assigned to the pion transmission was 0.5%.

3.10 Charge-normalized yield

The charge-normalized yield, $\bar{Y}$, which is often called the normalized yield, is given by

$$\bar{Y} = Y/Q, \tag{3.19}$$

where Y is the yield of a given run in counts and Q is the charge delivered by the beam in mC. The charge delivered by the beam was measured using the beam current from BCM2 (Section 2.2) integrated over time for the duration of the run. The yield is given by

$$Y = \frac{N_{\rm true}}{[\varepsilon_{\rm scer}\varepsilon_{\rm track}/f_{\rm elec}]_{\rm SOS}\,[\varepsilon_{\rm hcer}\varepsilon_{\rm haero}\varepsilon_{\rm track}/f_{\rm elec}]_{\rm HMS}}\frac{N_{\rm pretrigger}}{N_{\rm trigger}}f_{\rm coinblock}f_{\rm sync}\frac{1}{T_h}. \tag{3.20}$$

A small modification to this equation was required when the π^+ was below the HMS gas Cerenkov threshold and a cut on this detector was not used. For these runs, $\varepsilon_{\rm hcer}$ was set to one. The correction factors, $(f_{\rm elec})_{\rm HMS}$, $(f_{\rm elec})_{\rm SOS}$, $f_{\rm coinblock}$, and $f_{\rm sync}$ were all within 1% of unity for all runs. The coincidence prescale factor was set to 1 during e-π data taking, and therefore the yields did not require a correction for prescaling.

3.11 Target boiling check

The effects of localized boiling in the liquid targets due to the beam was checked using a series of runs with varying beam current. This series of runs is called a luminosity scan and the the beam current was varied between 15 μA and 90 μA. Luminosity scans were made using the hydrogen and deuterium liquid targets and the carbon target. The results from the luminosity scans are shown in Figure 3-13, and there was no observable change in boiling in either the hydrogen or deuterium targets over the range of currents used in the

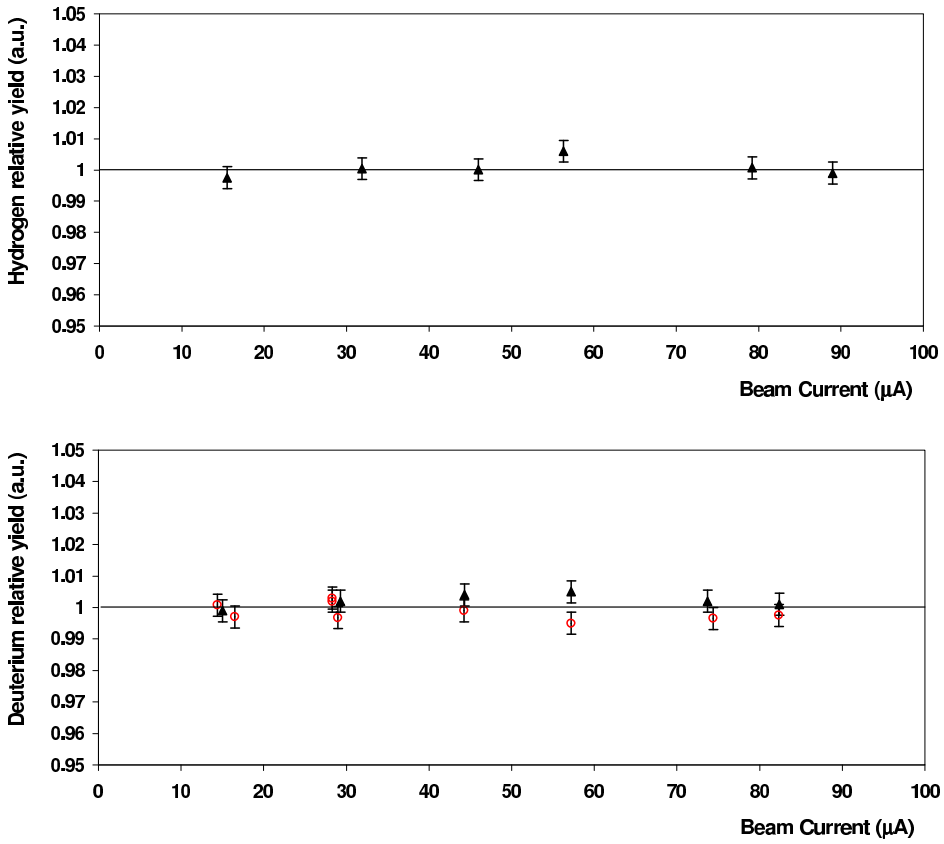

Figure 3-13: Target boiling check of the liquid targets. The luminosity scan was repeated for deuterium; the solid triangles are the first scan and the open circles are the second scan. Only the statistical uncertainty is shown and the relative yield is described in the text.

luminosity scans. More details on the luminosity scans can be found in Ref. [71]. Therefore, no correction was necessary in the luminosity due to target boiling with an uncertainty of 0.6%.

The relative yield in Figure 3-13 is the normalized yield from the liquid target divided by the normalized yield from the carbon target and multiplied by an arbitrary scale factor.

3.12 Cell wall subtraction for liquid targets

The liquid hydrogen and deuterium targets were enclosed by aluminum walls, and events from beam interactions with the cell walls were subtracted from the liquid target yields.

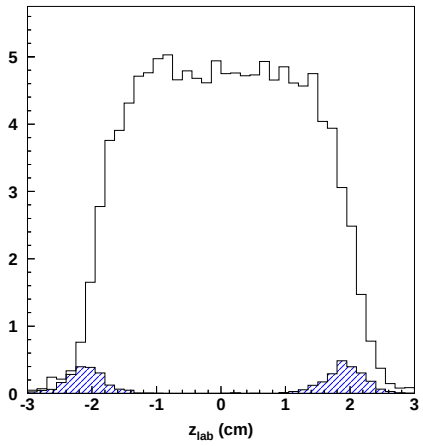

Figure 3-14: Histogram of the position of the experimental interaction point for the liquid hydrogen target at $Q^2 = 1.1$ $(\mathrm{GeV/c})^2$. $\mathrm{z_{lab}}$ is the distance along the direction of the beam from the center of the target to the reconstructed interaction point. The shaded histogram comes from the aluminum cell walls and the unshaded histogram from the liquid hydrogen. The dummy target was used to determine the shaded histogram, and dummy target subtraction was performed to remove the contribution of the cell walls from the unshaded histogram.

Aluminum 'dummy' target data were taken whenever these targets were used. This target, labeled "Al, foil 1" and "Al, foil 2" in Table 2.2, consisted of two aluminum foils located at the same position and had the same separation as the aluminum walls of the liquid targets. The dummy target foils were approximately 7 times thicker than the walls of liquid targets to increase the event rate. The measured thickness ratios were 7.088, 7.711 and 7.757 for loop 1, loop 2 and loop 3, respectively, where the loop numbers are described in Section 2.3. The relative contribution of the cell walls to the yields from the liquid hydrogen is shown in Figure 3-14.

The dummy target data were analyzed with the same cuts used to analyze the liquid targets. Furthermore, the position of some cuts change (for example the missing mass cuts used to exclude double pion production) when using a hydrogen target compared to using a deuterium target. The dummy target data were therefore analyzed a number of times, with each set of cuts, for proper target cell wall subtraction. The dummy target was our only aluminum target, and so this data were analyzed again with missing mass cuts suitable for aluminum to provide the aluminum normalized yields.

Dummy target subtraction was performed using the normalized yields measured using

the liquid and dummy target. The dummy target subtracted normalized yield, $\bar{Y}_{\mathrm{L}}$ is given by

$$\bar{Y}_{\mathrm{L}} = \bar{Y}_{\mathrm{L+W}} - \frac{1}{r_{\mathrm{dummy}}}\bar{Y}_{\mathrm{dummy}}, \tag{3.21}$$

where $\bar{Y}_{\mathrm{L+W}}$ is the normalized yield from the liquid and wall, r_{dummy} is the ratio of the dummy target foil thickness to the thickness of the cell wall, and $\bar{Y}_{\mathrm{dummy}}$ is the normalized yield from the dummy target. Distributions from liquid targets that were properly normalized, so that the sum of the events in the distribution was the normalized yield, $\bar{H}_{\mathrm{liquid}}$, were corrected for the contributions from the cell walls by

$$\bar{H}_{\mathrm{L}} = \bar{H}_{\mathrm{L+W}} - \frac{1}{r_{\mathrm{dummy}}}\bar{H}_{\mathrm{dummy}}. \tag{3.22}$$

The contribution of the cell wall to the liquid target yields was less than 5%. The uncertainty in r_{dummy} was 2%, and so the contribution to the uncertainty was at most 0.1%.

Chapter 4

Simulation of the experiment

The standard Monte Carlo simulation code for Hall C, called SIMC, was used to simulate the experimental data taken during πCT. As the solid angles of the spectrometers were much smaller than 4π, events were generated in only the phase space marginally larger than the acceptance of the spectrometers. The generation window was made larger than the acceptance to allow for offsets, radiation and energy loss that may scatter events into the acceptance. The pion electroproduction cross section was included as a weight that was applied to the simulated particles.

After events were generated at the vertex, they were transported through the spectrometer optics using COSY matrix elements. The COSY matrix elements were determined from a COSY INFINITY [72] model of the spectrometers. Particles were transported into the detector huts and thrown away if they passed outside of the active region of the detectors. The properties of the particles that survived this requirement were recorded in the output files.

Corrections were applied to the particles after they were generated at the vertex. These corrections included pion decay, multiple scattering, energy loss, Coulomb corrections, final state interactions, Pauli blocking and radiative corrections. The Monte Carlo equivalent yield was formed and the cuts that were applied to the experimental data were applied to the Monte Carlo events. The Monte Carlo was used to extract the bin-centered experimental cross section by iterating the model cross section until the Monte Carlo distributions matched the data. Then the experimental cross section was determined by evaluating the model cross section at the desired point within the acceptance.

4.1 Pion decay, multiple scattering and energy loss

Pion decay, multiple scattering and energy loss are standard features in SIMC, and can be turned on and off using flags in the input files. Descriptions of corrections for these processes can be found in Ref. [31] and a short description is given below. The materials traversed by the particles in each spectrometer are listed in Tables 4.1 and 4.2.

Pions (π^+) may decay in flight before they are detected in the HMS detector hut and the main decay mode is into a μ^+ and a ν_μ. Generally, the pion momentum was greater than 2 GeV/c, and so the lifetime of the pion in the lab frame was at least 0.37 μs. The time required to travel from the target to the HMS hut was $\sim$0.083 μs and, at the lowest pion momentum setting, 20% of the pions were expected to decay in flight.

Pion events could not be separated experimentally from muon events, and so pions that did decay could still produce a valid trigger and fall inside of the experimental acceptance. Therefore, the path of the pion was divided into steps (the distances between apertures in the HMS Monte Carlo), and the decay of the pion was simulated at each step. If the pion decayed in a given step, then the muon kinematics were generated (the muon was produced mostly at forward angles) and the muon was transported through the spectrometer. As the central momentum of the HMS was not changed between target changes, the pion decay correction will be the same and cancel in the ratio of yields from heavy targets to that of the hydrogen target. This assumption is also true for the L-T separation analysis, where the HMS central momentum settings are not very different between the high and low ϵ settings. The systematic uncertainty due to pion decay comes from events where the pion decayed inside either a quadrupole or a dipole in the HMS. These events are not modeled very well because the COSY matrix elements for a given magnet describe the transport of a particle with a single momentum. From the Monte Carlo simulation, 2.5% (1.4%) of events at the lowest (highest) Q^2 setting involved the pion decaying inside of a magnet, and the difference between targets was at most $\pm$0.1%. Therefore, a point-to-point uncertainty of 0.1% and an overall normalization uncertainty of 1.0% was assigned to this correction.

Electrons and hadrons may interact with the electrons that make up the material that they traverse and undergo multiple scattering. After passing through a certain material, a new scattering angle was generated using a parameterization fitted to the theory

Absorber	Material	thickness (cm)	density (g/cm^3)	X_0 (g/cm^2)	(X/X_0) (%)
Target Chamber Window	Al	0.013	2.70	24.01	0.292
Targets	LH2	4.0	0.0723	61.28	0.468
	LD2	4.0	0.165	122.6	0.538
	Al Dummy	0.195	2.70	24.01	2.19
	Carbon	0.294	2.27	42.66	1.56
	Copper	0.089	8.96	12.86	6.20
	Gold	0.0196	19.32	6.46	5.86
Chamber Window	Al	0.0406	2.70	24.01	0.457
Chamber HMS Gap	Air	15	0.00121	36.66	0.050
HMS Entrance Window	Kevlar	0.0381	0.74	55.20	0.0511
	Mylar	0.0127	1.39	39.95	0.0443
HMS Exit Window	Titanium	0.0508	4.54	16.2	1.42
Dipole-DC Gap	Air	35	0.00121	36.66	0.1155
HMS DC Windows	Mylar	4(0.0025)	1.39	39.95	0.0178
HMS DC Gas	Ar/C_6H_6	12(1.8)	0.00154	27.38	0.121
HMS DC sense wires	W	12(5.89E-06)	19.30	6.76	0.020
HMS DC field wires	Be/Cu	36(0.00018)	5.40	38.88	0.090
Aerogel entrance	Al	0.15	2.70	24.01	1.687
Aerogel	SiO_2	9.0	0.071	44.054	1.45
Aerogel air gap	Air	16.0	0.00121	36.66	0.0528
Aerogel exit	Al	0.1	2.70	24.01	1.1245
HMS S1X	polystyrene	1.067	1.03	43.80	2.51
HMS S1Y	polystyrene	1.067	1.03	43.80	2.51
HMS Cer Windows	Al	2(0.102)	2.70	24.01	2.28
HMS Cer gas (0.956 atm)	C_4F_{10}	135	0.00972	34.72	3.78
HMS Cer gas (0.350 atm)	C_4F_{10}	135	0.00356	34.72	1.38
HMS Cer mirror support	Rohacell	1.8	0.05	40.88	0.220
Air gap DC-S2X	Air	83.87	0.00121	36.66	0.272
HMS S2X	polystyrene	1.067	1.03	43.80	2.51
HMS S2Y	polystyrene	1.067	1.03	43.80	2.51

Table 4.1: Layer material and thicknesses traversed by particles exiting the target cell detected in the HMS (Modified from Ref. [65]).

Absorber	Material	thickness (cm)	density (g/cm^3)	X_0 (g/cm^2)	(X/X_0) (%)
Chamber Window	Al	0.0406	2.70	24.01	0.456
Chamber SOS Gap	Air	15	0.00121	36.66	0.050
SOS Entrance Window	Kevlar	0.0127	0.74	55.20	0.0170
	Mylar	0.0076	1.39	39.95	0.0260
SOS Exit Window	Kevlar	0.0381	0.74	55.20	0.051
	Mylar	0.0127	1.39	39.95	0.044
Dipole-DC Gap	Air	15	0.00121	36.66	0.050
SOS DC Windows	Mylar	14(0.0127)	1.39	39.95	0.062
SOS DC Gas	Ar/C_6H_6	12(0.617)	0.00154	27.38	0.044
SOS DC sense wires	W	12(35.4E-06)	19.30	6.76	0.121
SOS DC field wires	Be/Cu	36(0.00018)	5.40	38.88	0.09
SOS S1X	polystyrene	1.040	1.03	43.80	2.44
SOS S1Y	polystyrene	1.098	1.03	43.80	2.58
*SOS Cer Windows	Al	2(0.05)	2.70	24.01	1.12
*SOS Cer gas (1 atm)	Freon-12	111	0.00510	24.53	2.152
*SOS Cer mirror support	Rohacell	1.8	0.05	40.88	0.22
†SOS Cer Windows	Al	2(0.0762)	2.70	24.01	0.0171
†SOS Cer gas (1.41 atm)	C_4F_{10}	99.4	0.0143	34.72	4.09
†SOS Cer mirror support	Mylar	0.113	1.39	39.95	0.393
Air gap DC-S2Y	Air	174	0.00121	36.66	0.574
SOS S2X	polystyrene	1.040	1.03	43.80	2.44
SOS S2Y	polystyrene	1.098	1.03	43.80	2.58

Table 4.2: Layer material and thicknesses traversed by particles detected in the SOS (Modified from Ref. [65]). Layers marked with a (*) were used during the July running period, and those marked with a (†) were used during the December running period.

of Molière [42]. The scattering angle was generated with a width described by

$$\theta_{\rm rms} = \frac{13.6}{\beta p}\sqrt{t} \times (1 + 0.038 \log_{10} t), \tag{4.1}$$

where t is the thickness of the material in radiation lengths, β is the particle speed and p is the particle momentum in MeV/c.

Electrons and hadrons lose energy through the ionization of atoms within the materials that they traverse. The most probable energy loss for a relativistic particle traversing a thin layer of material is given by the Bethe-Bloch equation

$$E_{prob} = K\frac{Zt}{A\beta^2}\left[\ln\frac{m_e}{I^2} + 2\ln\frac{P}{M} + \ln\frac{KZt}{A\beta^2} - \delta - U + 1.06\right], \tag{4.2}$$

where $K = 0.15354$ cm^2/g, t is the material thickness in g/cm^2, M, P and β are the mass, momentum and speed of the incident particle, respectively, Z and A are the atomic number and nucleon number of the material, I is the mean ionization energy of the material, δ is the density effect correction, and U is the shell correction term. The energy loss assigned to the particle was generated according to a Landau distribution with the most probable value equal to E_{prob}.

4.2 Coulomb corrections

Coulomb corrections to the incoming and scattered electron were applied according to the Effective Momentum Approximation (EMA) approach in Ref. [73]. No Coulomb corrections were applied to nuclei with a single proton (hydrogen and deuterium), because this effect was already included in the elementary pion cross section. Coulomb distortions are due to the exchange of virtual photons with the remaining $(Z-1)$ protons in the nucleus.

The change in energy when an electron moves from infinity to a position, $\vec{r}$, inside a nucleus with $(Z-1)$ protons is

$$\Delta E(\vec{r}) = f_C(|\vec{r}|)\left[\alpha\frac{(Z-1)}{R_0}\right], \tag{4.3}$$

where, $R_0 = [1.1A^{1/3} + 0.86A^{-1/3}]$ fm is the radius of the nucleus, α is the fine structure constant, and $\vec{r} = 0$ is the center of the nucleus. If the electron moved to the surface of

the nucleus, then $f_C = 1$, and at the center of the nucleus, $f_C = 1.5$. The EMA picture in Ref. [73] uses an average potential

$$\bar{V} \sim (0.75 - 0.8) \times \frac{3}{2}\left[\alpha\frac{(Z-1)}{R_0}\right], \tag{4.4}$$

which corresponds to $f_C \approx 1.163$ in Equation 4.3.

Assuming that there is no deflection of the incoming electron, with momentum $\vec{k}_i$, the momentum at the vertex, $(\vec{k}_i)_v$, is

$$(\vec{k}_i)_v = \vec{k}_i(1 + \Delta E/k_i), \tag{4.5}$$

which is called the eikonal approximation. The increased beam momentum is used in SIMC in the calculation of the three momentum transfer, $(\vec{q})_v = (\vec{k}_i)_v - (\vec{k}_f)_v$. The outgoing electron has a generated vertex momentum, $(\vec{k}_f)_v$, and is weighted by the cross section calculated using $(\vec{q})_v$. The vertex momentum of the outgoing electron was then reduced due to Coulomb effects to produce the momentum of the outgoing electron, $\vec{k}_f$, according to

$$\vec{k}_f = (\vec{k}_f)_v(1 - \Delta E/(k_f)_v). \tag{4.6}$$

This method is equivalent to using the effective momentum transfer, $\vec{q}^{\,\mathrm{eff}}$. In this picture, $\vec{q}^{\,\mathrm{eff}}$, is equivalent to what was defined as $(\vec{q})_v$, above. The effective momentum transfer can be calculated from the incoming and outgoing electron momentum after Coulomb distortions have been applied, and is given by

$$\begin{aligned}
\vec{q}^{\,\mathrm{eff}} &= (\vec{k}_i)_v - (\vec{k}_f)_v \\
&= \vec{q}_{\mathrm{meas}} + \hat{k}_i\Delta E - \hat{k}_f\Delta E \\
&= \vec{q}_{\mathrm{meas}} + \tfrac{\vec{q}_{\mathrm{meas}}}{k_f}\Delta E + (\tfrac{\vec{k}_i}{k_i} - \tfrac{\vec{k}_i}{k_f})\Delta E \\
&= \vec{q}_{\mathrm{meas}}(1 + f_C\tfrac{\alpha(Z-1)}{R_0}\tfrac{1}{k_f}) + f_C\tfrac{\alpha(Z-1)}{R_0}\tfrac{\vec{k}_i}{k_i}(1 - \tfrac{k_i}{k_f}),
\end{aligned} \tag{4.7}$$

where, $\vec{q}_{\mathrm{meas}} = \vec{k}_i - \vec{k}_f$.

The incident and scattered electron plane waves are distorted due to the Coulomb field leading to focusing of these waves in the nucleus and an enhancement in the cross section. In the EMA prescription, the incident and scattered electron waves can be approximated

by

$$\psi_{\mathbf{k}_{i,f}}(\mathbf{r}) = \frac{|(\mathbf{k}_{i,f})_v|}{|\mathbf{k}_{i,f}|}\exp(i\mathbf{k}_{i,f}.\mathbf{r}) = \left(1 + f_C\frac{\alpha(Z-1)}{R_0}\frac{1}{|\mathbf{k}_{i,f}|}\right)\exp(i\mathbf{k}_{i,f}.\mathbf{r}), \tag{4.8}$$

producing an enhancement in the cross section given by the focusing factor, F, with

$$F = (|\mathbf{k}_i||\mathbf{k}_f|)_v^2/(|\mathbf{k}_i||\mathbf{k}_f|)^2. \tag{4.9}$$

The enhancement due to the focusing of the scattered wave exactly cancels with the enhanced phase space factor that appears in the cross section

$$(d\boldsymbol{k}_f)_v = \frac{|(\mathbf{k}_f)_v|^2}{|\mathbf{k}_f|^2}d\boldsymbol{k}_f. \tag{4.10}$$

The net enhancement in the cross section is given by

$$\sigma = \left(1 + f_C\frac{\alpha(Z-1)}{R_0}\frac{1}{|\mathbf{k}_i|}\right)^2(\sigma)_v. \tag{4.11}$$

This version of the EMA approximation has been verified to be a good approximation, compared to exact numerical calculations, when the energy of the final state electron is above 200 MeV and Q^2 is larger than about 0.09 $(\mathrm{GeV/c})^2$ [74]. The Coulomb corrections to the equivalent Monte Carlo normalized yields for copper and gold, and the uncertainty in this correction, are shown in Table 4.3.

E_{beam} (GeV)	$E_{e'}$ (GeV)	$(dY/Y)_{\mathrm{copper}}$ (%)	$(dY/Y)_{\mathrm{gold}}$ (%)
4.021	1.190	0.22 ± 0.05	0.87 ± 0.22
5.012	1.730	-1.08 ± 0.27	-1.57 ± 0.39
5.012	1.430	-1.24 ± 0.31	-3.49 ± 0.87
5.767	1.423	-1.78 ± 0.45	-3.27 ± 0.82
5.767	1.034	-2.17 ± 0.54	-4.36 ± 1.09

Table 4.3: Coulomb corrections to the equivalent Monte Carlo normalized yield. The change in the equivalent Monte Carlo normalized yield ((dY/Y)) is shown for copper and gold targets. Positive (dY/Y) indicates that Coulomb corrections increase the yield. The uncertainties shown are point-to-point uncertainties, and were assumed to be 25% of the correction.

Coulomb corrections can be applied to the pion produced in A(e,e$'\pi^+$) by increasing the pion energy by $\bar{V}$, where $\bar{V}$ was defined in Equation 4.4. These corrections probably should not be used when the model for energy for the proton is given by the default model. This

is because E_m from the spectral function is the separation energy for the proton, which already contains Coulomb effects for the hadron. However, these corrections were applied when $E_m = 0$ and proton-on-shell models for the energy of the proton were used.

4.3 Final-state interactions

In the quasifree model of the reaction A(e,e$'\pi^+$), the pion is produced from a proton in the nucleus, which produced a recoiling neutron, and the other nucleons are spectators. Final-State Interactions (FSI) of the outgoing neutron with the spectator nucleons can affect the quasifree cross section, and are called n-N FSI. The effects of n-N FSI are strongest when the relative momentum between the recoil neutron and the spectator nucleon(s) is small, which corresponds to nuclear missing masses near the single-pion production threshold (see below). Therefore, n-N FSI is likely the cause of the disagreement between the experimental and Monte Carlo distributions shown in Figure 4-1.

The Jost function prescription for n-N FSI is described in Refs. [31, 75]. This approach assumes that the phase shifts from n-N scattering can be applied to the phase of the recoiling neutron wave function, leading to an enhancement of the neutron wave function at the point where it was produced. It also assumes that the transition matrix element for pion production factorizes into the matrix element for elementary pion production and the secondary interaction due to n-N FSI. Although the Jost function was not used to correct the Monte Carlo in πCT, the Jost function method that was tested with our data will be summarized below.

The electroproduction cross section is modified by the Jost function, $J(k_{\rm rel})$, according to

$$\sigma_\pi^{\rm NN\ FSI} = \left[1 + \delta \times \left(\frac{1}{|J(k_{\rm rel})|^2} - 1\right)\right] \sigma_\pi, \tag{4.12}$$

where δ is a free parameter that is adjusted until there is reasonable agreement between the Monte Carlo and experimental missing mass distributions. The quantity, $k_{\rm rel}$, is the relative momentum between the recoil neutron and a spectator nucleon in their center-of-mass frame, and is given by

$$k_{\rm rel}^2 = -2M_n^2 + (M_x^2 - M_n^2 - M_{A-1}^2)/(A-1), \tag{4.13}$$

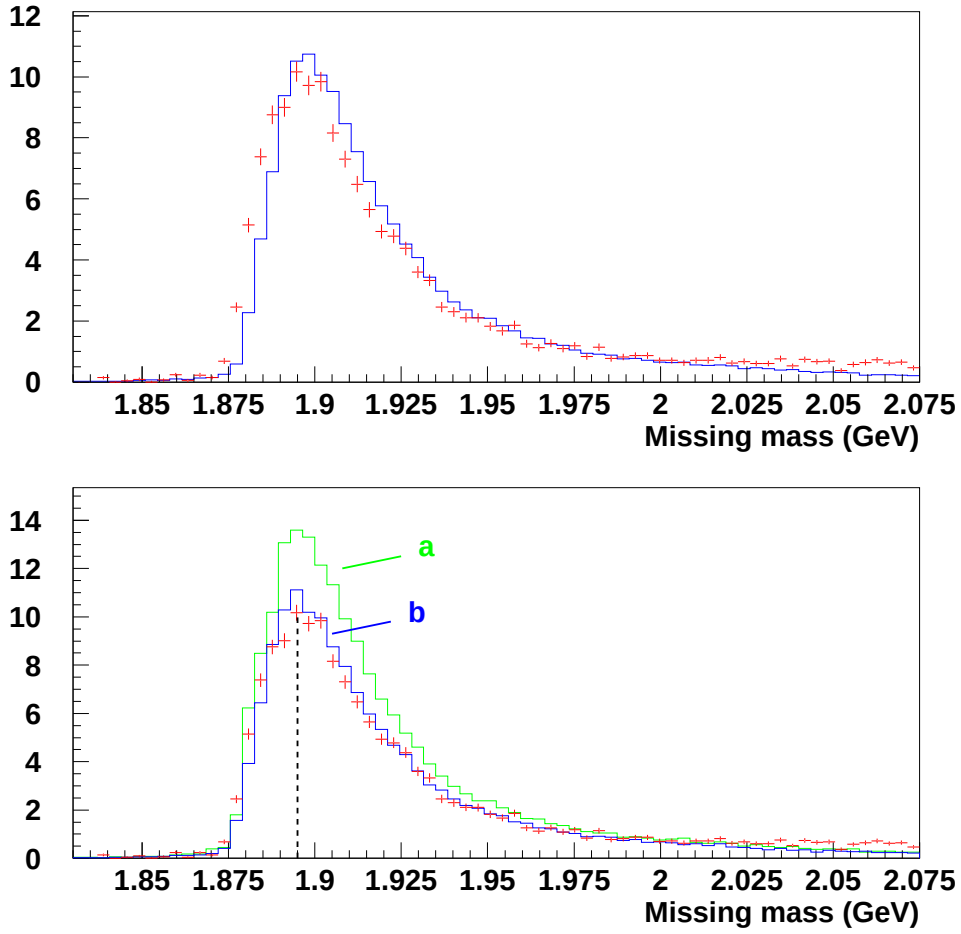

Figure 4-1: The histograms in the top plot are missing mass distributions for D(e,e′π^+) at $Q^2 = 1.1$ (GeV/c)^2. The experimental data are the crosses and the Monte Carlo with the default model for the energy of the proton (Section 1.9) and without corrections for n-N FSI are the lines. The bottom plot contains the same experimental data (crosses) and histogram (a) is the Monte Carlo distribution for the default model with the Jost function correction for n-N FSI with $\delta = 0.5$. Histogram (b) is the Monte Carlo distribution using the $E_m = 0$ model without the Jost function correction. No arbitrary normalizations have been applied. The vertical, dashed line is at $M_x = 2M_n$.

where M_n is the mass of the neutron, A is the nucleon number of the target nucleus, and, M_x is the nuclear missing mass. For A=2, this simplifies to

$$k_{\rm rel}^2 = M_x^2 - 4M_n^2. \tag{4.14}$$

The Jost function can be written,

$$J(k_{\rm rel}) = \frac{k_{\rm rel} - i\beta}{k_{\rm rel} - i\alpha}, \tag{4.15}$$

where $\alpha = 172.099$ MeV/c and $\beta = -7.9391$ MeV/c. Events with small M_x will therefore have small $k_{\rm rel}$ and the enhancement in $\sigma_\pi^{\rm NN\ FSI}$ is very large in this region as $J(0)^{-2} = 470$.

This method has been used in previous experiments that used ^{3}He and ^{2}H targets [31, 65] to give better agreement between the experimental and Monte Carlo missing mass distributions. However, the effect of the Jost function on the Monte Carlo normalization was not important for these experiments. In πCT, the quantity $\bar{Y}_{\rm exp}/\bar{Y}_{\rm SIMC}$ for nuclear targets is important and this quantity is affected by changes in the Monte Carlo normalization. The increase in $\bar{Y}_{\rm SIMC}$ was as large as 25% in deuterium with the Jost function approach, and was obviously too large when compared to the experimental data. The enhancement in the Monte Carlo yield was very sensitive to the choice of the free parameter, δ, leading to a large uncertainty in this method. There was also no reliable way to extend this approach to carbon and heavier nuclei.

It was found in this analysis that the Monte Carlo missing mass distributions had much better agreement with the experimental data when the $E_m = 0$ model (Section 1.9) was used. This is shown in Figure 4-1. Therefore, in the πCT analysis, no corrections using the Jost function were applied and the $E_m = 0$ model was used. It is worthwhile to note that n-N FSI predominantly affected the lowest Q^2 setting in πCT and the Jost function approach for correcting for n-N FSI, if it were used, would increase the slope of the nuclear transparency with Q^2. More results using the $E_m = 0$ model and other models for the energy of the proton will follow in Chapter 5.

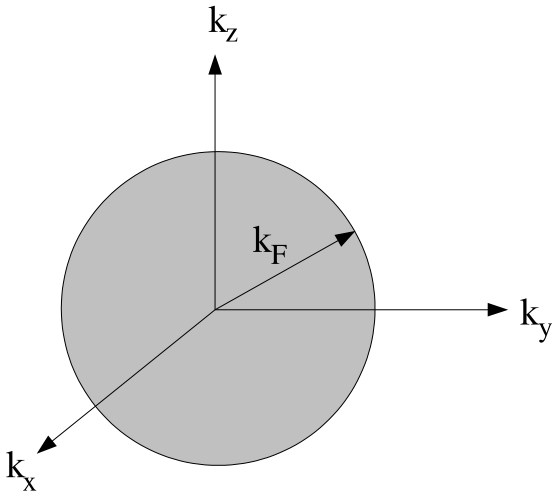

Figure 4-2: Ideal Fermi Gas model of a nucleus. The nucleons occupy all momentum states within a sphere of radius k_F.

4.4 Pauli blocking

In the Ideal Fermi Gas model, the nucleons occupy all single particle states with momentum, $|\mathbf{k}|$, less than the Fermi momentum, k_F. The nucleons fill a sphere in momentum space with a radius equal to k_F, which is shown in Figure 4-2. The Fermi momentum of infinite nuclear matter is 260±10 MeV/c. The values of the Fermi momentum for the nuclei used in πCT are shown in Table 4.4, which were determined using the values of similar nuclei in Refs. [76, 77].

Nuclide	k_F (MeV/c)	k'_F (MeV/c)
^{2}H	55	
^{12}C	228	221
^{27}Al	236	260
^{63}Cu	241	265
^{197}Au	245	265

Table 4.4: Fermi momentum, k_F and k'_F, of the target nuclei used in πCT. k_F was determined from similar nuclei in Ref. [76] and k'_F from similar nuclei in Ref. [77].

The π^+ particle detected in the HMS was produced from a proton in nuclear targets. This produced a recoiling neutron which was forbidden to occupy any single particle state that already contained a neutron. In the Ideal Fermi Gas model this is equivalent to the requirement that the recoiling neutron momentum, $|\mathbf{k}_n|$, is greater than k_F.

An alternative model to the Ideal Fermi Gas model includes interactions between the

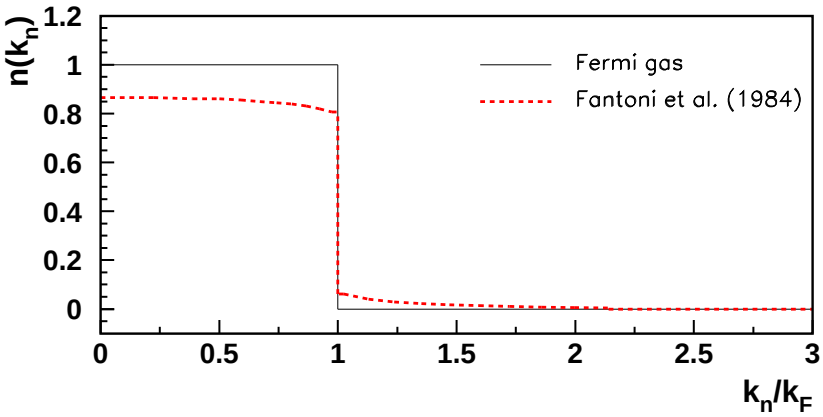

Figure 4-3: The distribution function, $n(|\mathbf{k}_n|)$, of nucleons in nuclear matter.

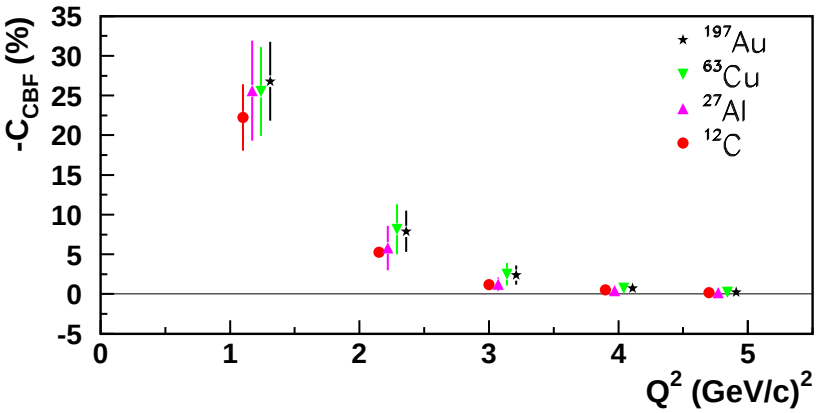

Figure 4-4: Pauli blocking correction to the Monte Carlo equivalent yield using the CBF theory of Fantoni and Pandharipande [78]. The correction, C_{CBF}, is equal to $(\bar{Y}_{pb} - \bar{Y})/\bar{Y}$, where $\bar{Y}_{pb}$ ($\bar{Y}$) is calculated from a simulation with (without) Pauli blocking. Different targets have been offset in Q^2 for clarity.

nucleons that can induce correlations. These correlations deplete single particle states below the Fermi momentum and populate single particle states above the Fermi momentum. Fantoni and Pandharipande [78] calculated the distribution function using perturbation theory in a correlated basis. The distribution function is shown in Figure 4-3, together with the distribution function from the Ideal Fermi Gas model.

Pauli blocking was applied in the Monte Carlo as a weight factor. Each event was assigned the weight $1-n(|\mathbf{k}_n|)$, where $|\mathbf{k}_n|$ could be calculated from the generated quantities using 4-momentum conservation. The effect of Pauli blocking was to decrease the Monte Carlo equivalent yield (Section 4.7), and the relative changes in the yields are shown in Figure 4-4. The correction, C_{CBF}, was determined using the distribution function calculated by Fantoni and Pandharipande [78] and using the unprimed Fermi momentum values in

Table 4.4. The uncertainty in the Pauli blocking model, represented by the error bars in Figure 4-4, were estimated using the primed Fermi momentum values in Table 4.4 and the distribution function from the Ideal Fermi Gas model. The uncertainty was equal to the largest deviations in the correction due to Pauli blocking with these changes.

4.5 Radiative corrections

The standard Hall C Monte Carlo includes radiative corrections based on the formalism derived by Mo and Tsai [79], but modified for use in coincidence experiments. The model for pion electroproduction was built from the procedure used in (e,e′p) experiments, and two options exist. The first is to treat the initial hadron, which is a proton bound inside the nucleus, as a virtual pion and the second is to treat the outgoing pion as an off-shell proton.

The extended peaking approximation was used, where the photons were emitted only in the direction of the incoming electron, outgoing electron, or outgoing pion. Furthermore, the total radiated strength was preserved by splitting the non-peaked part of the angular distribution between the incoming and outgoing electrons. The soft photon approximation was used where the radiated photon energies were restricted to be much less than the energies of the particles. Feynman diagrams for processes that contribute to radiative corrections in the Monte Carlo are shown in Figure 4-5.

Radiative corrections affected both the cross section and momentum of the incoming and outgoing charged particles. The first order pion electroproduction cross section was modified by a multiplicative radiative weight factor, $R_{\rm corr}$, given by

$$R_{\rm corr} = (1 - \delta_{\rm hard}) R_{\rm soft} \Phi_e^{\rm ext} \Phi_{e'}^{\rm ext}, \tag{4.16}$$

where, $R_{\rm soft}$ represents the soft contributions (the first four diagrams in Fig. 4-5), and $(1 - \delta_{\rm hard})$ the internal, hard contributions (the last two diagrams in Fig. 4-5). Contributions from IR divergences in the soft contributions that are eliminated by the hard processes were not included in either $R_{\rm soft}$ or $(1 - \delta_{\rm hard})$. The soft correction factor, $R_{\rm soft}$, included both internal and external soft corrections. External radiative corrections are due to Bremsstrahlung from the interactions of incoming and outgoing electrons with nu-

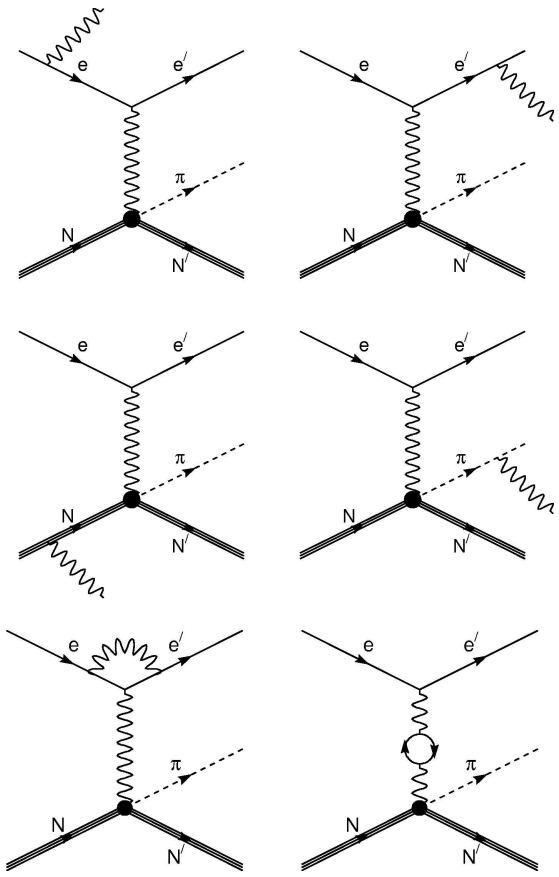

Figure 4-5: Feynman diagrams of processes contributing to radiative corrections in the Monte Carlo. Figure from Ref. [31].

clei other than the one involved in the scattering process. The factors $\Phi_e^{\rm ext}$ and $\Phi_{e'}^{\rm ext}$ in Equation 4.16 corrected for hard external radiative processes.

The radiative tails in the experiment and Monte Carlo are shown in Figure 4-6. The experimental events at low E_m in H(e,e′p) are due to resolution effects and the events in the radiative tail have good agreement. For H(e,e′π^+), the Monte Carlo radiative tail is slightly below the experimental data and this is discussed further in the next section.

The Monte Carlo was tested with the off-shell radiation option. There was no observable change in the missing mass or other distributions and the Monte Carlo equivalent yield changed by at most 0.5%. The largest source of uncertainty in the radiative correction procedure comes from radiation due to the pion as the electron radiation is relatively well known. The Monte Carlo equivalent yields changed by 2-4% when radiation from the pion was turned off (2% was for the settings with low Q^2 and 4% was for the heavy targets at

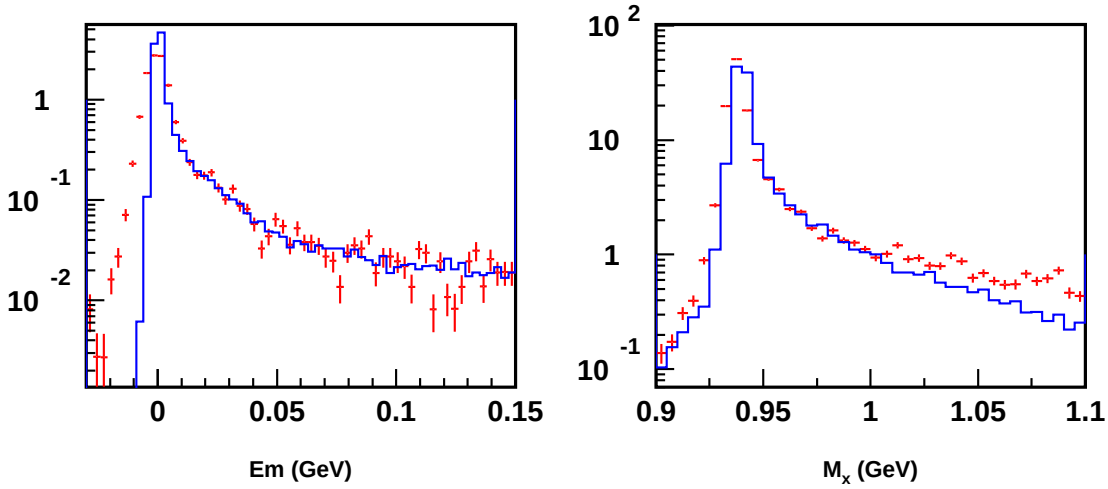

Figure 4-6: On the left is the missing energy, E_m, distribution for H(e,e′p) at $Q^2 = 6.1$ (GeV/c)^2, and on the right is the missing mass, M_x, distribution for H(e,e′π^+) at $Q^2 = 1.1$ (GeV/c)^2. Experimental data are the red crosses and the Monte Carlo are the solid lines. No arbitrary normalization factors have been applied. Collimator punch-through (Section 4.6) was turned off in the Monte Carlo and events where the pion struck the collimator were stopped.

high Q^2). The point-to-point uncertainty in the radiative corrections was estimated from the target dependence of the Monte Carlo equivalent yield when the pion radiation was turned off. This was 1% at the low Q^2 and 2% at high Q^2. The normalization uncertainty was assumed to be 2%.

4.6 Collimator punch-through

The HMS collimator consisted of 2.5 inch thick Heavymet (Tungsten with 10% CuNi) and was designed to remove particles that would otherwise hit magnetic elements and/or fall outside of the phase space that could be accurately modeled with the Monte Carlo. The collimator is very effective at stopping electrons, however, hadrons could pass through the material and still contribute to the experimental yield. Pions were detected in the HMS and the effect of pions punching through the HMS collimator was simulated in the Monte Carlo.

The pions were transported through the collimator material in small (3 mm) steps where they could undergo multiple scattering and energy loss using the same algorithms as

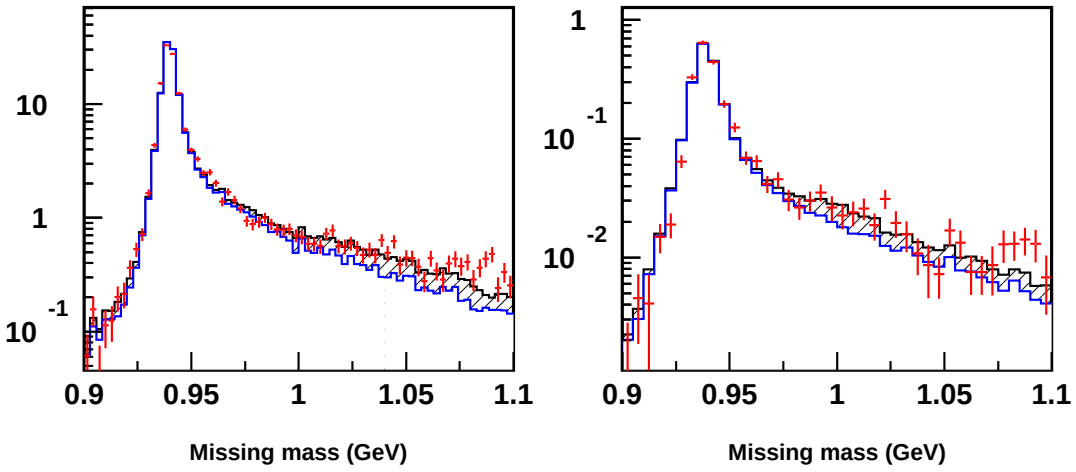

Figure 4-7: Missing mass distributions for H(e,e′π^+) at $Q^2 = 1.1$ (GeV/c)^2 (left) and $Q^2 = 4.8$ (GeV/c)^2 (right). The experimental data (red crosses) are shown with Monte Carlo simulations that do not include collimator punch-through events (blue solid line). The shaded area shows the effect of including pions that pass through the HMS collimator in the Monte Carlo.

described in Section 4.1. Pions that passed through the collimator typically lost 125 MeV in energy. The transmission of pions through the collimator was also reduced due to hadronic interactions with nuclei in the collimator material. The transmission was 53-56% for all momentum settings in πCT.

The calculation of the pion transmission through materials is described in Section 3.8 of Ref. [65], where the choice of the pion-nucleus cross section was chosen carefully using the total, elastic, reaction, inelastic and absorption cross sections. The total pion-nucleus cross section encompasses all hadronic interactions, $\sigma_{\rm total} = \sigma_{\rm elastic} + \sigma_{\rm reaction}$. The reaction cross section includes channels where the pion is absorbed (no pions in the final state) or undergoes an inelastic interaction, $\sigma_{\rm reaction} = \sigma_{\rm absorption} + \sigma_{\rm inelastic}$. Elastic scattering is peaked at small angles and pions that undergo this type of interaction with nuclei were still expected to produce a valid trigger. It is also possible that pions undergo an inelastic hadronic interaction and produce a valid trigger. Therefore, the cross section that was used to estimate the transmission of pions in the collimator was the average of the total and absorption cross sections.

The effect of simulating events that punch through the HMS collimator is shown in Figure 4-7. These events were sizable in the long tail of the missing mass distribution. The

contribution of collimator punch-through events to the total Monte Carlo yield was 3-4% with little variation (±0.5%) between targets and kinematic settings. Therefore, a point-to-point systematic uncertainty of 0.5% is assumed due to the collimator punch through events. To determine the systematic uncertainty for absolute cross sections, the Monte Carlo code was run using σ_{total} in place of the average of the total and absorption cross sections in the calculation of the pion transmission. It was found that the yields decreased by 1.3% at all settings within the previously stated point-to-point uncertainty. Therefore, the normalization uncertainty due to events that punch through the HMS collimator was assumed to be 1%.

4.7 Monte Carlo equivalent yield

The Monte Carlo equivalent yield was formed using the number of events inside the acceptance of the detectors. The corrections described above (pion decay, Coulomb corrections, etc.) were included to make the simulation as close to the conditions in the experiment as possible. The Monte Carlo particles were weighted by the cross section multiplied by the luminosity, where the luminosity, $\mathcal{L}$, was given by

$$\mathcal{L} = \frac{Q_{\text{SIMC}}}{e}\frac{tN_A}{M}, \tag{4.17}$$

where Q_{SIMC} was the simulated cumulative charge delivered by the beam, t was the target thickness in g/cm^2, N_A was Avagadro's number and M was the target mass in amu. The Monte Carlo equivalent yield, Y_{SIMC}, was the sum of the weights, w, of events,

$$Y_{\text{SIMC}} = \sum_i w_i = \sum_i \mathcal{L}\sigma_i = \mathcal{L}\sum_i \sigma_i, \tag{4.18}$$

where i represents the i'th event that passed the same acceptance cuts that were applied to the experimental data (Section 3.2). The normalized Monte Carlo equivalent yield, $\bar{Y}_{\text{SIMC}}$, was given by

$$\bar{Y}_{\text{SIMC}} = \frac{Y_{\text{SIMC}}}{Q_{\text{SIMC}}} \tag{4.19}$$

4.8 Multiple-pion production simulation

A multiple-pion production simulation was developed for deuterium and heavier targets for the πCT analysis. An outline of the multiple-pion simulation was given in Section 1.13.4. It was assumed that the mechanism for multiple-pion production was quasifree single-pion production from a nucleon followed by a second process that was incoherent from the first, where the pion produces one or more pions from a different nucleon. This process is shown in Figure 4-8. Furthermore, the cross section for the second process was assumed to be uniform over the acceptance of the HMS spectrometer.

The result from the standard Monte Carlo code was modified after the vertex quantities had been generated in the quasifree model and before the pion was transported through the materials in the target and HMS spectrometer. The N'' nucleon in Figure 4-8 was given a random momentum using the spectral function. The pion that was detected outside of the nucleus was generated uniformly over the HMS acceptance. The missing mass, M_m, was calculated using the 4-momenta of the pion from the quasifree process (the first black circle), the N'' nucleon and the pion detected outside of the nucleus. The event was discarded if M_m was less than $M_N + M_\pi$, which corresponds to the threshold for multiple-pion production, and/or the energy of the pion that was detected was greater than the initial energy involved in the second interaction.

The single-pion and multiple-pion simulations are compared to the experimental data from the carbon target in Figure 4-9 and the copper target in Figure 4-10. The threshold for double-pion production for electroproduction on a nucleus of mass M_A is $M_x = M_{A-1} + M_\pi$. Ideally, we would like to place the double-pion M_x cut several MeV below this threshold to guarantee that there is no contamination from double-pion events in our data samples. However, this type of cut causes an unacceptable loss of statistics at the two highest Q^2 settings. The multiple-pion simulation shows that it is safe to increase the double-pion missing mass cut above this threshold with minimal contamination. The double-pion missing mass cut was placed at the position where there was not more than 0.4% contamination in the Monte Carlo equivalent yield and the point-to-point systematic uncertainty was assumed to be 0.4%. A surprising result was seen in the ratio of the multiple-pion production yield over the single-pion yield. The ratio changed between targets but was almost constant at all Q^2 settings for the same type of target. This is shown in Table 4.5.

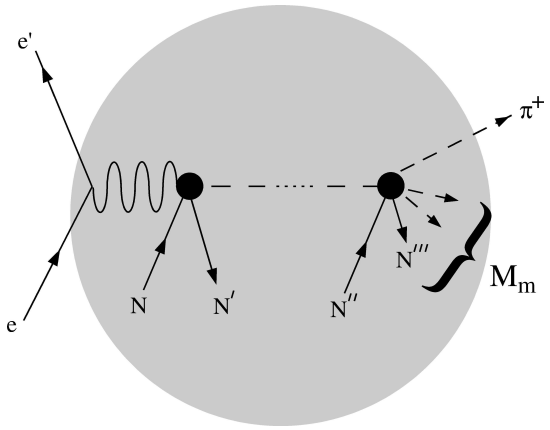

Figure 4-8: The diagram corresponding to multiple-pion production in the model developed for πCT. The interaction represented by the first black circle is described by the quasifree model. The missing mass, M_m, is the invariant mass of the the N''' nucleon and other particles produced in the interaction represented by the second black circle. The π^+ particle is detected outside of the nucleus.

Q^2 (GeV/c)^2	^{2}H	^{12}C	^{27}Al	^{63}Cu	^{197}Au
1.1	0.07	0.14	0.25	0.21	0.24
2.15	0.10	0.18	0.26	0.23	0.36
3.0	0.07	0.20	0.21	0.18	0.33
3.9	0.12	0.16	-	0.18	0.30
4.7	0.09	0.17	-	0.11	0.21

Table 4.5: Yields for multiple-pion production divided by single-pion production. This ratio was determined by fitting the single-pion and multiple-pion Monte Carlo results to the data. Two settings with the ^{27}Al target are marked with a "-" as there were few experimental events at these settings.

The background due to ρ production and $\rho \rightarrow \pi\pi^+$ was simulated. The ρ was produced isotropically in the γ^*-N center of mass frame and the kinematics that were generated were transformed into the lab frame. The ρ decay was simulated and the π^+ produced from the decay was transported through the target material. Most π^+ particles were outside of the acceptance of the HMS spectrometer and were discarded. Those π^+ particles that were inside of the acceptance were simulated inside the HMS spectrometer using the same methods used in the single-pion production simulation. The nuclear missing mass threshold for ρ production was greater than the threshold in the multiple-pion simulation, and therefore, the ρ production simulation was not used to determine the position of the multiple-pion missing mass cut.

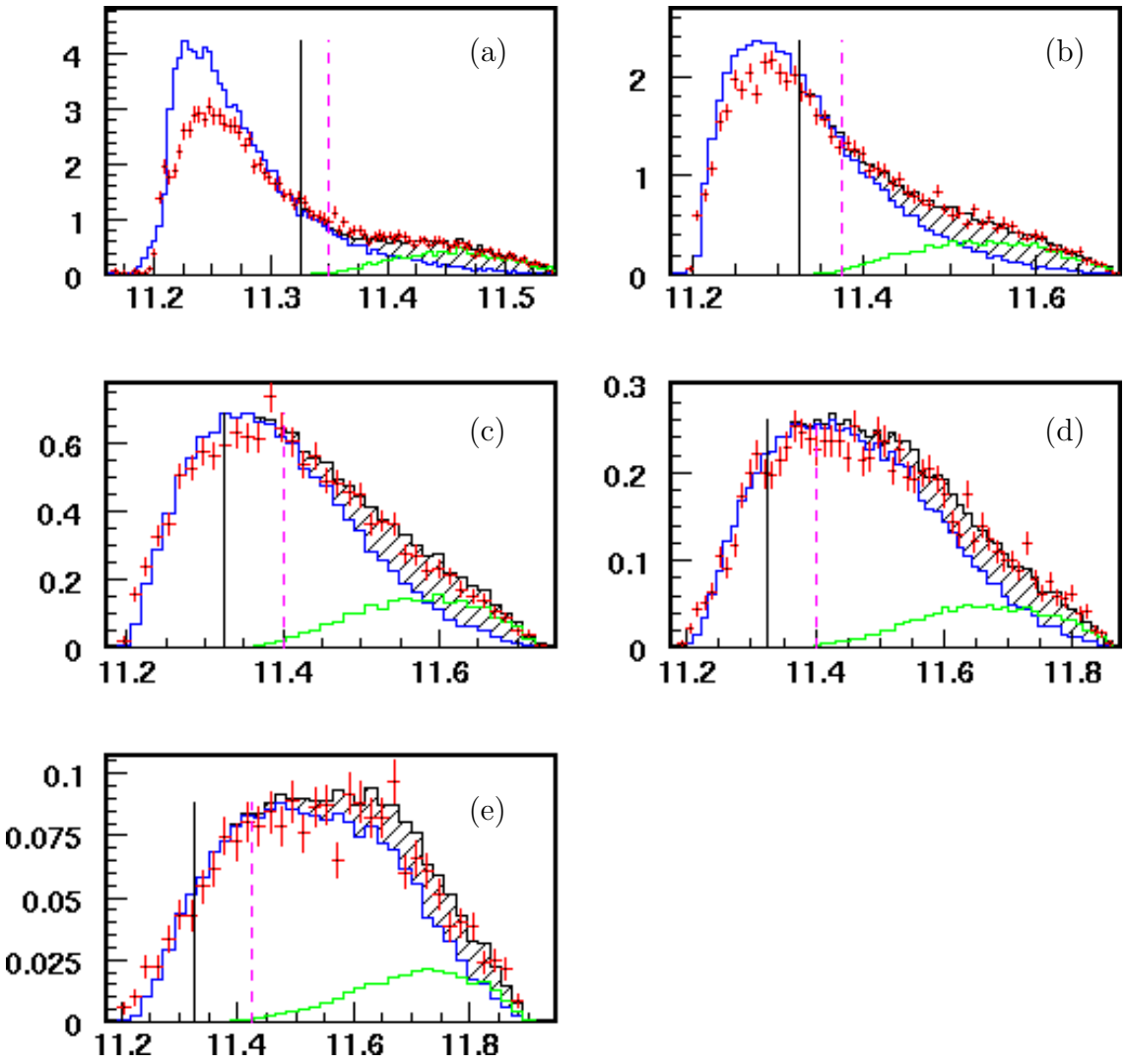

Figure 4-9: Nuclear missing mass distributions (in GeV/c^2) for ^{12}C(e,e$'\pi^+$), and (a) at Q^2=1.1 (GeV/c)^2, (b) at Q^2=2.15 (GeV/c)^2, (c) at Q^2=3.0 (GeV/c)^2, (d) at Q^2=3.9 (GeV/c)^2, and, (e) at Q^2=4.7 (GeV/c)^2. The experimental data are shown (red crosses) with the single-pion simulation (blue lines, or black in b/w) and the multiple-pion simulation (green lines, or gray in b/w). The shaded (black) area shows the sum of the single and multiple-pion simulation. The single-pion simulation and multiple-pion simulation were normalized to match the experimental data. The solid, vertical lines represent the position of the threshold for double-pion production (11.34 (GeV/c^2)). The dashed, magenta lines represent the position of the cut used in πCT.

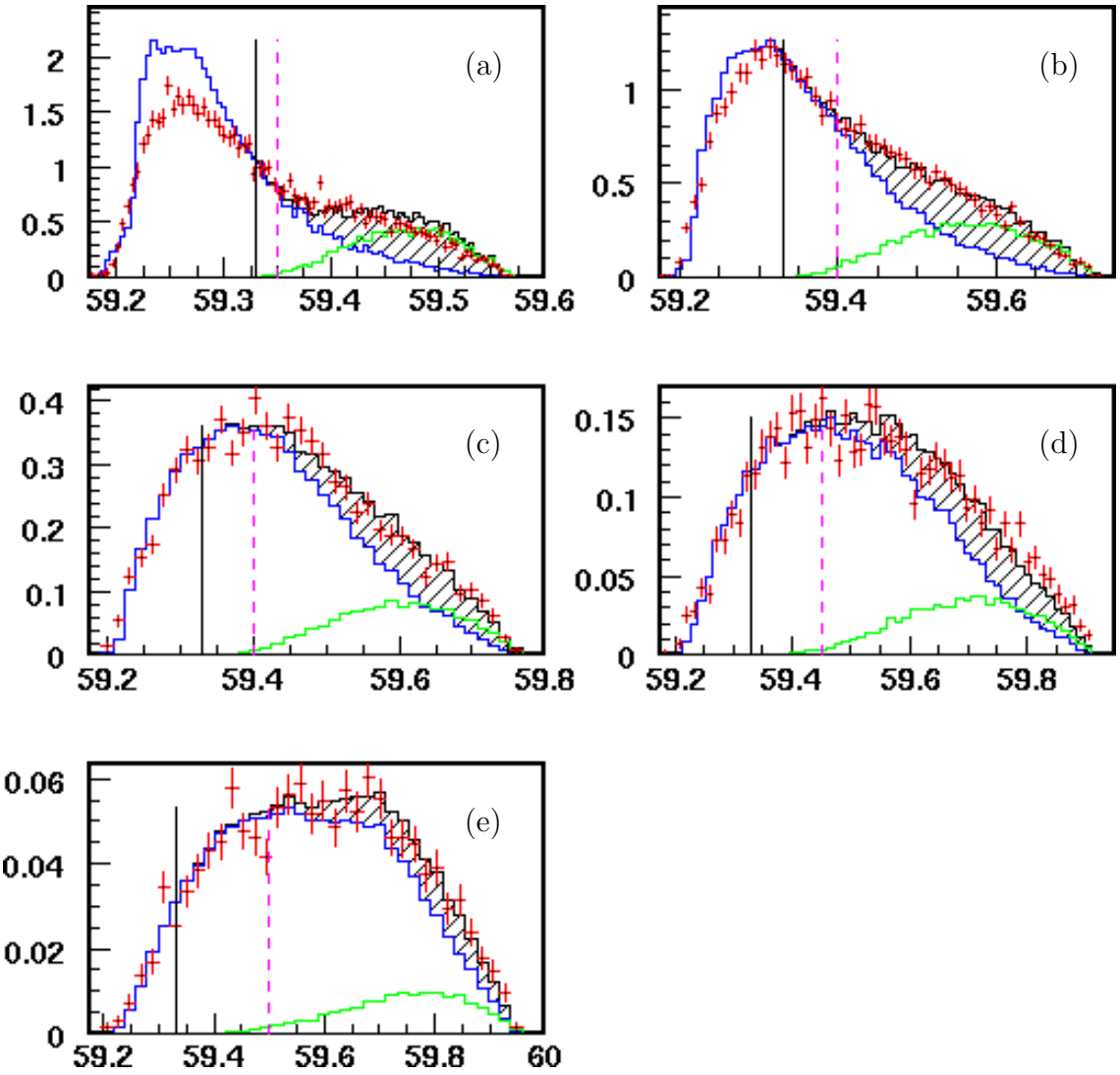

Figure 4-10: Nuclear missing mass distributions (in GeV/c^2) for ^{63}Cu(e,e′π^+). The symbols used in this figure are the same as in Figure 4-9.

Q^2 (GeV)^2	E_e (GeV)	HMS polarity	SOS polarity	p_e (GeV/c)	θ_e (deg)	p_p (GeV/c)	θ_p (deg)
4.511	4.021	+	-	1.582	50.05	3.225	22.08
6.1	5.012	+	-	1.703	50.05	4.111	18.67
7.47	5.767	+	-	1.673	51.63	4.864	16.16

Table 4.6: Spectrometer settings for hydrogen e-p elastic measurements.

4.9 e-p elastic scattering

Normalized yields from the experimental data and the Monte Carlo were compared using e-p elastic scattering to verify the accuracy of the spectrometer acceptance in the Monte Carlo. The "Rosenbluth" parameterizations of the elastic form factors determined by J. Arrington in Ref. [80] were used in the simulation, and are given by

$$\begin{aligned} G_E(Q^2) &= \frac{1}{1+3.226Q^2+1.508Q^4-0.3773Q^6+0.611Q^8-0.1853Q^{10}+0.01596Q^{12}} \\ G_M(Q^2)/\mu_p &= \frac{1}{1+3.19Q^2+1.355Q^4+0.151Q^6-0.0114Q^8+0.000533Q^{10}-0.000009Q^{12}}, \end{aligned} \tag{4.20}$$

where μ_p is the magnetic dipole moment of the proton and Q^2 values are in (GeV/c)^2. Furthermore, the parameterization for $G_E(Q^2)$ was set equal to $G_D(Q^2) = [1+Q^2/(0.71\ \text{GeV}^2)]^{-2}$ above $Q^2 = 6$ GeV/c^2, as described in Ref. [80]. Corrections for proton absorption (Section 3.9) were applied to the experimental normalized yield. The central kinematic settings of the spectrometers for the e-p elastic measurements are given in Table 4.6.

The reconstructed angles and momenta of the two spectrometers for the e-p elastic setting at $Q^2 = 6.1$ (GeV/c)^2 are compared to the simulated distributions in Figure 4-11. The reasonable agreement between the distributions indicate the acceptance of the spectrometers in the Monte Carlo is close to the experiment. The results for the ratio of the experimental normalized yields over the equivalent Monte Carlo normalized yields for all kinematic settings are shown in Figure 4-12 together with measurements of the H(e,e′p) cross section from Refs. [81, 82]. These data were chosen because they were measured at $\theta_e \approx 50^\circ$.

The point-to-point variation of the data in Figure 4-12 is small ($< \pm 1\%$), which is an indication that the acceptance is understood at the level of 1%. However, the experimental normalized yield is on average 5% higher than the equivalent Monte Carlo normalized yield. This is somewhat inconsistent with world data available at these kinematics. Since

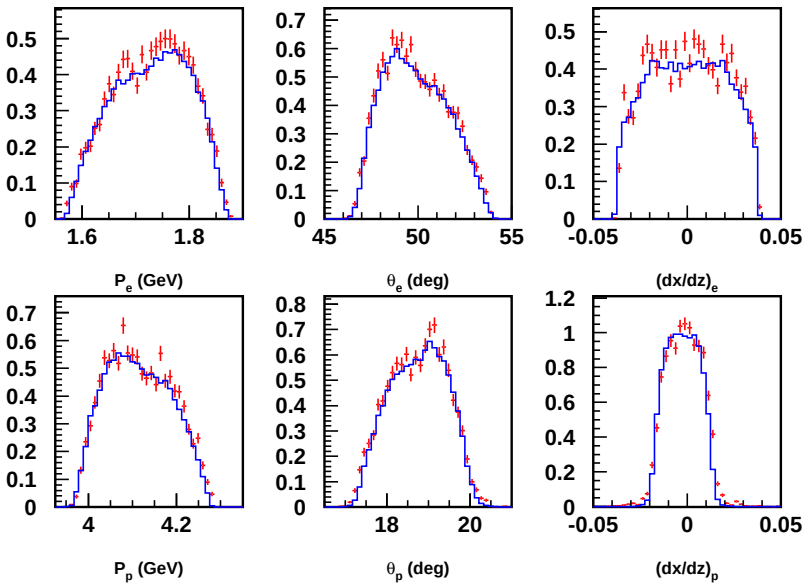

Figure 4-11: Monte Carlo and experimental H(e,e′p) distributions for the setting at $Q^2 = 6.1$ $(\mathrm{GeV/c})^2$. Monte Carlo distributions are the blue, solid lines and experimental data are the red crosses. Errors bars are statistical only. The dx/dz distribution is often called "xptar" and is the gradient of tracks with the x-axis pointing up and the z axis pointing from the target to the center of the spectrometer.

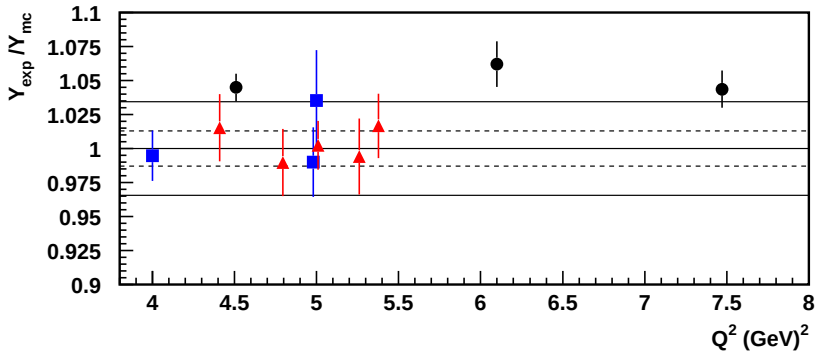

Figure 4-12: Ratio of experimental and Monte Carlo H(e,e′p) normalized yields (black, circles). The error bars for these data are statistical only. The dashed lines indicate the point-to-point systematic uncertainty between the data points and the solid lines indicate the overall systematic uncertainty. The estimated model uncertainty (2-3% at the lowest Q^2 and 3-4% at the other two data points) has not been included. Experimental data from Ref. [81] (red, triangles) and Ref. [82] (blue, squares) divided by the H(e,e′p) cross section using the same parameterization for the elastic form factors are shown for comparison.

the detailed shapes of the various spectrometer reconstructed quantities match very well with the simulations, the observed discrepancy could point to a normalization issue at the level of ∼5%. It should also be pointed out that the SOS acceptance is known to be less well understood at large angles and these data were taken at large angles.

4.10 Iteration of the model cross section

The Monte Carlo model of the elementary ^{1}H(e,e$'\pi^+$) cross section was iterated to match the data. The initial cross section (Section 1.7) was multiplied by a correction function, $C_{\rm H}(W, Q^2, t, \phi_{pq})$, and the procedure is described in Ref. [31]. It was assumed that the initial model used in this analysis (Equation 1.21) described the gross behavior of the cross section over the acceptance, such as the Q^{-4} behavior of the Mott cross section. The normalization and small deviations in the energy and angular distributions between the hydrogen model and the hydrogen experimental data were corrected by $C_{\rm H}(W, Q^2, t, \phi_{pq})$, which is described below.

The correction function was fit using a different function for each kinematic setting (Table 2.4). It was assumed to be factorizable, such that

$$C_{\rm H}(W, Q^2, t, \phi_{pq}) = O(W)K(Q^2)T(t)F(\phi_{pq}), \tag{4.21}$$

which follows from our assumption that $C_{\rm H}(W, Q^2, t, \phi_{pq})$ only provides a small adjustment to the model cross section. The iterated cross section was given by

$$\left(\frac{d^5\sigma_{\rm H}}{d\Omega_{e'}dE_{e'}d\Omega_\pi}\right)^{\rm itr} = O(W)K(Q^2)T(t)F(\phi_{pq})\left(\frac{d^5\sigma_{\rm H}}{d\Omega_{e'}dE_{e'}d\Omega_\pi}\right)^{\rm model}. \tag{4.22}$$

The correction functions, $O(W)$, $K(Q^2)$, $T(t)$ and $F(\phi_{pq})$, each contained at most three free parameters and were second order polynomials, with the exception of $F(\phi_{pq})$. $F(\phi_{pq})$ was given by

$$F(\phi_{pq}) = c_1 + c_2 \times \cos(\phi_{pq}) + c_3 \times \cos(2\phi_{pq}), \tag{4.23}$$

where c_1, c_2 and c_3 are free parameters.

The iteration procedure began with making 1-dimensional histograms of W using the experimental data and the Monte Carlo. The histogram from the experimental data was

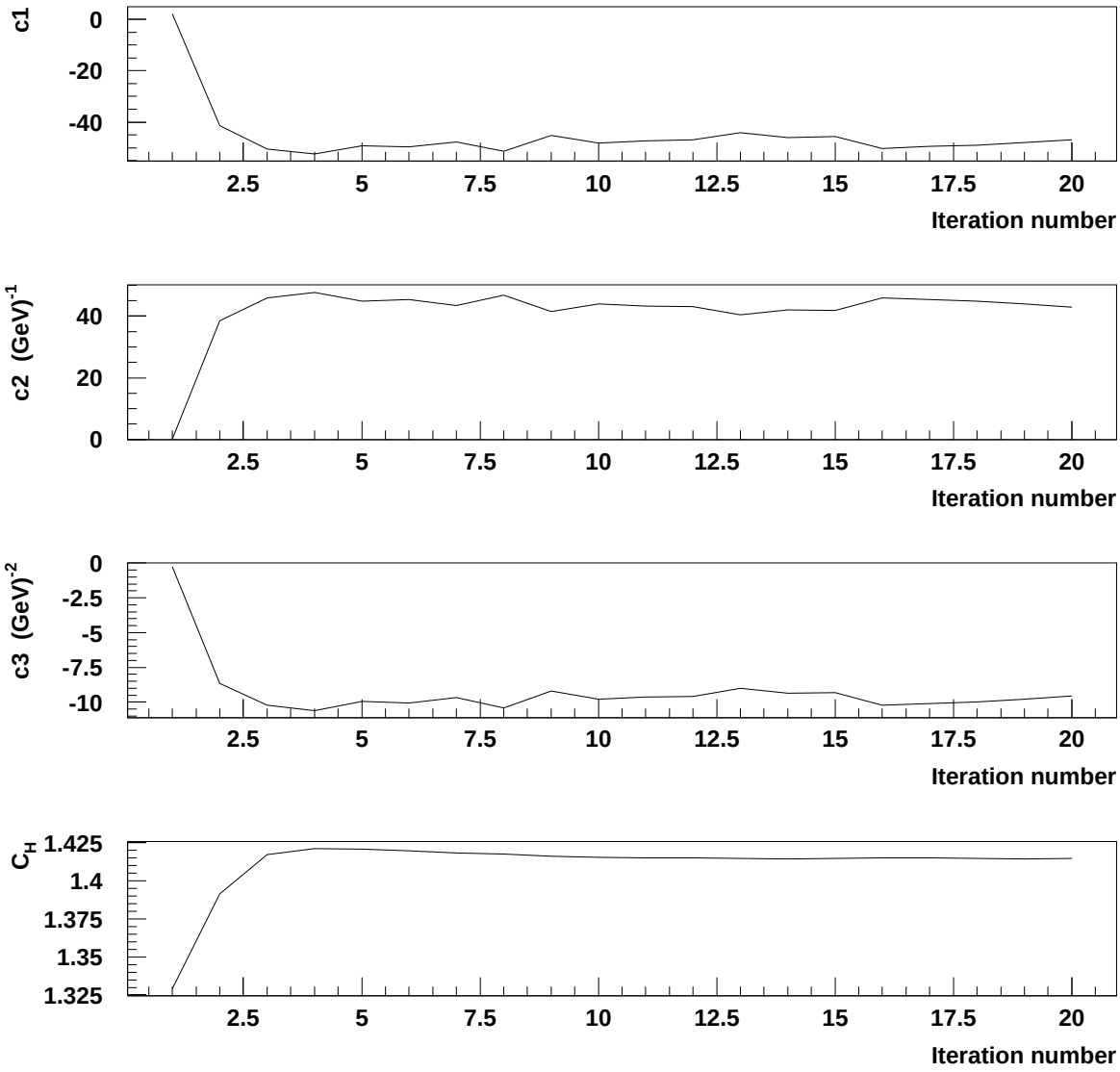

Figure 4-13: Iteration of the Monte Carlo cross section for H(e,e$'\pi^+$) at Q^2 = 1.1 (GeV/c)^2. The first three plots show the convergence of the coefficients of $O(W) = c_1 + c_2 W + c_3 W^2$ vs. the iteration number. The bottom plot shows the entire correction function $C_H = O(W)K(Q^2)T(t)F(\phi_{pq})$ evaluated at the central kinematics of the spectrometers. This quantity was 1.415 after 10 iterations, which means that the final Monte Carlo cross section at the central kinematics was 41.5% larger than the inital cross section.

divided, bin-by-bin, by the histogram from the Monte Carlo and the ratio was fit with the correction function $O(W)$. The function with the new coefficients was called $O_1(W)$. A histogram of Q^2 from the Monte Carlo data was produced where the model cross section was modified according to

$$\left(\frac{d^5\sigma_{\rm H}}{d\Omega_{e'}dE_{e'}d\Omega_\pi}\right)^{\rm itr} = O_1(W)T_0(t)F_0(\phi_{pq})\left(\frac{d^5\sigma_{\rm H}}{d\Omega_{e'}dE_{e'}d\Omega_\pi}\right)^{\rm model}, \tag{4.24}$$

where $T_0 = F_0 = 1$. The unmodified 1-dimensional histogram of the experimental data was then divided by this histogram of Q^2 and the resulting histogram of the ratio was fit with $K(Q^2)$. The function with the new coefficients was called $K_1(Q^2)$. The model cross section was modified again according to

$$\left(\frac{d^5\sigma_{\rm H}}{d\Omega_{e'}dE_{e'}d\Omega_\pi}\right)^{\rm itr} = O_1(W)K_1(Q^2)F_0(\phi_{pq})\left(\frac{d^5\sigma_{\rm H}}{d\Omega_{e'}dE_{e'}d\Omega_\pi}\right)^{\rm model}, \tag{4.25}$$

and was used in the fitting of $T_1(t)$. $F_1(\phi_{pq})$ was fit following the same procedure. The iteration procedure then returned to fitting W, and the correction function for W from the first iteration was removed. The model cross section when fitting W in the second iteration was

$$\left(\frac{d^5\sigma_{\rm H}}{d\Omega_{e'}dE_{e'}d\Omega_\pi}\right)^{\rm itr} = K_1(Q^2)T_1(t)F_1(\phi_{pq})\left(\frac{d^5\sigma_{\rm H}}{d\Omega_{e'}dE_{e'}d\Omega_\pi}\right)^{\rm model}, \tag{4.26}$$

The procedure was repeated until the coefficients in the correction function converged and the correction function upon completion of n iterations was given by

$$C_{\rm H}(W, Q^2, t, \phi_{pq}) = O_n(W)K_n(Q^2)T_n(t)F_n(\phi_{pq}). \tag{4.27}$$

The coefficients during an iteration procedure are shown in Figure 4-13. No significant change in the value of the correction function evaluated at the central kinematics was seen after 10 iterations.

The coefficients of the correction functions determined during the iteration of the elementary cross sections were the same parameters used in the model for targets with $A > 1$. No transformation of the correction function was necessary due to the Fermi motion of the proton as the variables W, Q^2 and t were invariant and ϕ_{pq} did not change when it was evaluated in the lab frame compared to the γ^*-N center of mass frame. Equation 1.17 was

modified to include the iterations

$$\begin{aligned}\frac{d^6\sigma_{\rm A}}{d\Omega_{e'}dE_{e'}d\Omega_\pi dP_\pi} &= \int dE_m d\boldsymbol{p}_m S(E_m,\boldsymbol{p}_m) \\ &\quad \times C_{\rm H}(W,Q^2,t,\phi_{pq})\frac{d^5\sigma_{\rm H}}{d\Omega_{e'}dE_{e'}d\Omega_\pi}\delta\left(h(E_m,\boldsymbol{p}_m)-P_\pi\right)\end{aligned} \tag{4.28}$$

The systematic uncertainty due to the iteration of the elementary cross section was a point-to-point uncertainty as using an imperfect elementary cross section model will influence the Monte Carlo equivalent yields differently for each type of target. There is also an uncertainty in the absolute cross section due to the iteration procedure, which will be discussed in the next section. The point-to-point uncertainty was determined by changing the iteration procedure, such as changing the initial cross section. The Mott cross section and the parameterizations of the elementary cross section described in Refs. [33, 65] were used in the iteration procedure. The Mott cross section resulted in inconsistencies between the experimental data and the Monte Carlo distributions after the iteration procedure at all Q^2 settings and so was not used in the estimation of the uncertainty. The parameterizations of the elementary cross section in Refs. [33, 65] could not be used at some Q^2 settings as they gave negative values, however, the parameterization in Ref. [33] resulted in Monte Carlo distributions that had reasonable agreement with the experimental data for $Q^2 \leq 3$ (GeV/c)^2. The change in the nuclear transparency in this Q^2 range was less than 1.2% with this new procedure.

The systematic uncertainty due to the iteration of the elementary cross section was also estimated by changing the order in which the variables were iterated, using higher order correction functions (up to 3rd order) and reducing the ranges over which the correction functions were iterated. The nuclear transparency changed by at most 1.3% with these variations in the iteration procedure. An extreme case was also considered where the parameterization in Equation 1.21 was used without iterations and the nuclear transparency changed by less than 3%. This was considered an upper limit of the systematic error in the iteration procedure and showed how well the initial parameterization described the elementary cross section. We assumed that the uncertainty in the nuclear transparency was 1.5% due to the iteration procedure, and as the nuclear transparency involved the ratio of two Monte Carlo yields (Chapter 5), the point-to-point uncertainty in the Monte Carlo yield was assumed to be 1.1%.

4.11 Bin centering and experimental cross sections

In addition to the iterations performed in the construction of the elementary cross section, iterations were used for bin-centering the experimental data and extracting the absolute experimental cross sections at some point, $x_0 = (\omega_0,\ Q_0^2,\ \theta_0)$, near the center of the acceptance. The model for the cross section in the Monte Carlo was adjusted using correction functions until the distributions of ω, Q^2, θ_{pq} and ϕ_{pq} from the Monte Carlo matched the distributions from the experimental data. Separate iterations were performed for each kinematic setting. We then assumed that the Monte Carlo model described the kinematic dependence of the cross section across the acceptance, without necessarily having the correct normalization. The model cross section was scaled by the normalized yield, $Y_{\rm exp}$, and for the hydrogen target, the bin-centered experimental cross section was given by

$$\left(\frac{d^5\sigma_{\rm H}}{d\Omega_{e'}dE_{e'}d\Omega_\pi}\right)^{\rm exp}_{x_0} = \frac{\bar{Y}_{\rm exp}}{\bar{Y}_{\rm SIMC}} \times \left(\frac{d^5\sigma_H}{d\Omega_{e'}dE_{e'}d\Omega_\pi}\right)^{\rm model}_{x_0}, \tag{4.29}$$

where the subscript, x_0, on the model cross section indicates that it was evaluated at a particular point $(\omega_0,\ Q_0^2,\ \theta_0)$ in the acceptance. For targets with $A > 1$, the bin-centered experimental cross section was given by

$$\left(\frac{d^6\sigma_{\rm A}}{d\Omega_{e'}dE_{e'}d\Omega_\pi dP_\pi}\right)^{\rm exp}_{x_0} = \frac{\bar{Y}_{\rm exp}}{\bar{Y}_{\rm SIMC}} \times \left(\frac{d^6\sigma_A}{d\Omega_{e'}dE_{e'}d\Omega_\pi dP_\pi}\right)^{\rm model}_{x_0}. \tag{4.30}$$

The model cross sections at the particular point, x_0, near the center of the acceptance, $\left(\frac{d^5\sigma_H}{d\Omega_{e'}dE_{e'}d\Omega_\pi}\right)^{\rm model}_{x_0}$ and $\left(\frac{d^6\sigma_A}{d\Omega_{e'}dE_{e'}d\Omega_\pi dP_\pi}\right)^{\rm model}_{x_0}$, were determined through what is called a point Monte Carlo simulation. The point Monte Carlo simulation was performed with all extraneous processes (radiation, multiple scattering, Coulomb corrections, etc.) turned off and the scattered electron kinematics and pion angles generated randomly within a very narrow phase space volume that corresponded to ω_0, Q_0^2 and θ_0. The magnitude of the pion momentum was not generated, even for nuclear targets, as its value was fixed after generating E_m and $\mathbf{p}_m$ in the spectral function and by conserving four-momentum in the quasifree picture. However, a narrow range of P_π was selected using cuts on this variable. The model cross sections at the particular point, x_0, near the center of the acceptance, was

given by

$$\left(\frac{d^5\sigma_{\rm H}}{d\Omega_{e'}dE_{e'}d\Omega_\pi}\right)^{\rm itr}_{x_0} = \frac{Y^{\rm itr}_{\rm point}}{\mathcal{L}\times(\Delta\Omega_{e'}\Delta E_{e'}\Delta\Omega_\pi)}, \tag{4.31}$$

for the hydrogen target, and

$$\left(\frac{d^6\sigma_{\rm A}}{d\Omega_{e'}dE_{e'}d\Omega_\pi dP_\pi}\right)^{\rm exp}_{x_0} = \frac{Y^{\rm itr}_{\rm point}}{\mathcal{L}\times(\Delta\Omega_{e'}\Delta E_{e'}\Delta\Omega_\pi\Delta P_\pi)}, \tag{4.32}$$

for the targets with $A > 1$, where $\mathcal{L}$ was the simulated luminosity and $(\Delta\Omega_{e'}\Delta E_{e'}$ ...) was the volume of the narrow phase space region over which kinematics were generated (or selected using cuts in the case of P_π) in the point Monte Carlo simulation.

Chapter 5

Results

The nuclear transparencies for ^{2}H, ^{12}C, ^{27}Al, ^{63}Cu and ^{197}Au targets are shown in this chapter together with the super ratio of A>2 nuclei to deuterium and A>12 nuclei to carbon. The dependence of the nuclear transparency on the nucleon number will be presented and the parameterization $T = A^{\alpha-1}$ will be fitted to the results. Results from additional kinematic settings that were used to check the quasifree model, the L-T separations at $Q^2 = 2.15$ (GeV/c)^2 and 4.0 (GeV/c)^2 and the W vs. k_π test setting, will be shown. Finally, a study of various options of the quasi-free pion electro-production model used in the analysis will be presented.

5.1 Nuclear transparency

The nuclear transparency, T, was formed using the experimental charge normalized yield, $\bar{Y}$, divided by the charge normalized Monte Carlo equivalent yield, $\bar{Y}_{\rm SIMC}$. For a given target with nucleon number, A, the nuclear transparency was

$$T = \frac{\left(\bar{Y}/\bar{Y}_{\rm SIMC}\right)_A}{\left(\bar{Y}/\bar{Y}_{\rm SIMC}\right)_{\rm H}}, \tag{5.1}$$

where the denominator is the ratio of the yields for the ^{1}H target. The nuclear transparency, shown as a function of Q^2 in Figure 5-1, was determined under the following options of the model:

- Nuclear missing mass cuts to minimize double-pion events

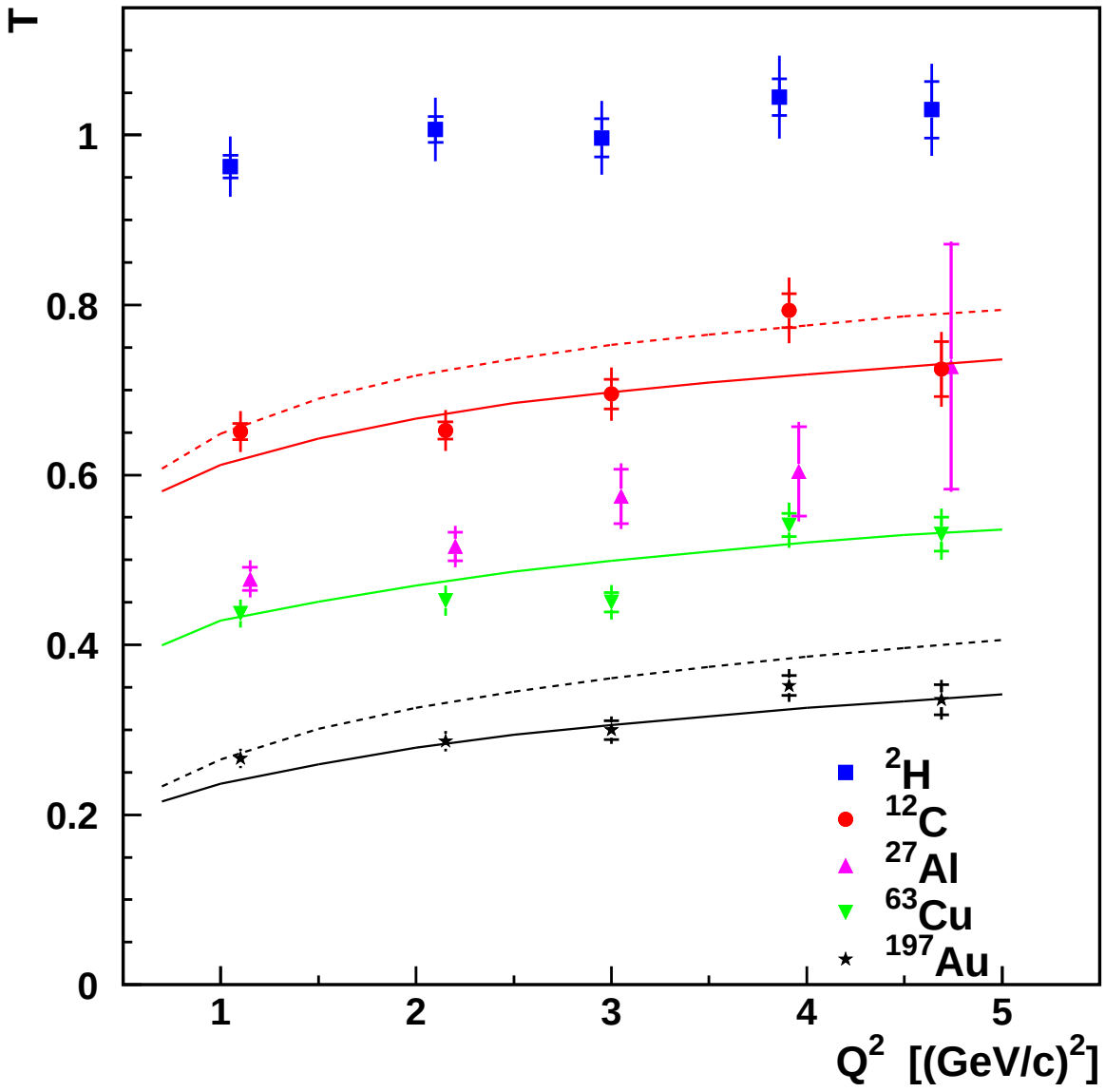

Figure 5-1: Nuclear transparency, T, determined during the πCT analysis. The inner error bars are the statistical uncertainties, the outer error bars are the statistical and point-to-point systematic uncertainties added in quadrature. The solid and dashed lines are theoretical calculations using end-point and asymptotic distribution amplitudes, respectively [45]. The upper, middle and lower lines are for ^{12}C, ^{63}Cu and ^{197}Au and are scaled by 1.09, 0.85 and 0.88, respectively.

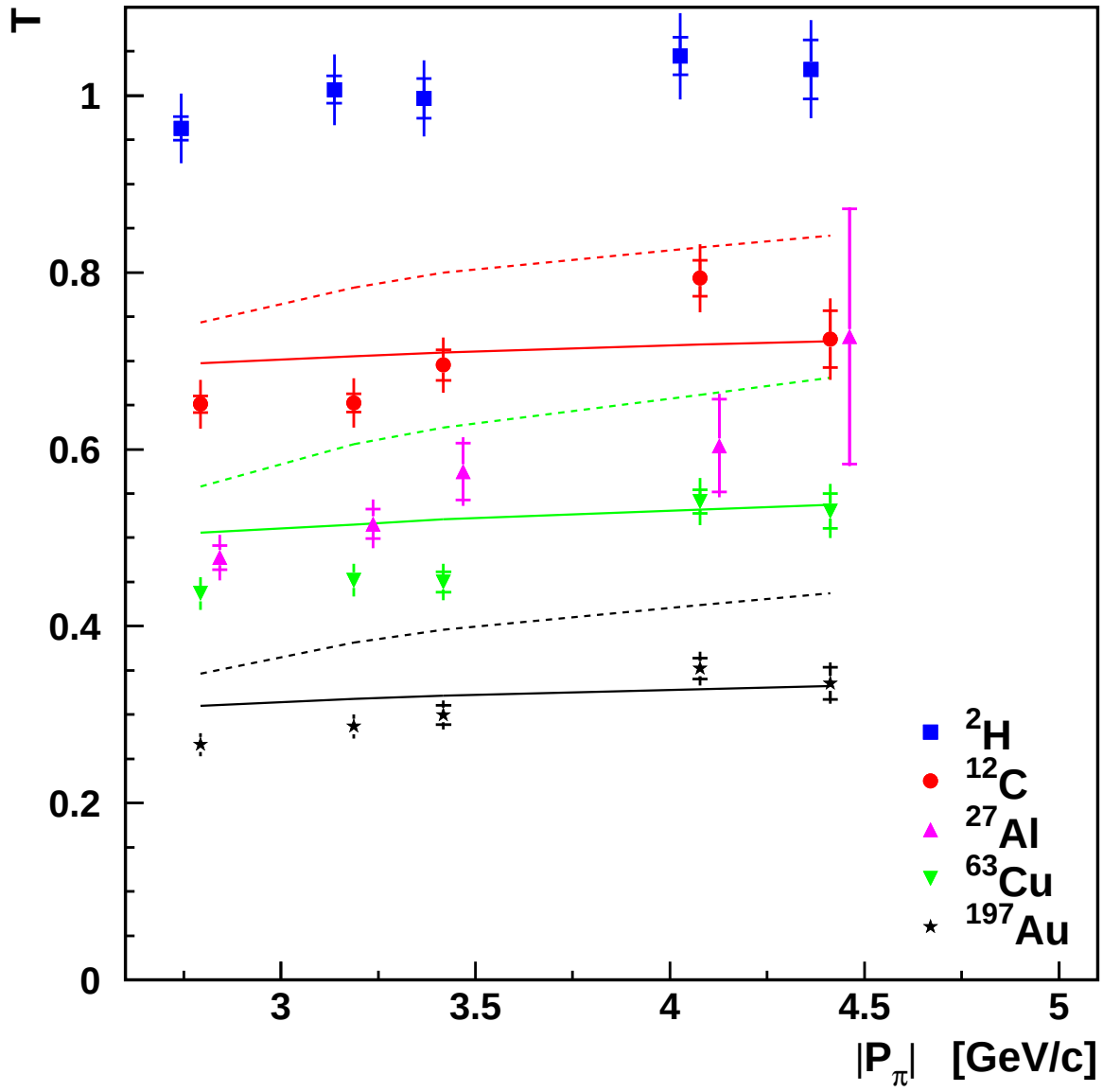

Figure 5-2: Nuclear transparency, T, vs. the magnitude of the outgoing pion momentum in the laboratory frame, $|\mathbf{P}_\pi|$. The inner error bars are the statistical uncertainties and the outer error bars are the statistical and point-to-point systematic uncertainties added in quadrature. The solid lines are Glauber calculations and the dashed lines are Glauber plus color transparency (both sets of curves are from Refs. [8, 83]). The color transparency calculation assumed $\Delta M^2 = 0.7$ (GeV/c^2)^2. The upper, middle and lower lines are for ^{12}C, ^{63}Cu and ^{197}Au and are scaled by 1.13, 1.37 and 1.25, respectively.

Q^2 (GeV/c)^2	^{2}H	^{12}C	^{27}Al
1.10	0.963±0.013±0.033	0.651±0.010±0.022	0.478±0.014±0.017
2.15	1.007±0.015±0.034	0.652±0.010±0.022	0.516±0.017±0.018
3.00	0.997±0.022±0.037	0.695±0.017±0.026	0.575±0.032±0.022
3.91	1.045±0.021±0.044	0.793±0.020±0.033	0.604±0.053±0.026
4.69	1.030±0.033±0.043	0.724±0.032±0.030	0.728±0.144±0.031
Q^2 (GeV/c)^2	^{63}Cu	^{197}Au	
1.10	0.437±0.007±0.015	0.266±0.005±0.010	
2.15	0.452±0.007±0.016	0.287±0.007±0.010	
3.00	0.450±0.011±0.017	0.300±0.011±0.012	
3.91	0.541±0.013±0.023	0.352±0.012±0.015	
4.69	0.530±0.020±0.023	0.335±0.018±0.015	

Table 5.1: The nuclear transparency values for ^{2}H, ^{12}C, ^{27}Al, ^{63}Cu and ^{197}Au targets. The first uncertainty quoted is the statistical uncertainty and the second is the point-to-point systematic uncertainty.

- E_m=0 for the model of the energy of the proton
- No correlations included in the spectral function
- Pauli blocking using the Fantoni and Pandharipande distribution function
- Coulomb corrections for the outgoing pion (E_π was increased by $\bar{V}$)

is shown as a function of Q^2 in Figure 5-1. The nuclear transparency is shown as a function of P_π in Figure 5-2 and the values for the nuclear transparency are given in Table 5.1. The point-to-point and overall systematic uncertainties are discussed in Section 5.2. Calculations of the nuclear transparency were scaled to agree with the experimental data at Q^2=4.7 (GeV/c)^2.

The results presented in Figure 5-1 suggest an enhancement in the nuclear transparency that is consistent with the theoretical calculations shown in the same figure within the experimental and model dependent uncertainties. The theoretical calculations in Figure 5-1 use the pion distribution amplitude and models using an end point dominated [46, 47] and a centrally dominated [48] model are shown. The pion distribution amplitude provides insight into the nonperturbative structure of the pion. The centrally dominated model uses the asymptotic limit of perturbative QCD to determine the pion distribution amplitude, while the end-point dominated model uses measured moments of the pion distribution amplitude to construct a parameterization for this function. The results of the nuclear

transparency vs. P_π presented in Figure 5-2 also show an enhancement in the nuclear transparency that is in good agreement with the theoretical calculation that includes CT with $\Delta M^2 = 0.7$ $(\mathrm{GeV/c^2})^2$ in Refs. [8, 83]. This calculation uses the quantum diffusion model to describe the expansion of the pion, which is a perturbative calculation in the quark basis. A reliable baseline in πCT will help to distinguish better between the various CT predictions. A reliable baseline is lacking at the lower Q^2 in Figure 5-1 and lower P_π in Figure 5-2 and awaits a better understanding of n-N FSI (interactions between the recoiling neutron and the spectator nucleons), Pauli blocking and medium modification of the nucleons.

The goodness of fit of the Glauber transparency in Figure 5-2 was determined after normalizing these curves to match the data using the least squares method. The number of degrees of freedom was 4 (5 data points - 1 fitted parameter) and the residual was 13.0, 11.1 and 8.8 for the gold, copper and carbon targets, respectively. The Glauber model is rejected at the 98.9%, 97.5% and 93.4% confidence level for the gold, copper and carbon targets, respectively. However, the 4.3-10.6% model dependent uncertainty in the experimental results was not included in this goodness of fit calculation.

The nuclear transparency is plotted vs. the nucleon number, A, in Figure 5-3. The data was fit with the parameterization $T = A^{\alpha-1}$ and the values of α determined from the fit at each Q^2 are given in Table 5.2. This form of the parameterization is a direct consequence of the parameterization of nuclear cross sections as $\sigma = \sigma_0 A^\alpha$ and a positive slope of α with increasing Q^2 is considered a signal of CT. This parameterization represents a very crude approximation which usually suffers from poor χ^2 in fits to the data. However, the parameter α seems to be a robust result over a wide range of energies and probes and is thus a powerful technique for studying the effects of CT. The results for α can be compared to the absorption cross section in π-A scattering, which were parameterized with $\sigma(A) = \sigma_0 A^\alpha$. The value of α determined in these experiments was $\alpha = 0.75 - 0.77$ [51]. The value of α in π-A scattering is compared to the results from πCT in Figure 5-4.

The results in Figure 5-3 show a behavior that could be due to color transparency. The dependence of the nuclear transparency on the nucleon number becomes curved with increasing Q^2, with the nuclear transparency for small A nuclei rising further above the fitted line. Furthermore, the fitted values for α increased by 6.6% over the Q^2 range of these measurements and were approximately 8.3% larger than the value determined from

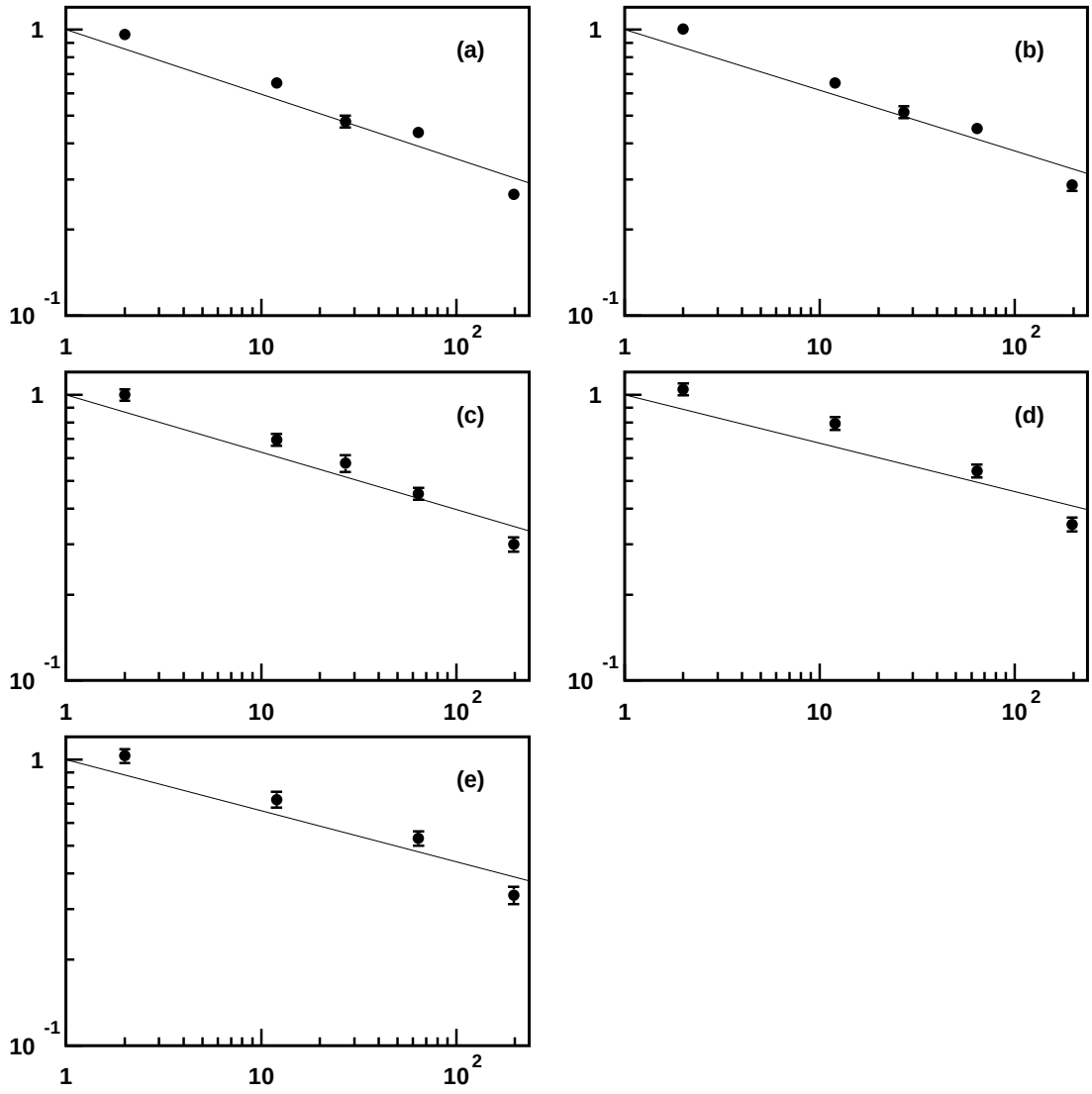

Figure 5-3: The nuclear transparency vs. the nucleon number, A, for (a) Q^2=1.1 (GeV/c)^2, (b) Q^2=2.15 (GeV/c)^2, (c) Q^2=3.0 (GeV/c)^2, (d) Q^2=3.9 (GeV/c)^2, and, (e) Q^2=4.7 (GeV/c)^2. The lines are fits to the experimental data using the parameterization $T = A^{\alpha-1}$. The error bars are the statistical and overall (point-to-point and normalization) systematic uncertainties added in quadrature. The values of α determined from the fit at each Q^2 are given in the text.

Q^2 (GeV/c)^2	α
1.10	0.774±0.005
2.15	0.788±0.005
3.00	0.799±0.007
3.91	0.830±0.007
4.69	0.821±0.009

Table 5.2: The values for the parameter, α, which were determined by fitting the experimental data with the statistical and overall (point-to-point and normalization) systematic uncertainties added in quadrature.

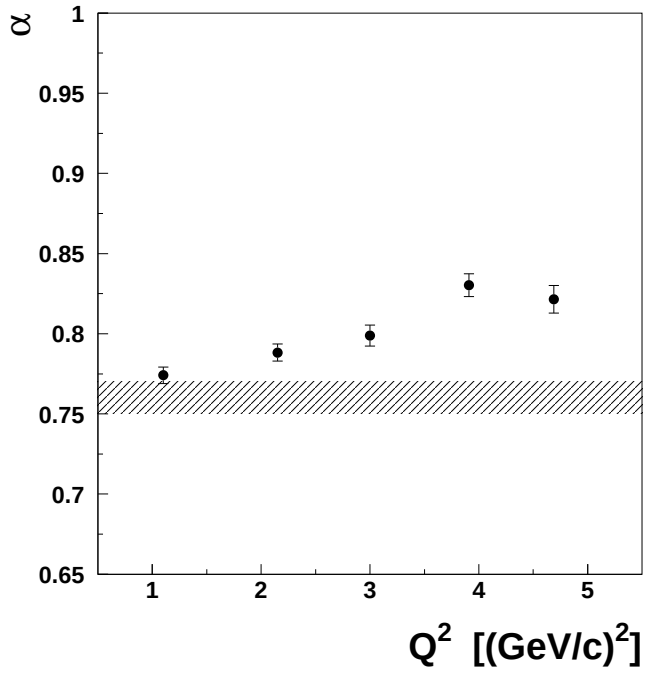

Figure 5-4: The parameter, α, vs. Q^2. The circles are from the πCT analysis and the error bars represent the statistical and overall (point-to-point and normalization) systematic uncertainties added in quadrature. The band shows the measured values of α from π-A scattering for pion momentum from several GeV/c to hundreds of GeV/c.

π-A scattering.

The CT signal is reduced when we form the super ratio, $R_{A,A'}$, given by

$$R_{A,A'} = \frac{\left(\bar{Y}/\bar{Y}_{\mathrm{SIMC}}\right)_A}{\left(\bar{Y}/\bar{Y}_{\mathrm{SIMC}}\right)_{A'}}. \tag{5.2}$$

This is because any enhancement of the experimental yield in the numerator will partially cancel with the enhancement in the denominator. However, it can be useful to examine the super ratio as the model uncertainty will be reduced, which is because errors due to assumptions in the quasifree model will cancel to first order. The super ratio with deuterium is shown in Figure 5-5 and with carbon in Figure 5-6. There appears to be a small enhancement of the super ratio with deuterium with Q^2 and the super ratio with carbon appears to be energy independent for all targets with nuclei heavier than carbon.

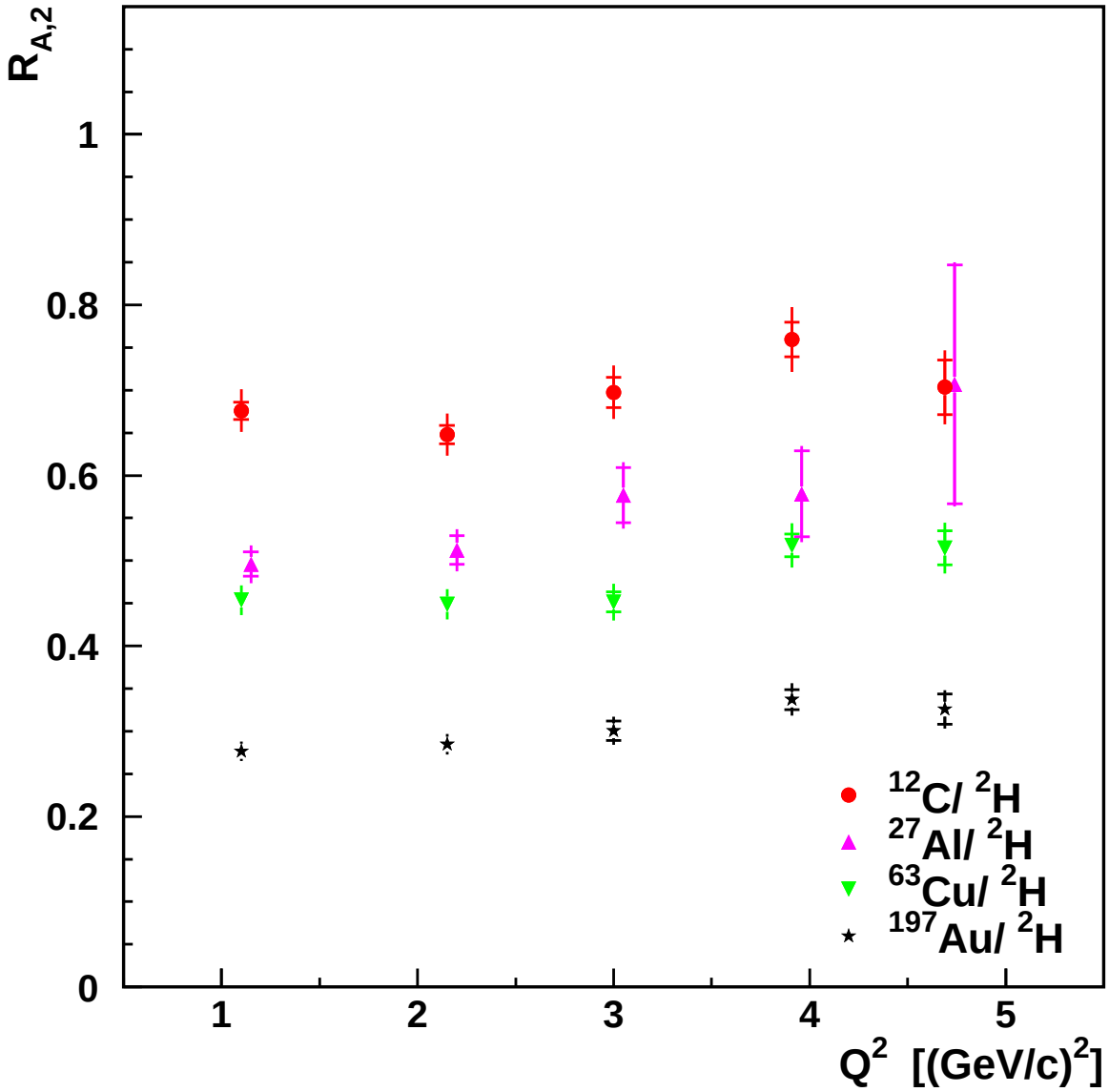

Figure 5-5: The $R_{A,2}$ super ratio vs. Q^2. The inner error bars are the statistical uncertainties, the outer error bars are the statistical and point-to-point systematic uncertainties added in quadrature.

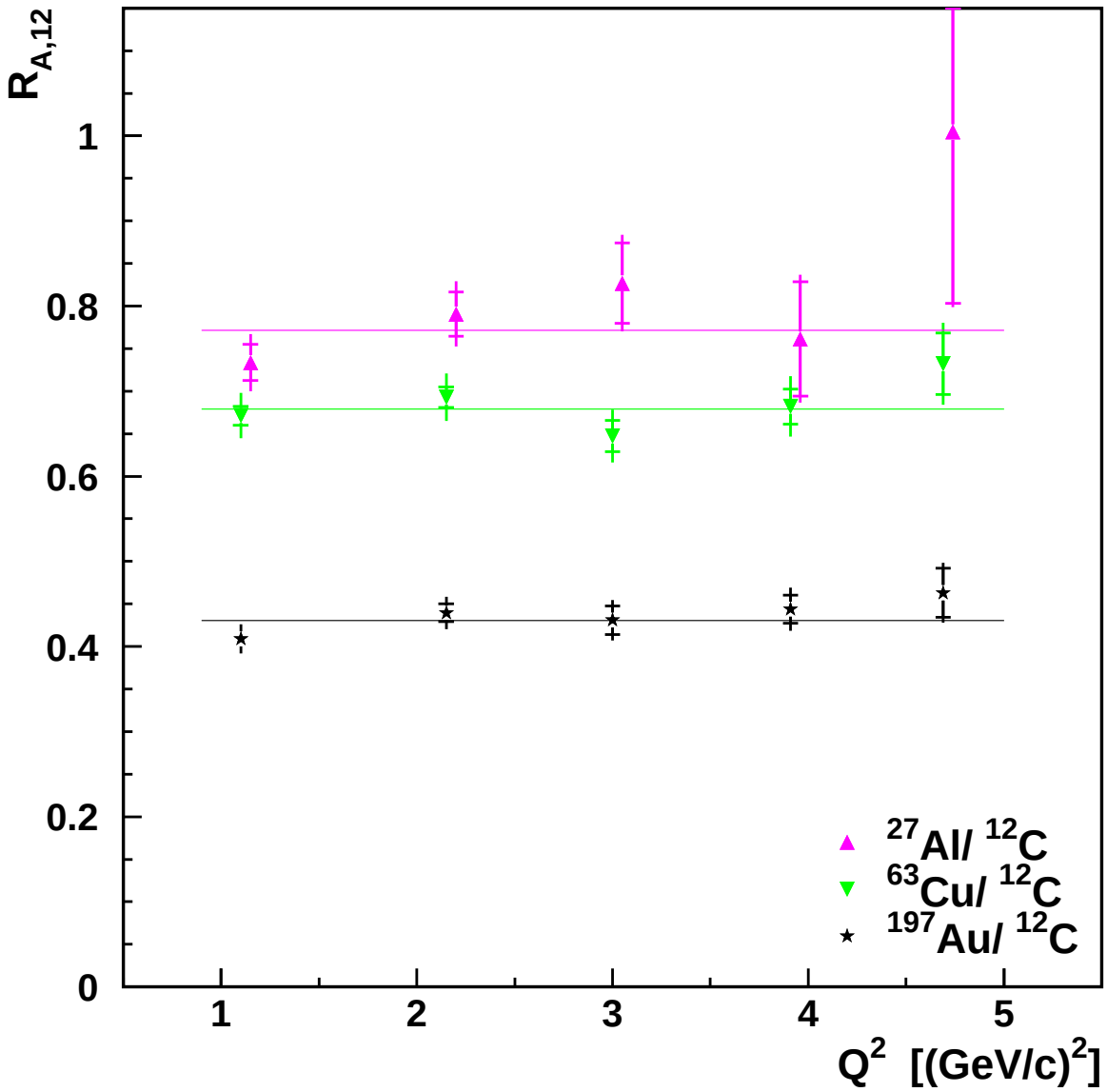

Figure 5-6: The $R_{A,12}$ super ratio vs. Q^2. The inner error bars are the statistical uncertainties, the outer error bars are the statistical and point-to-point systematic uncertainties added in quadrature. The upper, middle and lower horizontal lines are fitted to the data for the ^{27}Al, ^{63}Cu and ^{197}Au targets, respectively.

5.2 Error analysis

The statistical uncertainties in the charge normalized experimental yields were calculated for each run and were summed over the runs at a given kinematic setting to give the best estimate for the charge normalized yield, given by

$$\begin{aligned} \bar{Y} &= \left(\sum_i^n \frac{\bar{Y}_i}{\left(\bar{Y}_i/\sqrt{N_i}\right)^2} \right) \left(\sum_i^n \frac{1}{\left(\bar{Y}_i/\sqrt{N_i}\right)^2} \right)^{-1} \\ &= \left(\sum_i^n N_i/\bar{Y}_i \right) \left(\sum_i^n N_i/\bar{Y}_i^2 \right)^{-1}, \end{aligned}$$

where i represents the i^{th} run of a kinematic setting and N_i the number of events inside the experimental acceptance. The statistical uncertainty for the entire setting, $d\bar{Y}$, was

$$d\bar{Y} = \left(\sum_i^n N_i/\bar{Y}_i^2 \right)^{-\frac{1}{2}}. \tag{5.3}$$

The same acceptance and missing mass cuts that were applied to the experimental data were also applied to the Monte Carlo events. The Monte Carlo statistical error was determined in a similar manner, except N_i was replaced with the raw number of Monte Carlo particles that passed these cuts. The statistical uncertainty in the transparency, $dT_{\rm stat}$, was given by

$$dT_{\rm stat} = T \times \sqrt{\left([d\bar{Y}/\bar{Y}]^2 + [d\bar{Y}_{\rm SIMC}/\bar{Y}_{\rm SIMC}]^2\right)_A + \left([d\bar{Y}/\bar{Y}]^2 + [d\bar{Y}_{\rm SIMC}/\bar{Y}_{\rm SIMC}]^2\right)_{\rm H}}. \tag{5.4}$$

Three different types of systematic uncertainties in the normalized yields are shown in Table 5.3. The distinction between these types of uncertainties was based on how they contribute to the systematic uncertainty in the nuclear transparency. Point-to-point systematic uncertainties in the normalized yield contributed to both the normalization and point-to-point systematic uncertainties in the nuclear transparency. $d\bar{Y}_{\rm pt-to-pt}$, was the point-to-point systematic uncertainty in the normalized yield that contributed to the point-to-point systematic uncertainty in the nuclear transparency. $d\bar{Y}_{\rm norm}$, was the point-to-point systematic uncertainty in the normalized yield that contributed to the normalization systematic uncertainty in the nuclear transparency. $d\bar{Y}_{\rm pt-to-pt}$ contributed to the numerator and denominator in Equation 5.1 and the point-to-point systematic uncertainty in the nu-

Correction	$\frac{d\bar{Y}_{\rm pt-to-pt}}{\bar{Y}}$ (%)	$\frac{d\bar{Y}_{\rm norm}}{\bar{Y}}$ (%)	$\frac{d\bar{Y}_{\rm abs,norm}}{\bar{Y}}$ (%)	Section
HMS Cerenkov	0.2		0.3-0.5	3.2
SOS Cerenkov	0.2		0.3-0.5	3.2
Charge	0.4-0.9		0.4	2.2
Target thickness		0.5-1.0		2.3
Coincidence blocking	0.2			3.3
HMS Trigger	0.5			3.6
SOS Trigger	0.5			3.6
Dead time	0.5			3.7
HMS Tracking	1.0		1.0	3.8
SOS Tracking	0.5		0.5	3.8
Pion absorption		0.5	2.0	3.9
Pion decay	0.1		1.0	4.1
Coulomb corrections	0.0-1.0			4.2
Radiative corrections	1.0-2.0		2.0	4.5
Collimator	0.5		1.0	4.6
Acceptance	1.0		2.0	4.9
Iteration procedure	1.1			4.10 and 4.11
Multi-π contamination	0.0-0.4			4.8
Total	2.4-3.2	0.7-1.1		

Table 5.3: Systematic uncertainties in the normalized yields. The uncertainty, $d\bar{Y}_{\rm pt-to-pt}$, contributed to the point-to-point uncertainty in the nuclear transparency. $d\bar{Y}_{\rm norm}$ is the uncertainty that depends on the target nuclei and is independent of Q^2. $d\bar{Y}_{\rm abs,norm}$ is the uncertainty in the overall normalization due to uncertainties that are independent of the target nuclei and Q^2. In addition, there is a 4.3-10.6% model uncertainty that is described in the text.

clear transparency was given by

$$dT_{\rm pt-to-pt} = T \times \sqrt{\left(\frac{d\bar{Y}_{\rm pt-to-pt}}{\bar{Y}}\right)^2_{\rm A} + \left(\frac{d\bar{Y}_{\rm pt-to-pt}}{\bar{Y}}\right)^2_{\rm H}}. \tag{5.5}$$

The normalization systematic uncertainty in the nuclear transparency was given by

$$dT_{\rm norm} = T \times \sqrt{\left(\frac{d\bar{Y}_{\rm norm}}{\bar{Y}}\right)^2_{\rm A} + \left(\frac{d\bar{Y}_{\rm norm}}{\bar{Y}}\right)^2_{\rm H}}. \tag{5.6}$$

Normalization systematic uncertainties in the normalized yield, $d\bar{Y}_{\rm abs,norm}$, contributed to the systematic uncertainty in the absolute cross sections and canceled in the ratio between

targets. Therefore, these uncertainties did not contribute to the systematic uncertainty in the nuclear transparency.

The model uncertainty is an estimate of the uncertainty in the nuclear transparency due to corrections for Pauli blocking and nucleon correlations in the spectral function. Corrections due to Pauli blocking have a large impact on the lowest Q^2 setting and less of an impact on the higher Q^2 settings (Figure 4-4). While we attempted to correct for these effects in the πCT analysis, a better theoretical understanding of the nuclear transparency based on traditional nuclear physics is desirable. The model uncertainty in the nuclear transparency was estimated by summing in quadrature the uncertainty in the Pauli blocking correction (Section 4.4) and the relative changes in the nuclear transparency when correlations were included in the spectral function (Table 5.4). The model uncertainty was 10.6%, 8.7%, 7.5%, 5.7% and 4.3% at Q^2=1.1, 2.15, 3.0, 3.9, and 4.7 (GeV/c)^2, respectively.

5.3 Results from additional kinematic settings

Longitudinal-Transverse (L-T) separations were performed at Q^2 =2.15 and 4.0 (GeV/c)^2. The measured longitudinal and transverse virtual photon cross sections ($d^2\sigma_L/d\Omega_\pi$ and $d^2\sigma_T/d\Omega_\pi$) of a free proton may be different when compared to that of a proton inside of a nucleus due to effects such as nucleon correlations in the spectral function, medium modification of the nucleons and absorption of the outgoing pion. However, in the quasifree picture, the ratio σ_L/σ_T is not expected to change, but in reality this may not be the case. Preliminary results for this analysis from Ref. [84] do not show any inconsistency in this ratio between hydrogen and nuclear targets and are shown in Figure 5-7.

The nuclear transparency for the W vs. k_π kinematic setting is shown in Figure 5-8. This setting was designed to check for rescattering contributions in the experimental yields in nuclear targets. The central settings of the spectrometers corresponded to $-t$=0.374 (GeV/c)^2 for the W vs. k_π kinematic setting and 0.158 (GeV/c)^2 for the previous setting at the same Q^2. Rescattering contributions, if they exist, will result in a t dependence of the nuclear transparency. The results in Figure 5-8 show that there is no t dependence of the nuclear transparency within the statistical and systematic uncertainties.

A check of the analysis method was performed by determining the nuclear transparency for the low-epsilon settings that were used in the L-T separations. The central kinematics

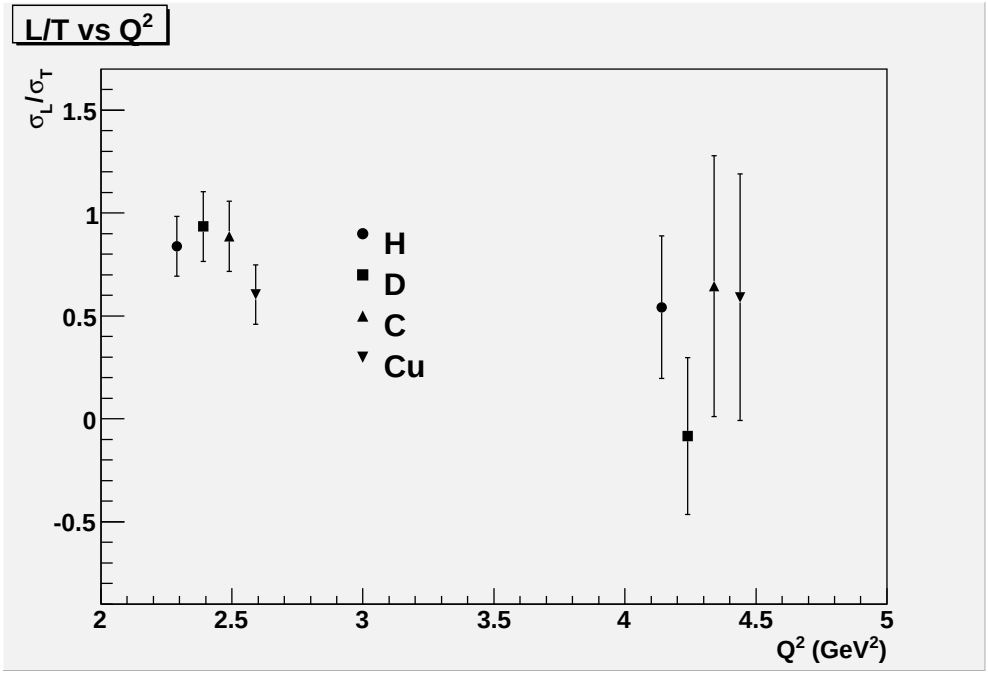

Figure 5-7: Preliminary results for the Longitudinal-Transverse (L-T) separations of the pion electroproduction cross section from hydrogen and nuclear targets. Results from different targets have been offset slightly in Q^2 for clarity. The error bars are the statistical uncertainties.

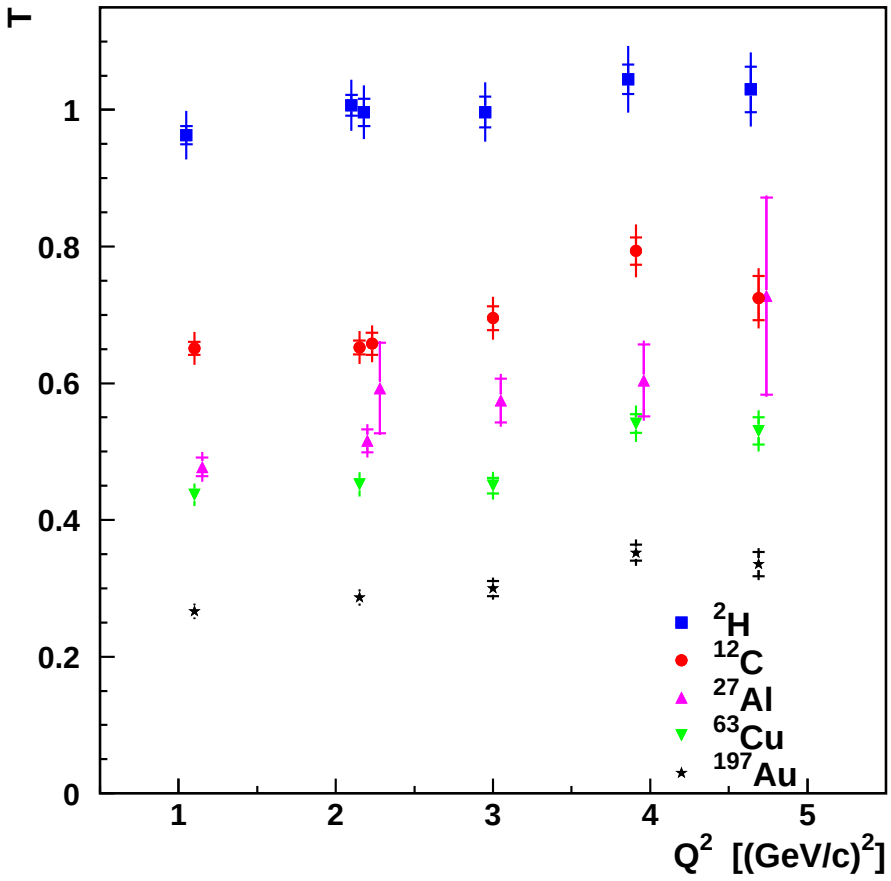

Figure 5-8: Results showing the nuclear transparency for the W vs. k_π kinematic setting. These data for ^{2}H, ^{12}C and ^{27}Al are shown at Q^2=2.15 (GeV/c)^2 and are offset slightly to larger Q^2 compared to the previous data.

of the low-epsilon settings had similar Q^2 and P_π compared to the high-epsilon settings, and therefore, the nuclear transparency was expected to be the same. These data are shown in Figure 5-9, and the agreement is reasonable for different settings.

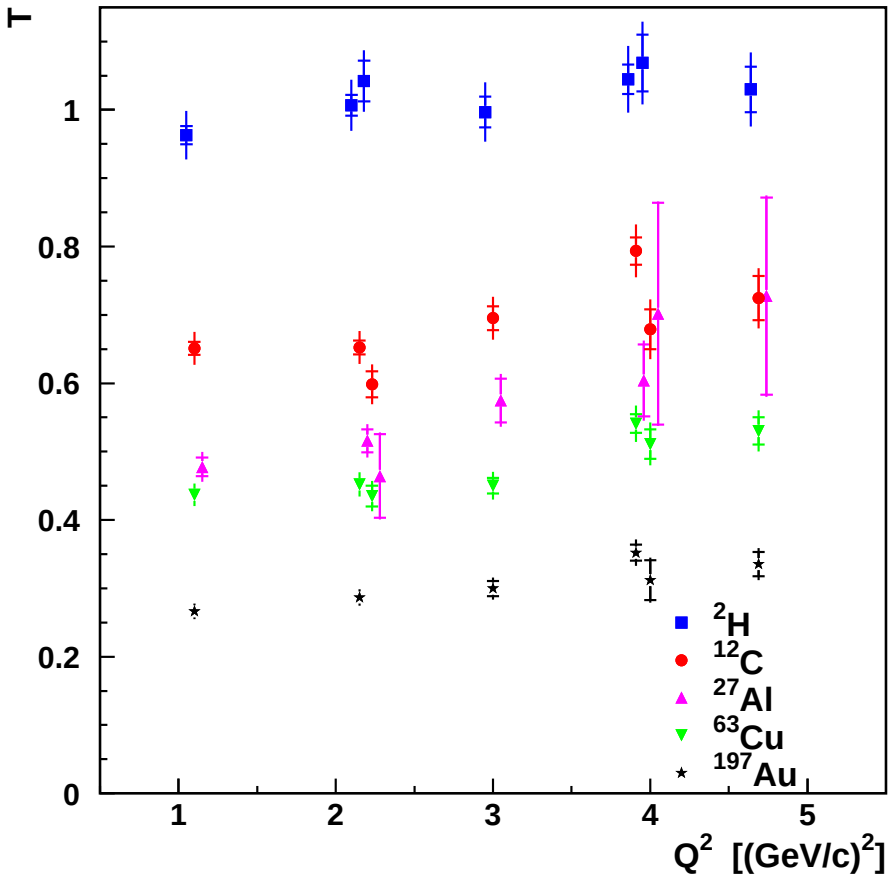

Figure 5-9: Results showing the nuclear transparency for the low epsilon kinematic settings. These data for ^{2}H, ^{12}C, ^{27}Al and ^{63}Cu are shown at Q^2=2.15 and 4.0 (GeV/c)^2, and are offset slightly to larger Q^2 compared to the previous data.

5.4 Results using different analysis options

There were a number of different options in the analysis procedure, such as the model for the energy of the proton, nucleon correlations in the spectral function, double-pion production missing mass cuts, and Coulomb corrections for the pion. For the results in the preceding sections, we selected the options that gave us the best agreement between the experimental and Monte Carlo missing mass and other distributions. The results with changes in the analysis options will be shown in this section.

The different models for the energy of the proton (Section 1.9) affected the Monte Carlo missing mass distributions. This can be seen in Figures 5-10 and 5-11 for the deuterium

Q^2 (GeV/c)^2	ΔT
1.10	0.047
2.15	0.058
3.00	0.052
3.91	0.040
4.69	0.030

Table 5.4: Results after inserting correlations in the spectral function for carbon. ΔT is the change in the nuclear transparency due to correlations.

and carbon targets, respectively. The Monte Carlo distributions in these figures contain an arbitrary normalization so that one may compare the shapes of the distributions. It can be seen that the Monte Carlo distributions are shifted to larger missing mass for the default model and to smaller missing mass for the proton-on-shell model. The distributions for carbon at Q^2=1.1 (GeV/c)^2 show inconsistencies between the experimental and Monte Carlo distributions which could be due to the limitations of the Pauli blocking model and/or n-N FSI. However, the $E_m = 0$ model appears to provide better agreement for this setting. Furthermore, the aforementioned limitations are expected to become insignificant for the settings with $Q^2 \gtrsim 2.15$ (GeV/c)^2, and the distributions for carbon at Q^2=4 (GeV/c)^2 show that the $E_m = 0$ model provides the best agreement. Therefore, the $E_m = 0$ model was used for all other results presented in this chapter.

The spectral functions used in this analysis did not contain nucleon correlations as we did not have access to this type of spectral function for the targets in πCT other than ^{12}C. The nuclear transparency for the carbon target using the spectral function with nucleon correlations is shown in Figure 5-12. In this case, nucleon correlations produce an energy-independent shift in the nuclear transparency. The values of the size of this shift is given in Table 5.4.

Multi-pion events could be excluded using either nucleon or nuclear missing mass cuts. The results for the nuclear transparency using nucleon missing mass cuts are shown in Figure 5-13. The nuclear transparency is similar to the results using nuclear missing mass cuts presented in Section 5.1, which gives us confidence in the analysis procedure.

Coulomb corrections for the pion were a large (up to 9.5%) effect, and the results presented in section 5.1 have these corrections. The nuclear transparency without Coulomb corrections for the pion are shown in Figure 5-14. These corrections affected the missing

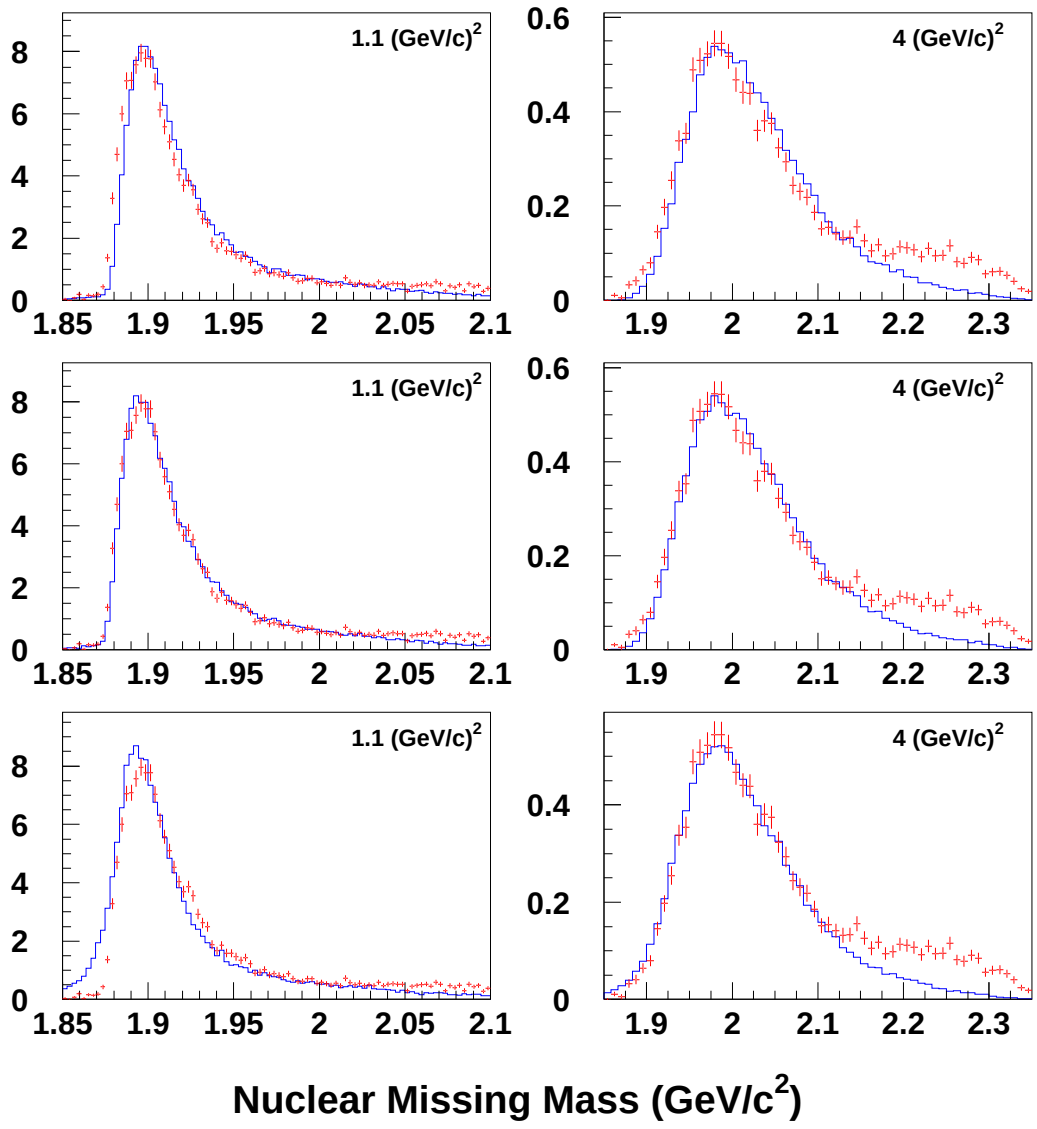

Figure 5-10: Experimental (crosses) and Monte Carlo (lines) nuclear missing mass distributions for ^{2}H(e,e$'\pi^+$). The top, middle and bottom plots use the default, E_m=0 and proton-on-shell models in the Monte Carlo simulation, respectively. The Q^2 settings for each plot are shown in the figure.

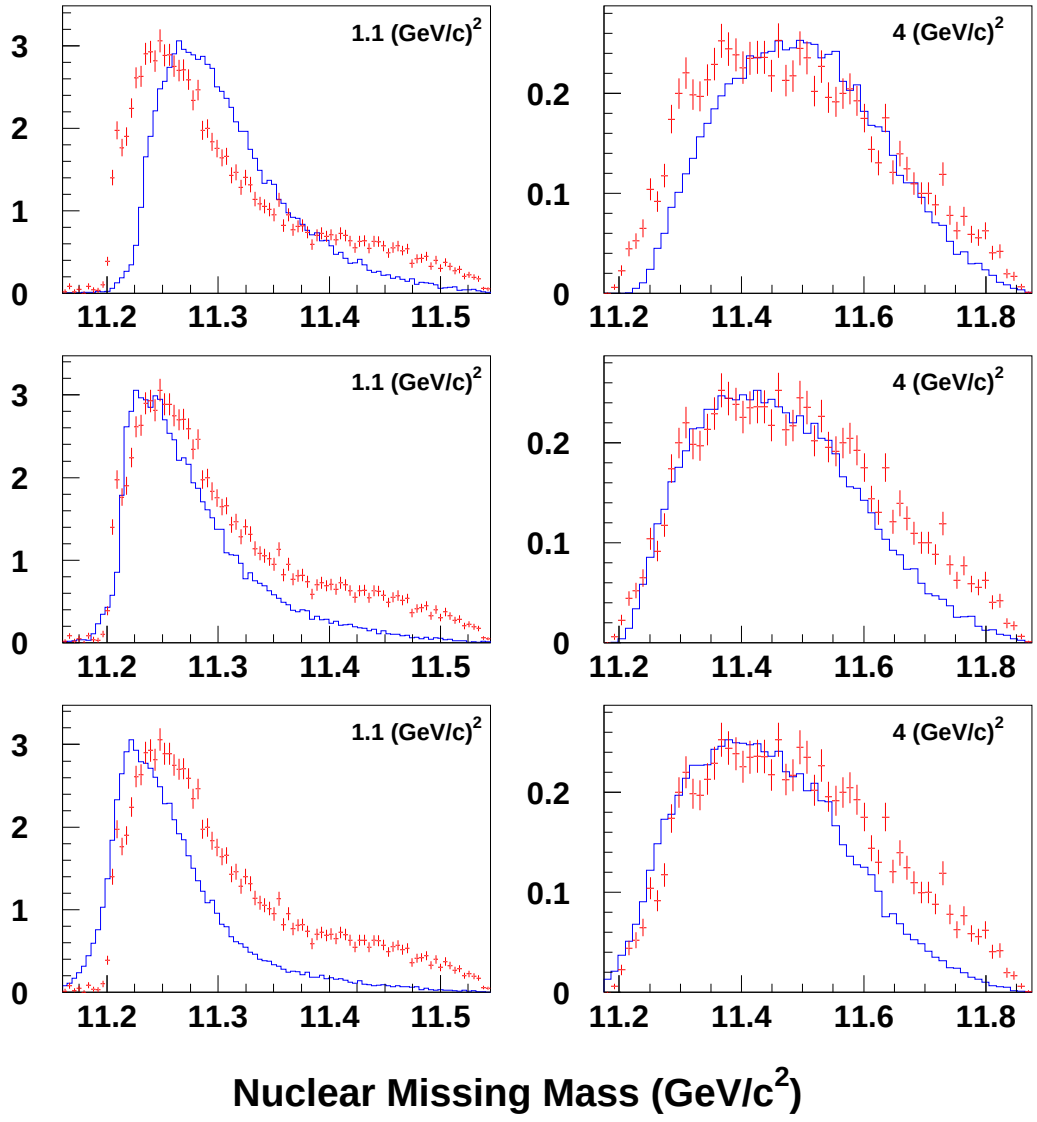

Figure 5-11: Experimental (crosses) and Monte Carlo (lines) nuclear missing mass distributions for ^{12}C(e,e$'\pi^+$). The top, middle and bottom plots use the default, E_m=0 and proton-on-shell models in the Monte Carlo simulation, respectively. The Q^2 settings for each plot are shown in the figure.

mass distributions and there was better agreement between the experimental data and the Monte Carlo when these corrections were used. The changes in the Monte Carlo equivalent yield without Coulomb corrections for the pion were 7-9.5%, 3-5.5% and 1-1.5% for the gold, copper and carbon targets, respectively. Therefore, the Coulomb corrections for the pion are energy independent within 1-2%.

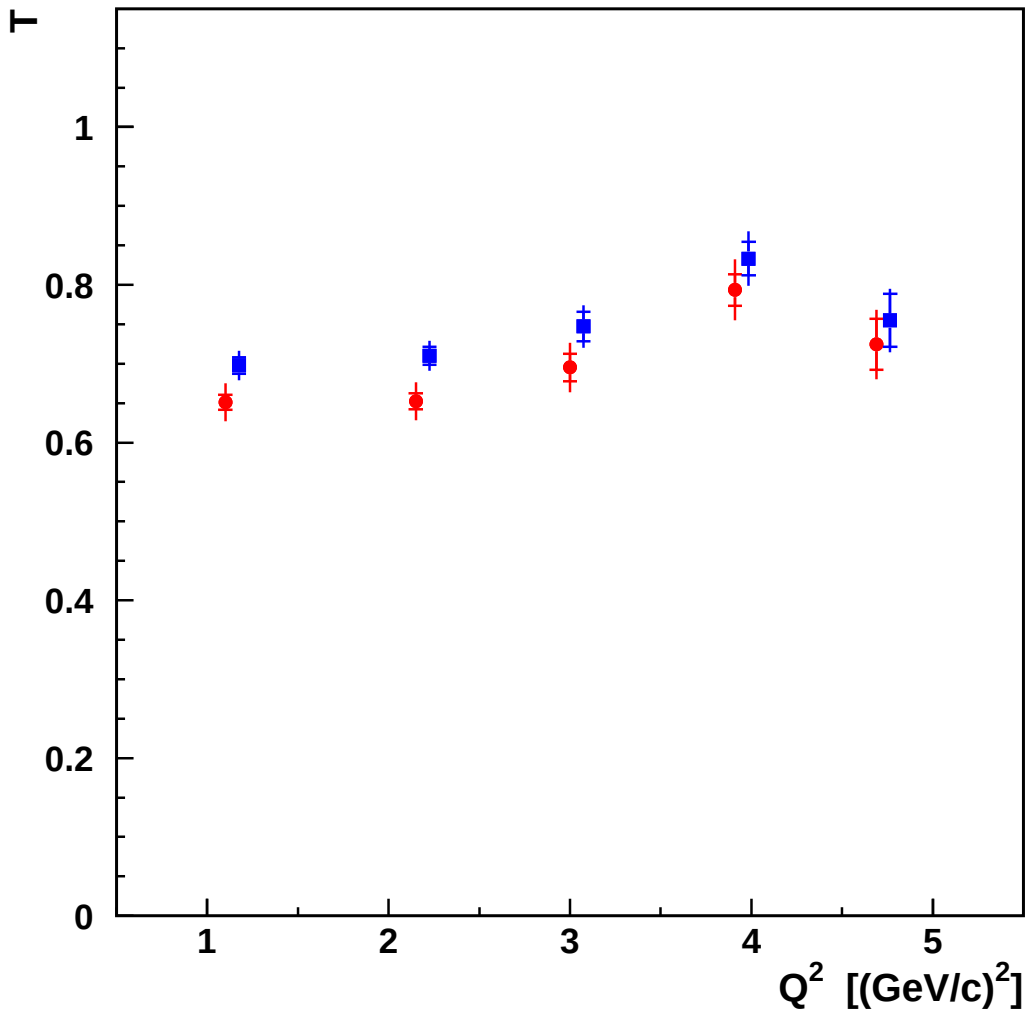

Figure 5-12: The effect of including correlations in the Monte Carlo for carbon nuclei. The nuclear transparency is shown before (red, circles) and after (blue, squares) nucleon correlations were included in the spectral function. The results for the latter case are offset in Q^2 for clarity.

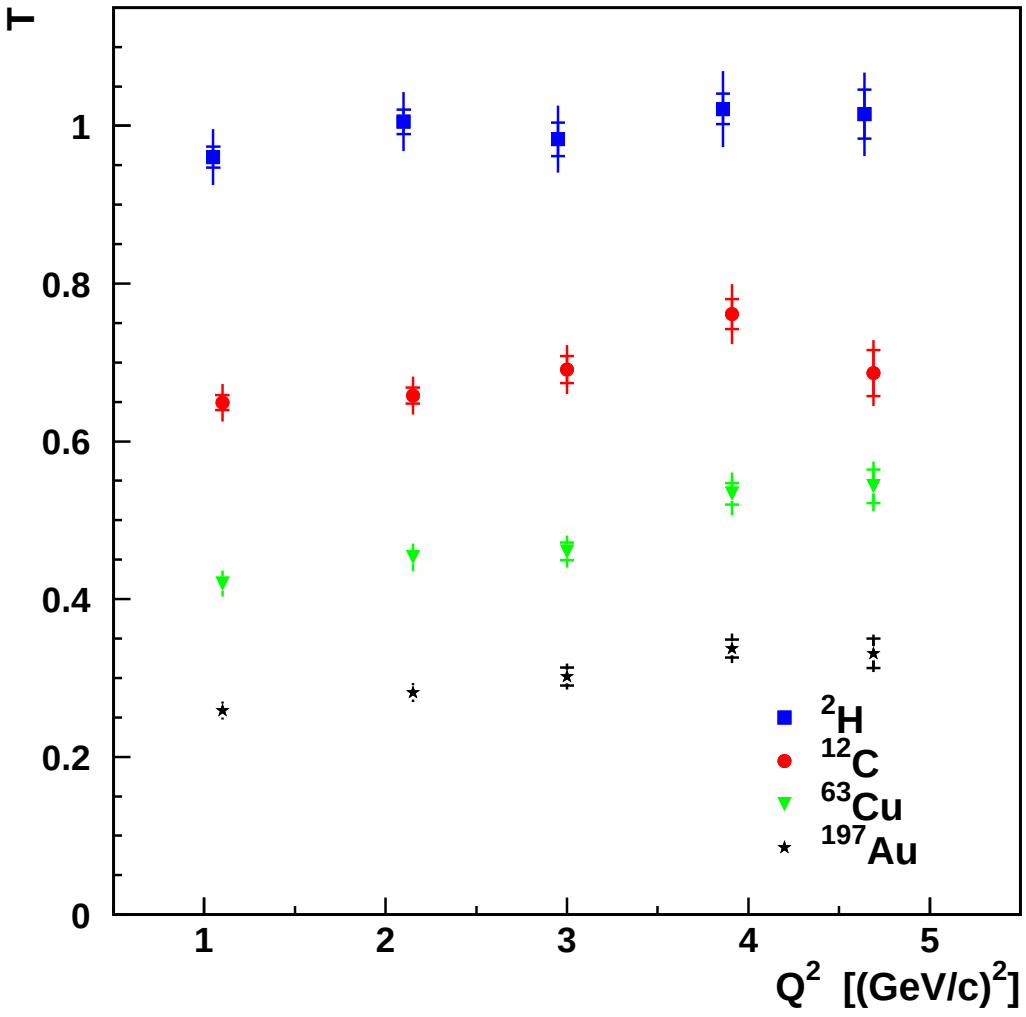

Figure 5-13: Nuclear transparency results using the nucleon missing mass cut.

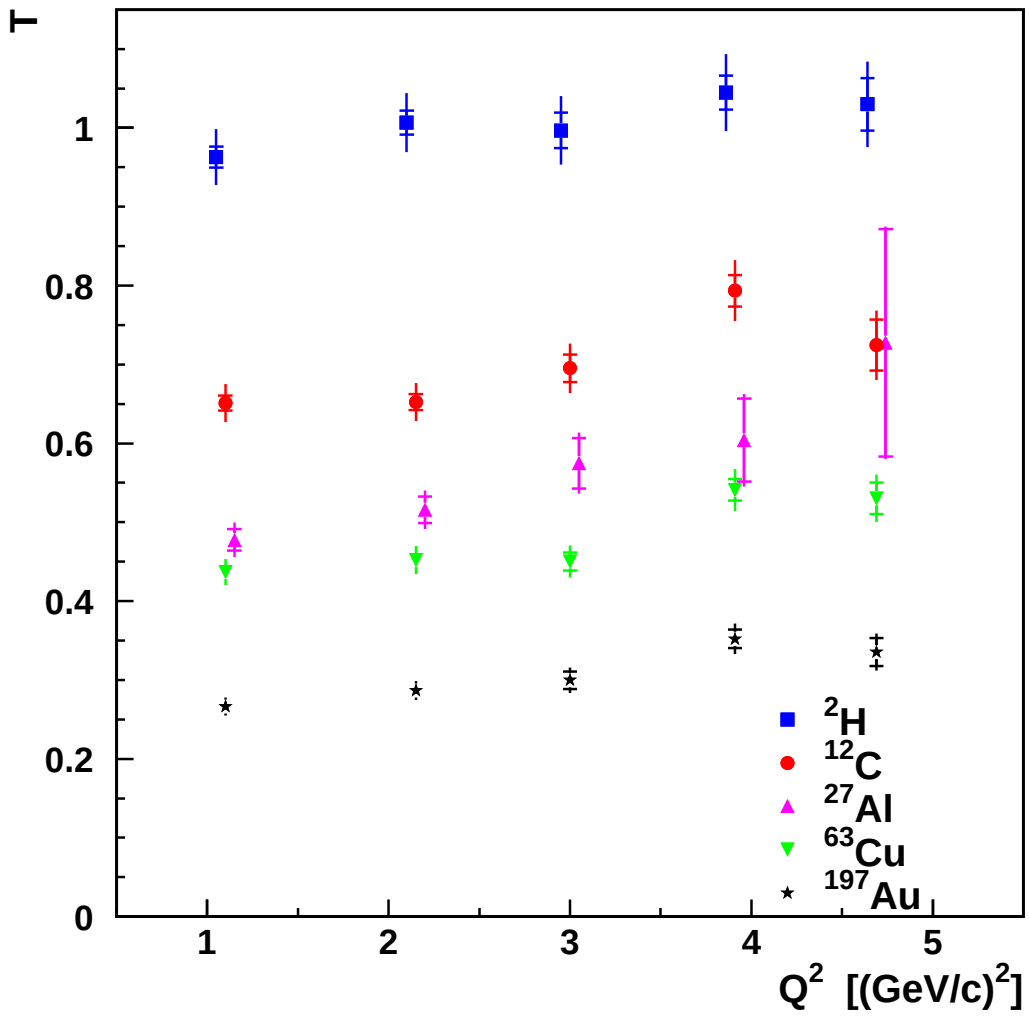

Figure 5-14: Nuclear transparency results without Coulomb corrections for the pion.

Chapter 6

Summary and Outlook

The nuclear transparency of pions in the reaction A(e,e$'\pi^+$) was measured from ^{1}H, ^{2}H,^{12}C, ^{63}Cu and ^{197}Au targets at Q^2 of 1.1, 2.15, 3.0, 3.9 and 4.7 (GeV/c)^2. The results for the nuclear transparency were presented in Figure 5-1 and the parameter α was shown as a function of Q^2 in Figure 5-4. The results suggest an enhancement of the nuclear transparency as a function of Q^2 and P_π that is in reasonable agreement with theoretical predictions of color transparency in Refs. [45, 8]. However, these data do not provide conclusive evidence for the color transparency effect.

It was found that reasonable agreement between the experimental and Monte Carlo distributions was achieved using nuclear missing mass cuts, where the position of the cut was based on a multi-pion production simulation. Shifts observed between the experimental and Monte Carlo missing mass distributions appear to be explained by the E_m=0 model for the energy of the proton. A model of Pauli blocking of the recoiling neutron was employed in this analysis, which had a large impact on the nuclear transparency at low Q^2. However, inconsistencies remain between the experimental and Monte Carlo missing mass distributions at Q^2=1.1 (GeV/c)^2. A better theoretical understanding of the nuclear transparency based on traditional nuclear physics is desirable and will help to distinguish color transparency effects from conventional nuclear physics effects. In particular, a reliable model of the operator for the elementary process would be useful to predict the absolute cross sections in deuterium and estimate the effects of Pauli blocking using nuclear wave functions. Spectral functions that include nucleon correlations would be useful to remove the effect of correlations on the nuclear transparency.

Larger energies will soon be available at JLab and the color transparency effect will be probed at larger Q^2 and P_π compared to πCT, where the enhancement of the nuclear transparency is expected to be larger. The results from this experiment will provide a baseline from which the enhancement at larger energies will be examined. The pion form factor will also be extracted at Q^2=2.15 (GeV/c)^2 using results from the L-T separation in πCT. Furthermore, a large sample of kaon data was taken parasitically during πCT. With the good particle identification described in Chapter 2, it may be possible to determine the nuclear transparency from A(e,e$'K^+$) reactions. The data from πCT may also be used to measure the cross section for multi-pion production.

Appendix A

Experimental and Monte Carlo distributions

The distributions from the experiment and Monte Carlo are compared in this Appendix. The error bars in the following figures indicate the statistical uncertainties. The ends of the Monte Carlo error bars are joined forming a double line in each figure. The Monte Carlo distributions are normalized to have the same area as the experimental distributions.

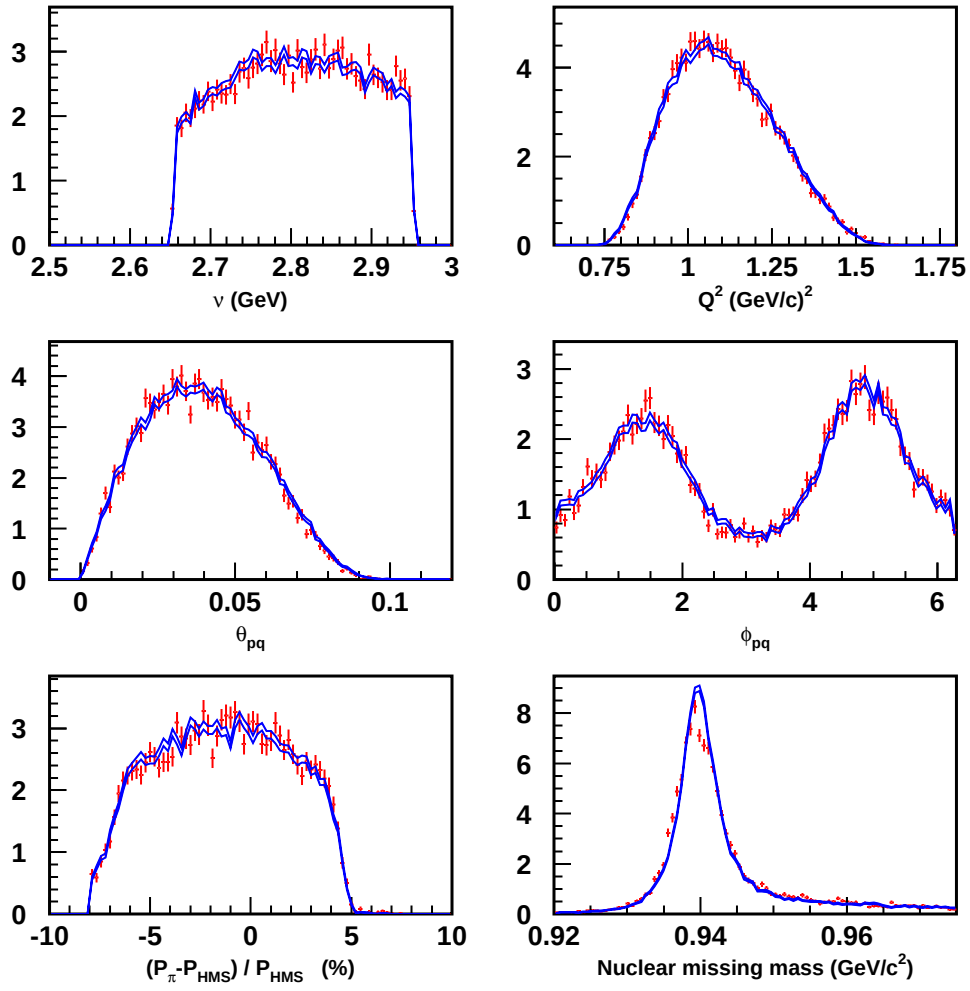

Figure A-1: Experimental (crosses) and Monte Carlo (lines) distributions for the hydrogen target at Q^2=1.1 (GeV/c)^2. The vertical line shows the position of the double-pion production missing mass cut.

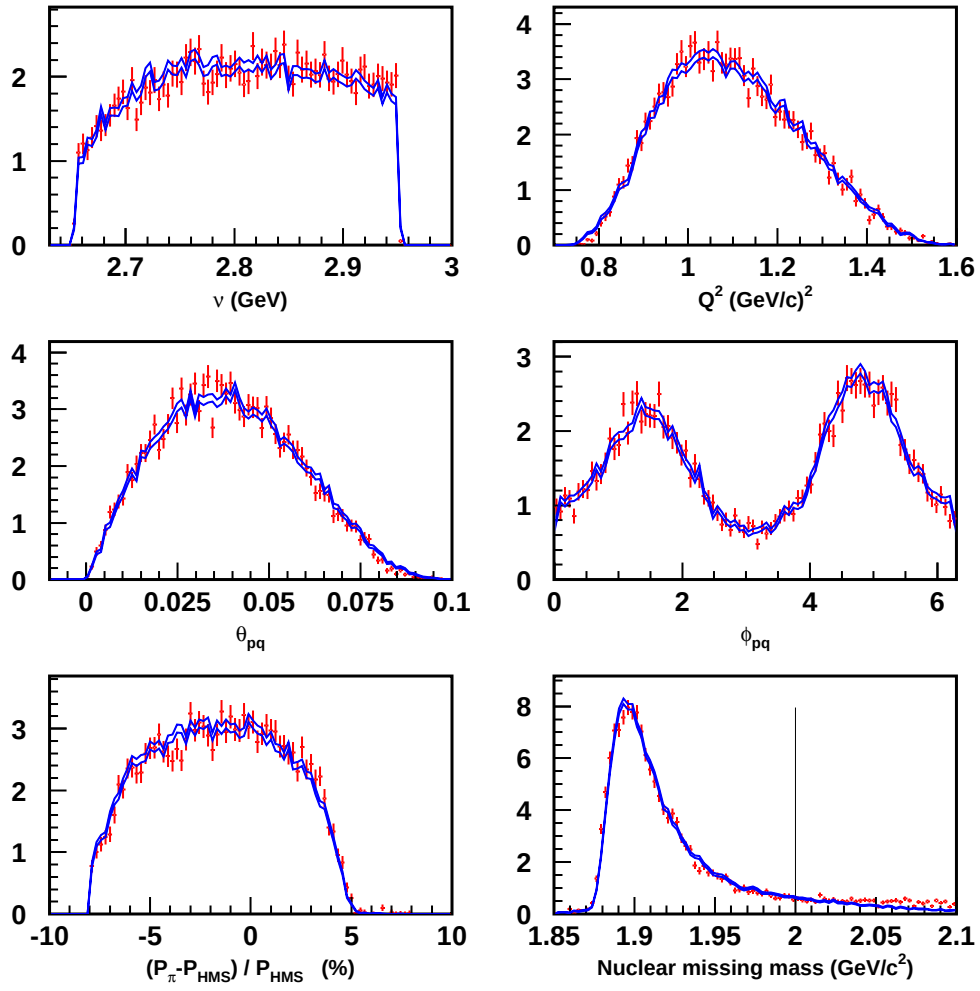

Figure A-2: Experimental (crosses) and Monte Carlo (lines) distributions for the deuterium target at Q^2=1.1 (GeV/c)^2. The vertical line shows the position of the double-pion production missing mass cut.

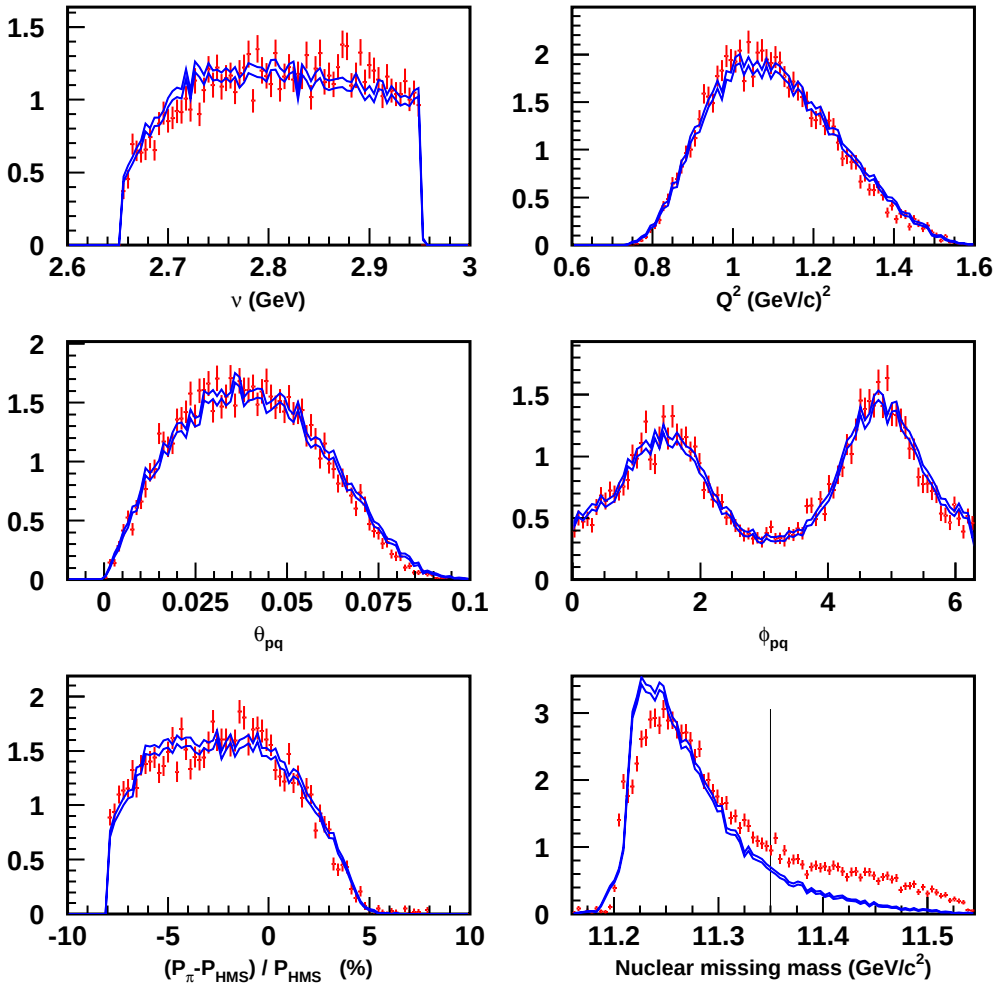

Figure A-3: Experimental (crosses) and Monte Carlo (lines) distributions for the carbon target at Q^2=1.1 (GeV/c)^2. The vertical line shows the position of the double-pion production missing mass cut.

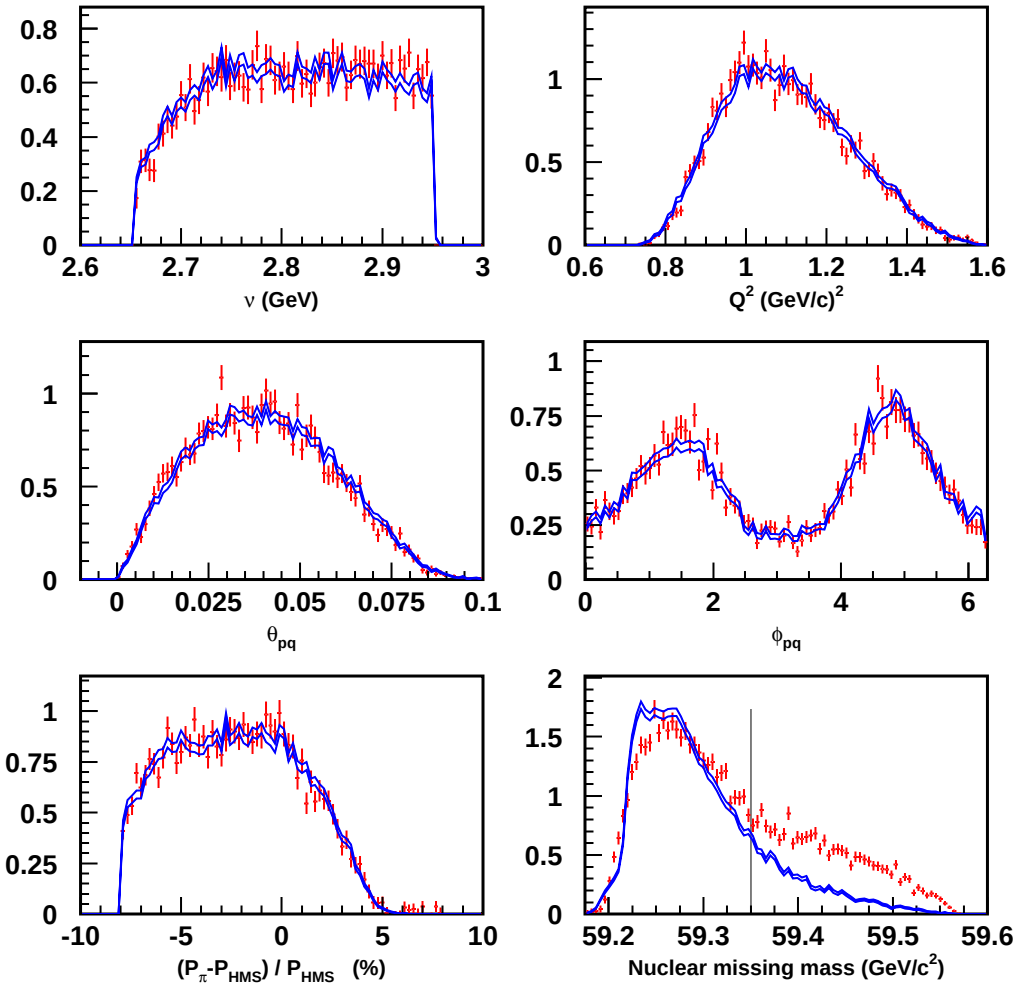

Figure A-4: Experimental (crosses) and Monte Carlo (lines) distributions for the copper target at Q^2=1.1 (GeV/c)^2. The vertical line shows the position of the double-pion production missing mass cut.

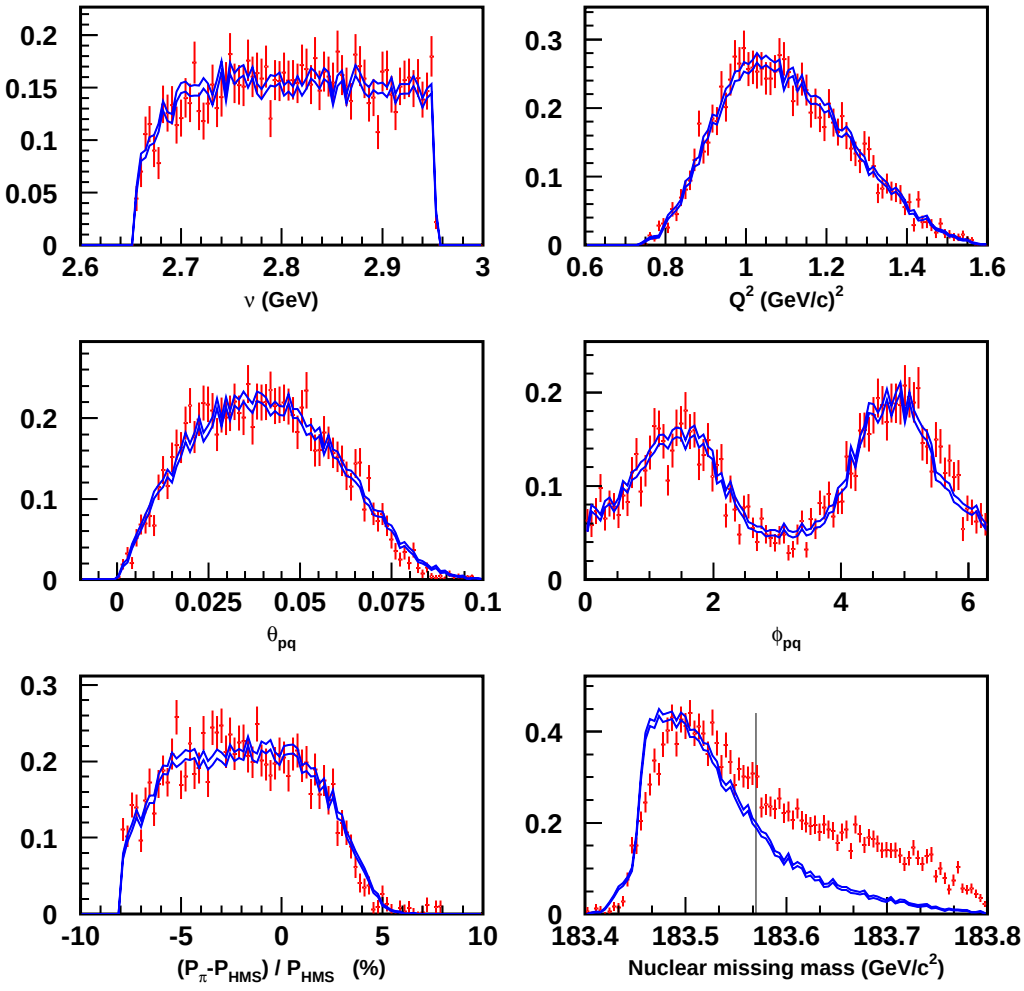

Figure A-5: Experimental (crosses) and Monte Carlo (lines) distributions for the gold target at Q^2=1.1 (GeV/c)^2. The vertical line shows the position of the double-pion production missing mass cut.

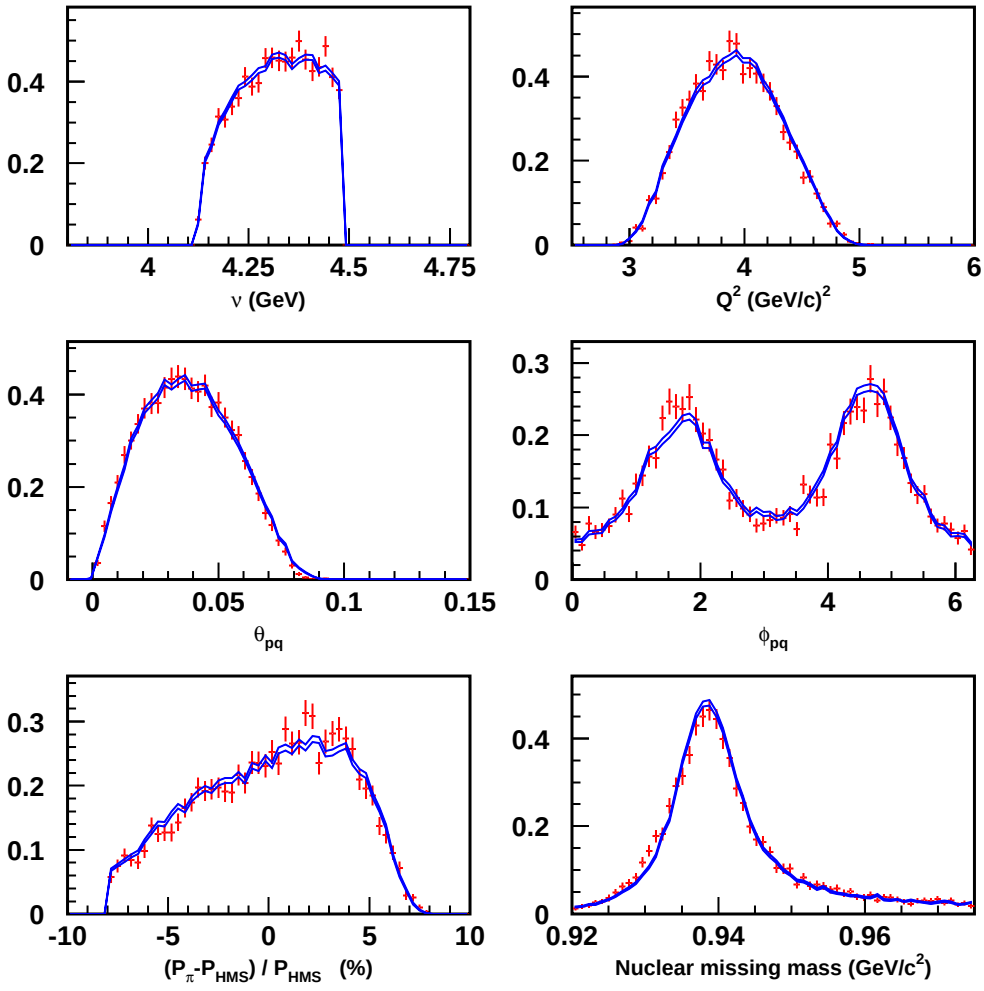

Figure A-6: Experimental (crosses) and Monte Carlo (lines) distributions for the hydrogen target at Q^2=3.9 (GeV/c)^2. The vertical line shows the position of the double-pion production missing mass cut.

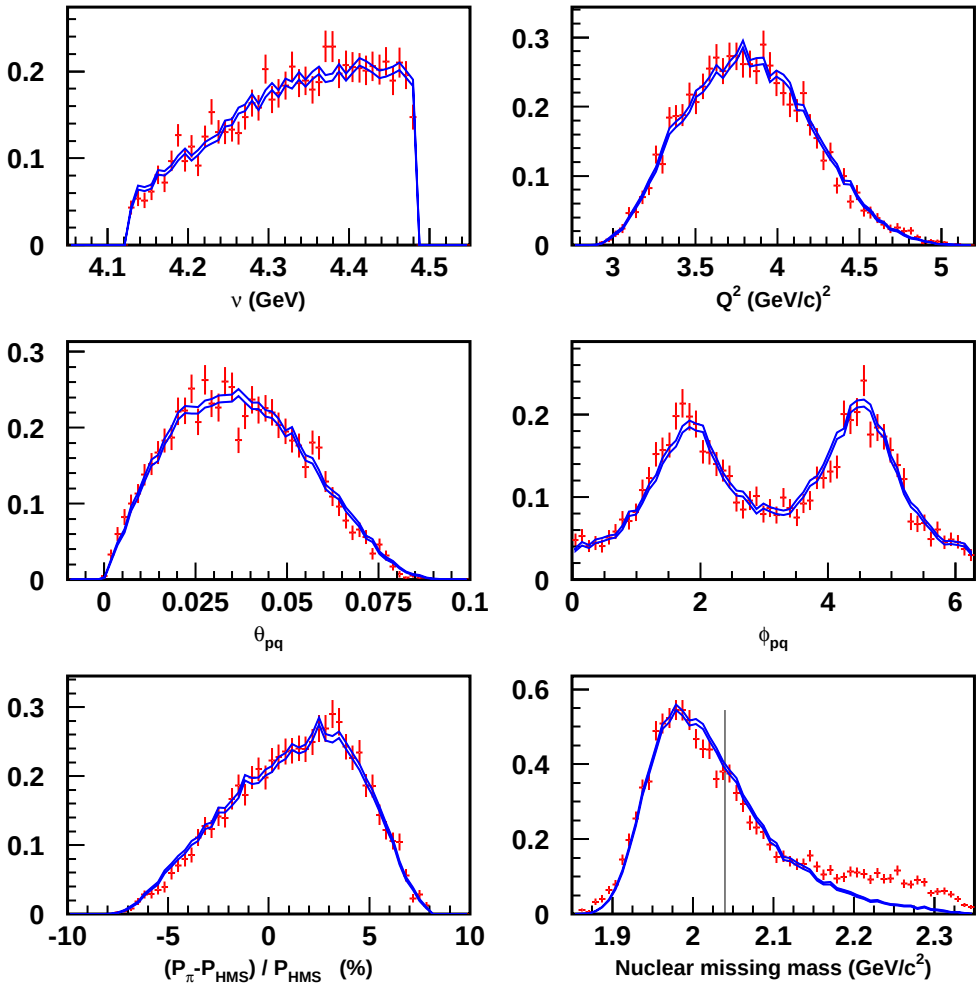

Figure A-7: Experimental (crosses) and Monte Carlo (lines) distributions for the deuterium target at Q^2=3.9 (GeV/c)^2. The vertical line shows the position of the double-pion production missing mass cut.

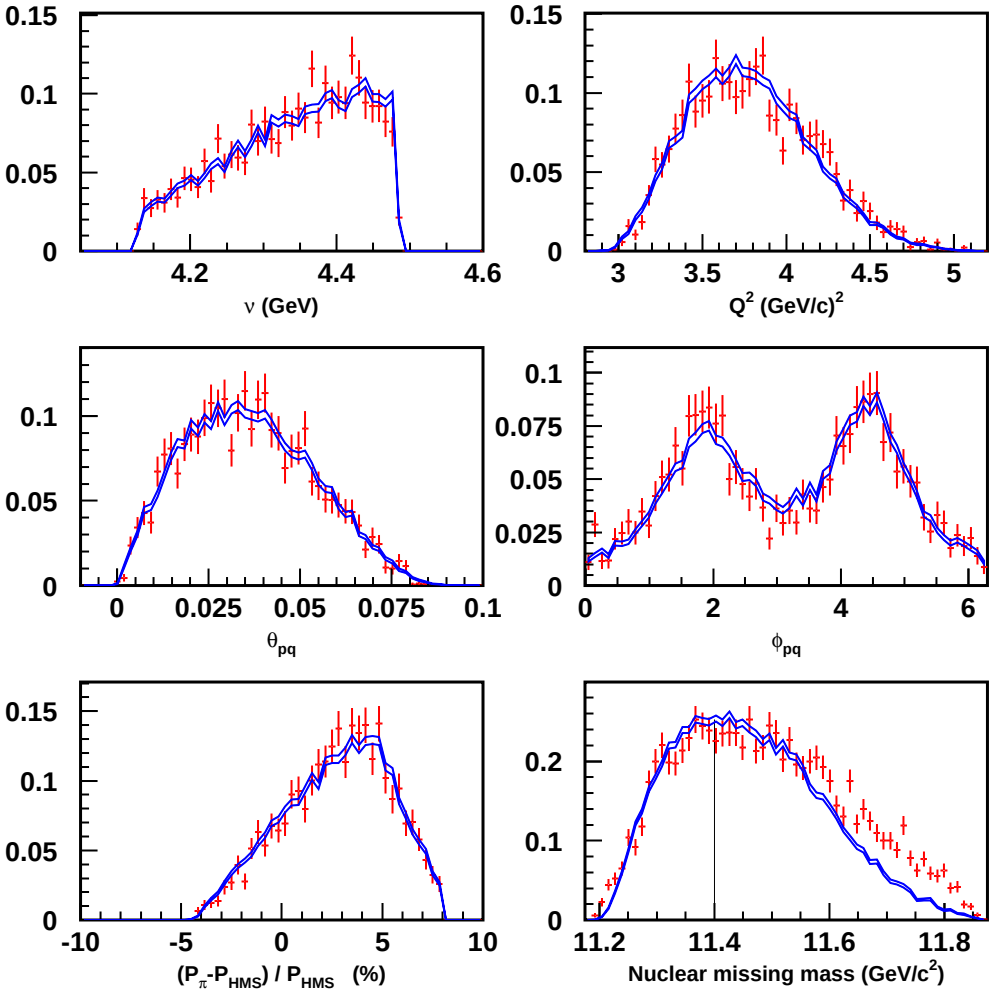

Figure A-8: Experimental (crosses) and Monte Carlo (lines) distributions for the carbon target at Q^2=3.9 (GeV/c)^2. The vertical line shows the position of the double-pion production missing mass cut.

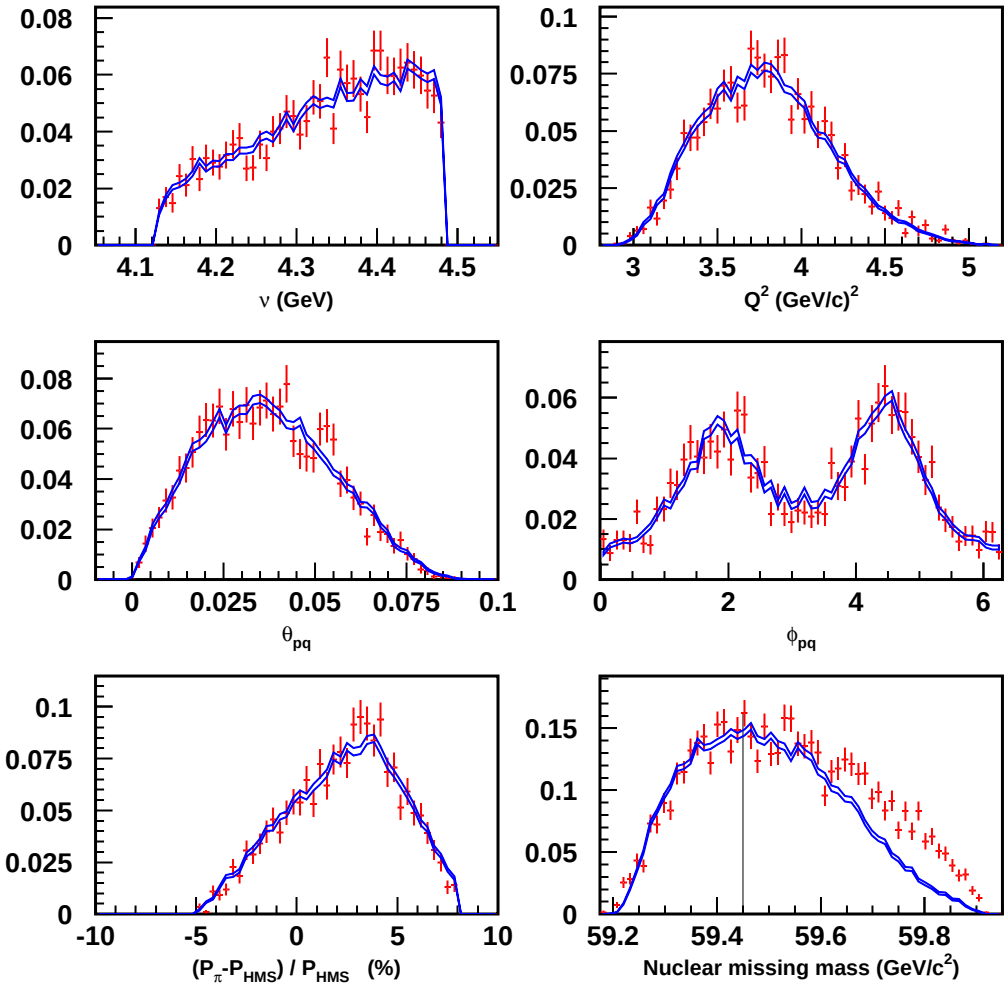

Figure A-9: Experimental (crosses) and Monte Carlo (lines) distributions for the copper target at Q^2=3.9 (GeV/c)^2. The vertical line shows the position of the double-pion production missing mass cut.

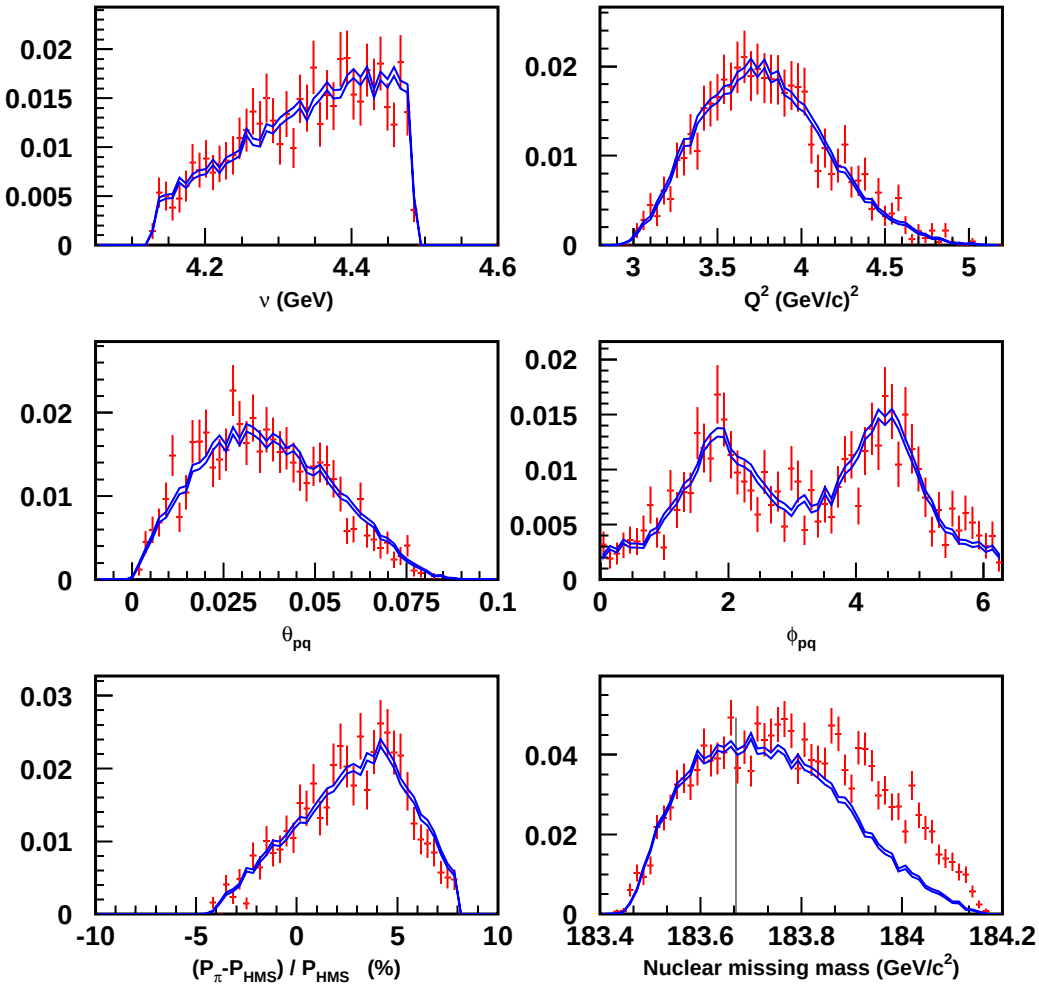

Figure A-10: Experimental (crosses) and Monte Carlo (lines) distributions for the gold target at Q^2=3.9 (GeV/c)^2. The vertical line shows the position of the double-pion production missing mass cut.

Bibliography

[1] A. Mueller, in *Proceedings of the Seventeenth Recontre de Moriond, Moriond* (Editions Frontieres, Gif-sur-Yvette, France, 1982), p. 13.

[2] S. J. Brodsky, G. T. Bodwin, and G. P. Lepage, in *Proceedings of the 13th Int. Symp. on Multiparticle Dynamics, Volendam, 1982* (World Scientific, Singapore, 1982), p. 963.

[3] S. J. Brodsky and A. H. Mueller, Phys. Lett. **B206**, 685 (1988).

[4] B. Povh and J. Hufner, Phys. Rev. Lett. **58**, 1612 (1987).

[5] D. Dutta, Eur. Phys. J. **A19S1**, 179 (2004).

[6] R. J. Glauber, in: Lectures in theoretical physics, ed. W. E. Brittin et al. (Interscience Publishers, New York, 1959), vol. I, p 315.

[7] G. R. Farrar, H. Liu, L. L. Frankfurt, and M. I. Strikman, Phys. Rev. Lett. **61**, 686 (1988).

[8] A. Larson, G. A. Miller, and M. Strikman, nucl-th/0604022 (2006).

[9] M. Strikman, Nucl. Phys. **A663**, 64 (2000).

[10] A. S. Carroll *et al.*, Phys. Rev. Lett. **61**, 1698 (1988).

[11] I. Mardor *et al.*, Phys. Rev. Lett. **81**, 5085 (1998).

[12] A. Leksanov *et al.*, Phys. Rev. Lett. **87**, 212301 (2001).

[13] J. P. Ralston and B. Pire, Phys. Rev. Lett. **65**, 2343 (1990).

[14] J. P. Ralston and B. Pire, Phys. Rev. Lett. **61**, 1823 (1988).

[15] S. J. Brodsky and G. F. de Teramond, Phys. Rev. Lett. **60**, 1924 (1988).

[16] K. Garrow *et al.*, Phys. Rev. **C66**, 044613 (2002).

[17] G. Garino *et al.*, Phys. Rev. **C45**, 780 (1992).

[18] N. Makins *et al.*, Phys. Rev. Lett. **72**, 1986 (1994).

[19] T. O'Neill *et al.*, Phys. Lett. **B351**, 87 (1995).

[20] D. Abbott *et al.*, Phys. Rev. Lett. **80**, 5072 (1998).

[21] J. M. Laget, Phys. Rev. **C73**, 044003 (2006).

[22] M. R. Adams *et al.* (E665), Phys. Rev. Lett. **74**, 1525 (1995).

[23] A. Airapetian *et al.* (HERMES), Phys. Rev. Lett. **90**, 052501 (2003).

[24] K. Ackerstaff *et al.* (HERMES), Phys. Rev. Lett. **82**, 3025 (1999).

[25] J. M. Laget, nucl-th/0507035 (2005).

[26] E. M. Aitala *et al.* (E791), Phys. Rev. Lett. **86**, 4773 (2001).

[27] D. Dutta *et al.* (Jefferson Lab E94-104), Phys. Rev. **C68**, 021001(R) (2003).

[28] L. Y. Zhu *et al.* (Jefferson Lab Hall A), Phys. Rev. **C71**, 044603 (2005).

[29] L. Y. Zhu *et al.* (Jefferson Lab Hall A), Phys. Rev. Lett. **91**, 022003 (2003).

[30] J. M. Laget, Phys. Rev. **D70**, 054023 (2004).

[31] D. Gaskell, *Longitudinal electroproduction of charged pions from hydrogen, deuterium and helium-3*, Ph.D. thesis, Oregon State University (2001), http://www1.jlab.org/Ul/publications/documents/gaskell.pdf.

[32] S. Nozawa and T. S. H. Lee, Nucl. Phys. **A513**, 511 (1990).

[33] J. Volmer, *The pion charge form factor via pion electroproduction on the proton*, Ph.D. thesis, Vrije Universiteit (2000).

[34] E. Quint, *The Proton Spectral Function of* 27Al, Tech. rep., NIKHEF internal note (1983).

[35] K. Holinde and R. Machleidt, Nucl. Phys. **A256**, 479 (1976).

[36] R. B. Wiringa, V. G. J. Stoks, and R. Schiavilla, Phys. Rev. **C51**, 38 (1995).

[37] C. Giusti and F. D. Pacati, Nucl. Phys. **A485**, 461 (1988).

[38] C. Giusti and F. D. Pacati, Nucl. Phys. **A473**, 717 (1987).

[39] J. Mougey *et al.*, Nucl. Phys. **A262**, 461 (1976).

[40] N. Makins, *Measurement of the nuclear dependence and momentum transfer dependence of quasielastic (e,e′p) scattering at large momentum transfer*, Ph.D. thesis, Massachusetts Institute of Technology (1994).

[41] G. E. Brown and M. Rho, Nucl. Phys. **A372**, 397 (1981).

[42] S. Eidelman *et al.* (Particle Data Group), Phys. Lett. **B592**, 1 (2004).

[43] V. R. Pandharipande and C. Pieper, Steven, Phys. Rev. **C45**, 791 (1992).

[44] B. Z. Kopeliovich, J. Nemchick, N. N. Nikolaev, and B. G. Zakharov, Phys. Lett. **B324**, 469 (1994).

[45] B. Kundu, J. Samuelsson, P. Jain, and J. P. Ralston, Phys. Rev. **D62**, 113009 (2000).

[46] V. L. Chernyak and A. R. Zhitnitsky, Phys. Rept. **112**, 173 (1984).

[47] V. L. Chernyak and I. R. Zhitnitsky, Nucl. Phys. **B246**, 52 (1984).

[48] S. J. Brodsky and G. P. Lepage, Phys. Rev. **D24**, 2848 (1981).

[49] D. Drechsel, S. S. Kamalov, and L. Tiator, Nucl. Phys. **A645**, 145 (1999).

[50] G. Bertsch, S. J. Brodsky, A. S. Goldhaber, and J. F. Gunion, Phys. Rev. Lett. **47**, 297 (1981).

[51] A. S. Carroll *et al.*, Phys. Lett. **B80**, 319 (1979).

[52] R. L. Anderson *et al.*, Phys. Rev. **D4**, 3245 (1971).

[53] M. M. Sargsian *et al.*, J. Phys. **G29**, R1 (2003), nucl-th/0210025.

[54] B. L. Friman, V. R. Pandharipande, and R. B. Wiringa, Phys. Rev. Lett. **51**, 763 (1983).

[55] D. Gaskell *et al.*, Phys. Rev. Lett. **87**, 202301 (2001).

[56] J. Gomez *et al.*, Phys. Rev. **D49**, 4348 (1994).

[57] T. De Forest, Nucl. Phys. **A392**, 232 (1983).

[58] B. Frois and C. N. Papanicolas, Ann. Rev. Nucl. Part. Sci. **37**, 133 (1987).

[59] L. Lapikas, Nucl. Phys. **A553**, 297c (1993).

[60] L. Lapikas, G. van der Steenhoven, L. Frankfurt, M. Strikman, and M. Zhalov, Phys. Rev. **C61**, 064325 (2000).

[61] L. Frankfurt, M. Strikman, and M. Zhalov, Phys. Lett. **B503**, 73 (2001).

[62] J. Arrington, *Inclusive electron scattering from nuclei at $x > 1$ and high Q^2*, Ph.D. thesis, California Institute of Technology (1998).

[63] D. Dutta, *The (e,e′p) reaction mechanism in the quasi-elastic region*, Ph.D. thesis, Northwestern University (1999).

[64] R. Mohring, *A comparison of longitudinal and transverse cross sections in the $p(e, e'K^+)\Lambda$ and $p(e, e'K^+)\Sigma^0$ reactions*, Ph.D. thesis, University of Maryland (1999).

[65] T. Horn, *The pion charge form factor through pion electroproduction*, Ph.D. thesis, University of Maryland (2006).

[66] X. Chuncheng, *Optics Check for different Psos*, Tech. rep., http://www.jlab.org/ xu/OPTCHECK.html.

[67] G. F. Knoll, *Radiation Detection and Measurement* (John Wiley and Sons, Inc., New York, 1999), 3rd ed.

[68] P. Bosted and M. Jones, *Hodoscope timing code enhancement*, Tech. rep., Hallc C software documentation (March 2005), http://hallcweb.jlab.org/analysis_documentation/hallc_analysis/tof.ps.

[69] P. Bosted and T. Navasardyan, *Track pruning enhancement*, Tech. rep., Hallc C software documentation (March 2005), http://hallcweb.jlab.org/analysis_documentation/hallc_analysis/prune.ps.

[70] D. van Westrum, *Quasielastic (e,e′p) Reactions and Proton Propagation Through Nuclei*, Ph.D. thesis, University of Colorado (1998), http://www1.jlab.org/Ul/publications/documents/vanwestrum_Aeep_thesis.ps.gz.ps.

[71] J. Seely, *EMC effect*, Ph.D. thesis, Massachusetts Institute of Technology (2006).

[72] *COSY INFINITY*, Proceedings of the 1991 Particle Accelerator Conference, see also http://bt.nscl.msu.edu/cosy/index.html.

[73] A. Aste, C. von Arx, and D. Trautmann, Eur. Phys. J. **A26**, 167 (2005).

[74] A. Aste, (private communication).

[75] J. Gillespie, *Final-State Interactions* (Holden-Day, San Francisco, 1964).

[76] C. Maieron, T. W. Donnelly, and I. Sick, Phys. Rev. **C65**, 025502 (2002).

[77] R. R. Whitney, I. Sick, J. R. Ficenec, R. D. Kephart, and W. P. Trower, Phys. Rev. **C9**, 2230 (1974).

[78] S. Fantoni and V. R. Pandharipande, Nucl. Phys. **A427**, 473 (1984).

[79] L. W. Mo and Y.-S. Tsai, Rev. Mod. Phys. **41**, 205 (1969).

[80] J. Arrington, Phys. Rev. **C69**, 022201 (2004).

[81] M. E. Christy *et al.* (E94110), Phys. Rev. **C70**, 015206 (2004).

[82] L. Andivahis *et al.*, Phys. Rev. **D50**, 5491 (1994).

[83] A. Larson, (private communication).

[84] X. Qian, (private communication).